Ocean/atmosphere interactions and trace metal geochemistry in ocean and sea ice sediments

by

Meghan Anne Taylor

A dissertation submitted in partial fulfillment
of the requirements for the degree of
Doctor of Philosophy
(Earth and Environmental Sciences)
in the University of Michigan
2015

Doctoral Committee:

Associate Professor Ingrid Hendy, Chair
Assistant Professor Sarah Aciego
Assistant Professor Rose Cory
Assistant Professor Mark Flanner
Associate Professor Nathan Sheldon

Acknowledgements

I would like to first thank my advisor, Ingrid Hendy, for taking on a rather challenging student with experience in neither oceanography nor geology. It has been a crash course and I've really enjoyed it. I'd like to thank my committee for their patience with me as a slow learner and for all of the opportunities that they have given me. In particular I'd like to thank Sarah Aciego and Mark Flanner for letting me take on a huge part of the M cubed project, which was a departure from my previous work and a valuable chance to develop a new set of skills in the field and in the lab. In that vein I'd like to thank the whole of the GIGL lab for their generosity in training me to prep for fieldwork and to process samples – I would have been lost without their help.

I'd also like to thank the kind people at the Naval Research Lab and CRREL, especially Jackie Ritcher-Menge, for basically letting me tag along with them in the field, making me feel welcome, and for not leaving me out there on the sea ice. Paolo Gabrielli and his lab were invaluable in helping me analyze all of my sea ice samples and they spent weeks with me ensuring that we got good data. I'd also like to thank Dotti Pak at UCSB for training me in Mg/Ca sample preparation and for being a coauthor and resource for all questions Mg/Ca-related, and Ted Huston who helped me get all of my foraminifera samples run at UM.

I'd like to thank all of my friends among the UM undergraduate, graduate students, and post docs for making these years so much fun. My lab mates are incredibility supportive of one another and several of them have read most of my grants and manuscript drafts over the years.

I'd especially like to thank Tim, Allie, and Tiffany for their encouragement, insightful criticism, and science talks over beers (or in T$'s case, wine).

I owe thanks to my family – to my dad who instilled in me a love of adventure and the outdoors ever since that first road trip to the U.P. and who really instigated it all by getting a subscription to Scientific American and taking me to Utah. And to my mom, the editor, who helped me so much with my first manuscript even though she almost killed me when, during my second round of revisions, she asked me if I wouldn't be better off just starting over with an outline.

And finally I'd like to thank Tom, my partner in all things, who reminds me every day that science is the most fun and that we're incredibly lucky.

Table of Contents

List of Tables

List of Figures

List of Appendices

Abstract

During last glacial period, abrupt climate events were recorded in the Greenland ice core and North Atlantic sediment cores suggest major millennial scale variability in the northern North Atlantic, marked by a series of abrupt climate changes from 60 to 20 ka, first characterized by rapid shifts in the Greenland ice core oxygen isotope record. The use of high-resolution marine sediment cores in regions like the Pacific Ocean that are far afield from the region of climatic forcing allows us to evaluate different mechanisms for transmission of these major climate change events. The subarctic northeastern Pacific Ocean was also influenced by the growth and retreat of the smaller, western side of the North American ice sheet, the Cordilleran Ice Sheet (CIS).

In Chapters 2 and 3, I use the $\delta^{18}O_{calcite}$ and the ratio of Mg/Ca in planktonic foraminifera to reconstruct sea surface temperatures and $\delta^{18}O_{seawater}$ from high-resolution ocean sediment core MD02-2496 offshore of Vancouver Island in the subarctic Northeastern Pacific to reconstruct the effects of ocean temperatures on the marine margin of the CIS during the deglacial. The ice rafted debris record suggests an increase in calving events that coincide with the retreat of the CIS beginning around 17 ka. From 50 to 10 ka, surface ocean temperature and $\delta^{18}O_{seawater}$ are compared with core sites to the south along the California margin, to examining the relative changes in surface ocean characteristics during Dansgaard-Oeschger events. Warm, relatively saline waters dominate offshore during these intervals, perhaps as a result of increased tropical waters from the south advected northward by the relative strengthening of the California Undercurrent.

Chapter 4 is a characterization of sediments in modern Arctic sea ice from sites in the northern Canadian Arctic Archipelago and offshore from Point Barrow, AK. Sea ice aggregates sediments entrained during sea ice formation and may therefore contribute to surface ocean Fe concentrations. In Chapter 4, elemental data from sea ice cores collected from shallow coastal regions in the Beaufort/Chukchi Sea and the Canadian Arctic are presented, with the potentially bioavailable pool of filterable and particulate Fe from sea ice sediments in these regions.

Chapter 1

Introduction

1. Sediment geochemistry

An estimated 6 to11 billion metric tons of sediment accumulate in ocean basins per year, constituting a vast potential archive of information about climate conditions in the surface ocean and near shore regions (Bradley, 2015). The geochemistry of marine sediments can be applied to address a variety of climate processes both in past and present settings. Marine sediments are primarily of biogenic or terrigenous origin. Biogenic sediments generated from the calcareous skeletal remains of organisms are often formed in equilibrium with seawater geochemistry and can be utilized to reconstruct past ocean processes such as circulation, temperature and salinity, dissolved oxygen, trace metal concentrations, and changes in export production. Calcareous skeletons formed in both surface (planktonic) and bottom water (benthic) environments are most commonly used to infer paleoclimate via $\delta^{18}O_{calcite}$, characterization of species assemblages over time, and Mg/Ca ratios that can be used to reconstruct temperatures and to extract $\delta^{18}O_{seawater}$ (Lea, 2014).

Terrigenous sediments can often be applied to a different set of climate-related questions such as relative aridity, prevailing wind paths/strength, and the relative importance of different sediment transport pathways such as river runoff, ice rafting, and aeolian. The geochemistry of terrigenous sediments may also be used to trace sediment provenance using radiogenic isotope

signatures, rare earth element enrichment patterns, and trace element abundances. These in addition to grain size analyses can indicate transport mechanisms and distance.

In addition to being passive records of climate information, sediments can play an active role in biogeochemical cycling both in the past and in modern systems. In high nitrogen/low chlorophyll (HNLC) regions like the Southern Ocean, iron (Fe) is an important limiting nutrient to primary productivity. Iron has a low solubility in seawater and is found at low concentrations throughout the ocean. Deep ocean sources of dissolved Fe come from sediment dissolution at continental margins, and from submarine hydrothermalism. Iron is thought to be delivered to the surface ocean primarily via mineral dust, but increasingly other sediment sources recognized to be important such as glacial weathering, ice rafted sediments, and sea ice that can act as a sediment reservoir, melting in spring and delivering nutrients during incipient blooms (Martin, 1990; Tovar-Sánchez et al., 2010; Raiswell, 2011).

Chapters 2 and **3** examine past ice-ocean-atmospheric in the Northeastern Pacific Ocean using the Mg/Ca ratios in biogenic sediments as a proxy for sea surface temperatures (SSTs). **Chapter 4** is a study of modern sediments to better understand the role of Arctic sea ice sediments in surface ocean geochemistry and Fe bioavailability and cycling.

2. Ice sheet-ocean temperature interactions

Changes in ocean circulation and advection of warm ocean waters have been invoked as a mechanism for significant ice sheet retreat during deglaciation at Termination 1 (Marcott et al., 2011; Davies et al., 2011; Jennings et al., 2015), and have been increasingly observed in modern ice sheet retreat and loss (Motyka et al., 2003; Steig et al., 2009; Rignot et al., 2010; Joughin et al., 2012; Rignot et al., 2012; Xu et al., 2012). Reconstructions of past ice sheet mass balance changes have focused on the larger Laurentide, Greenland, and Antarctic Ice Sheets, but there is

also growing interest in understanding processes affecting the western component of the North American ice sheet, the Cordilleran Ice Sheet (CIS) and the details of its retreat. The CIS is thought to have been a temperate, wet based ice sheet with a marine margin made up of ice grounded on the continental shelf and coastal tidewater glaciers (Alley and Chatwin, 1979; Mosher and Hewitt, 2004). At maximum extent (local last glacial maximum, ~18 ka), it was 900 km wide with an area of 1.5 million km^2 reaching from southern Alaska to the north, through the Yukon Territory and British Columbia to Washington State, Idaho, and Montana in the south, and as far eastward as the Rocky Mountains (Margold et al., 2013). Studies from the CIS interior have posited that the CIS decayed from downwasting and stagnation, and that the marine margin retreated as a result of eustatic sea level rise (Clague and James, 2002). Recent work suggests that the CIS ice divide shifted west to the Coast Mountains early in the deglaciation, and that the western margin of the ice sheet was removed rapidly by calving which would increase ice discharge and lower ice profiles to the west of the Coast Mountains (Hendy and Cosma 2008; Margold et al., 2012).

In **Chapter 2**, to better understand processes driving ice removal from the southern extent of the CIS marine margin during last deglaciation, planktonic foraminiferal Mg/Ca-based ocean temperature records were generated from glaciomarine sediments at deep sea core MD02-2496, sited offshore of Vancouver Island in the Northeastern Pacific Ocean. These ocean temperature reconstructions are compared with IRD records (Hendy and Cosma, 2008) that are evidence for calving events from the same sediment core to determine the relative timing of IRD discharge and ocean warming through the deglacial. This chapter was published in *Earth and Planetary Science Letters* in October 2014 (Taylor et al., 2014).

3. Teleconnections and abrupt climate change

In **Chapter 3**, the Mg/Ca-based temperature reconstruction from ocean sediment core MD02-2496 is extended, spanning 10-50 ka. This interval spans Marine Isotope Stage 3 (MIS 3), the deglacial transition, and the onset of the Holocene. The last glacial period, MIS 3, is characterized by abrupt, millennial scale climate variability, which is thought to originate in the North Atlantic Ocean. Dansgaard-Oeschger interstadials (DOIs) are rapid warming events first recognized in the Greenland Ice cores (Johnsen et al., 1992; Dansgaard et al., 1993). The cause of DOIs is still an area of active research, although most recent hypotheses are converging on some combination of changes in the strength of Atlantic Meridional Overturning Circulation (AMOC) and the extent of sea ice in the northern North Atlantic (Li et al., 2010; Petersen et al., 2013; Zhang et al., 2015). Evidence of DOIs has been found in high-resolution records further afield in terrestrial and lower latitude sites (Schulz et al., 1998; Wang et al., 2001; Schmidt et al., 2006; Leduc et al., 2007; Deplazes et al., 2013), and in the northeastern Pacific Ocean (Behl and Kennett, 1996; Hendy and Kennett, 1999; Hendy et al., 2004; Hendy et al., 2010; Pak et al., 2012), and an outstanding question is how widespread are the effects of DOIs and by what means are they teleconnected from their presumed point of origin.

The sedimentation rate at MD02-2496 was high enough during MIS 3 to capture millennial to sub-centennial climate events like Dansgaard-Oeschger. Sediment cores to the south have found evidence of bottom water oxygenation changes, benthic foraminiferal assemblage changes and SST warming during DOIs (Behl and Kennett, 1996; Cannariato and Kennett, 1999; Hendy and Kennett, 2000; Hendy et al., 2010; Pak et al., 2012; Ohkushi et al., 2013). In **Chapter 3**, relative changes in $\delta^{18}O_{calcite}$ and Mg/Ca-based SSTs from foraminifera, reconstructed $\delta^{18}O_{seawater}$ and bulk sediment $\delta^{15}N$ are analyzed to place the northeastern Pacific Ocean in better context in terms of changing sea surface characteristics in response to North

Atlantic climate forcing. This chapter is currently in revision with *Paleoceanography* (Taylor et al., in revision).

4. Modern sea ice processes

In **Chapter 4**, modern processes are explored using sediments entrained in Arctic sea ice. Arctic sea ice extent is in rapid decline, with summer minimum extent reduced from 7.0-7.5 million km^2 to 3.5-4.5 million km^2 since 1979 (Comiso et al., 2008), and thicker multi year pack ice replaced by first year ice (Maslanik et al., 2011). Loss of sea ice is driven by anthropogenic warming which is amplified in the Arctic through surface albedo feedbacks (Post et al., 2013). It is unclear what the effects of sea ice thinning and less sea ice cover will have on Arctic biological production. Recent estimates indicate a 20% increase (8.1 Tg C yr^{-1}) in net primary productivity between 1998 and 2009 (Arrigo and van Dijken, 2011), however these estimates do not take into account changes in community structure that can affect ecosystem function. Sea ice acts as an inhibitor to primary productivity by attenuating solar radiation to phytoplankton living beneath the ice, but also functions as habitat to sea ice algae and diverse microorganisms (Arrigo, 2014). Moreover the surface ocean phytoplankton community structure is shifting from nanoplankton (2 to 20 μm) to picoplankton (< 2 μm) dominated in many regions (Lasternas and Agusti, 2010), which may lead to less export from the surface mixed layer and a less efficient Arctic food web in future (Li et al., 2009).

Release of phytoplankton from the light limitations of permanent sea ice cover may increase productivity, but nutrient availability is another important factor—large-scale spatial heterogeneity in Arctic is dependent primarily on nitrogen supply (Tremblay and Gagnon 2009). With increased freshwater input to the Arctic Ocean, from runoff and sea ice melt, there is increased stratification that can restrict nutrient flux to surface waters (Bergeron and Tremblay,

2014), and a deepening of the nitracline in the Canadian Basin has been documented since 2003 (McLaughlin et al., 2010). In shallow coastal regions, nitrate concentrations are projected to increase commensurate with enhanced winds and upwelling.

The main factors known to limit primary productivity are light, especially in spring, and nitrate as it is drawn down throughout the growing season. It is not known whether the micronutrient Fe limits productivity in some regions of the Arctic (Taylor et al., 2013). Arctic primary producers may have a relatively high cellular Fe demand for assimilation of nitrate as well as photosynthesis under low light conditions (Taylor et al., 2013). Sea ice may have elevated concentrations of dissolved and particulate metals relative to seawater because it aggregates dust and ocean sediments during formation in the fall and throughout winter. Thus sea ice may contribute to surface ocean Fe concentrations during the early spring melt when surface nitrate concentrations are relatively high, especially in coastal regions (Aguilar-Islas et al., 200; Klunder et al., 2012; Wang et al., 2014). In **Chapter 4**, elemental data from sea ice cores collected from shallow coastal regions in the Beaufort/Chukchi Sea and the Canadian Arctic are presented, and sediment digestions constrain the potentially bioavailable pool of Fe from sea ice sediments in these regions.

References

Aguilar-Islas, A. M., R. D. Rember, C. W. Mordy, and J. Wu (2008), Sea ice-derived dissolved iron and its potential influence on the spring algal bloom in the Bering Sea, *Geophysical Research Letters*, *35*(24), L24601.

Alley, N. F., and S. C. Chatwin (1979), Late Pleistocene history and geomorphology, southwestern Vancouver Island, British Columbia, *Canadian Journal of Earth Sciences*, *16*(9), 1645-1657.

Arrigo, K. R. (2014), Sea Ice Ecosystems, *Annual Review of Marine Science*, *6*(1), 439-467.

Arrigo, K. R., and G. L. van Dijken (2011), Secular trends in Arctic Ocean net primary production, *Journal of Geophysical Research*, *116*(C9), C09011.

Behl, R. J., and J. P. Kennett (1996), Brief interstadial events in the Santa Barbara basin, NE Pacific, during the past 60 kyr, *Nature*, *379*(18), 243-246.

Bergeron, M., and J. É. Tremblay (2014), Shifts in biological productivity inferred from nutrient drawdown in the southern Beaufort Sea (2003–2011) and northern Baffin Bay (1997–2011), Canadian Arctic, *Geophysical Research Letters*, *41*, 3979-3987.

Bradley, R. S. (2015), *Marine Sediments*, 3 ed., 195-277 pp., Elsevier Inc.

Cannriato, K. G., and J. P. Kennett (1999), Climatically related millennial-scale fluctuations in strength of California margin oxygen-minimum zone during the past 60 k.y., *Geology*, *27*, 975-978.

Clague, J. J., and T. S. James (2002), History and isostatic effects of the last ice sheet in southern British Columbia, *Quaternary Science Reviews*, *21*, 71-87.

Comiso, J. C., C. L. Parkinson, R. Gersten, and L. Stock (2008), Accelerated decline in the Arctic sea ice cover, *Geophysical Research Letters*, *35*(1), L01703.

Dansgaard, W., S. J. Johnsen, and H. B. Clausen (1993), Evidence for general instability of past climate from a 250-kyr ice-core record, *Nature*, *364*, 218-220.

Davies, M. H., A. C. Mix, J. S. Stoner, J. A. Addison, J. Jaeger, B. Finney, and J. Wiest (2011), The deglacial transition on the southeastern Alaska Margin: Meltwater input, sea level rise, marine productivity, and sedimentary anoxia, *Paleoceanography*, *26*(2), PA2223.

Deplazes, G., et al. (2013), Links between tropical rainfall and North Atlantic climate during the last glacial period, *Nature Geoscience*, *6*(3), 213-217.

Hendy, I. L. (2010), The paleoclimatic response of the Southern Californian Margin to the rapid climate change of the last 60ka: A regional overview, *Quaternary International*, *215*(1-

2), 62-73.

Hendy, I. L., and T. Cosma (2008), Vulnerability of the Cordilleran Ice Sheet to iceberg calving during late Quaternary rapid climate change events, *Paleoceanography*, *23*, PA2101.

Hendy, I. L., and J. P. Kennett (1999), Latest Quaternary North Pacific surface-water responses imply atmosphere-driven climate instability, *Geology*, *27*(4), 291-294.

Hendy, I. L., and J. P. Kennett (2000), Dansgaard-Oeschger Cycles and the California Current System: Planktonic foraminiferal response to rapid climate change in Santa Barbara Basin, Ocean Drilling Program Hole 893A, *Paleoceanography*, *15*(1), 30-42.

Hendy, I. L., T. F. Pedersen, J. P. Kennett, and R. Tada (2004), Intermittent existence of a southern Californian upwelling cell during submillennial climate change of the last 60 kyr, *Paleoceanography*, *19*(3), PA3007.

Jennings, A., J. Andrews, C. Pearce, L. Wilson, and S. Ólfasdótttir (2015), Detrital carbonate peaks on the Labrador shelf, a 13-7ka template for freshwater forcing from the Hudson Strait outlet of the Laurentide Ice Sheet into the subpolar gyre, *Quaternary Science Reviews*, *107*(C), 62-80.

Johnsen, S. J., H. B. Clausen, W. Dansgaard, K. Fuhrer, N. Gundestrup, H. C. U, P. Iversen, J. Jouzel, B. Stauffer, and J. P. Steffensen (1992), Irregular glacial interstadials recorded in a new Greenland ice core, *Nature*, *359*, 311-313.

Joughin, I., B. E. Smith, I. M. Howat, D. Floricioiu, R. B. Alley, M. Truffer, and M. Fahnestock (2012), Seasonal to decadal scale variations in the surface velocity of Jakobshavn Isbrae, Greenland: Observation and model-based analysis, *Journal of Geophysical Research*, *117*(F2), F02030.

Klunder, M. B., D. Bauch, P. Laan, H. J. W. de Baar, S. van Heuven, and S. Ober (2012), Dissolved iron in the Arctic shelf seas and surface waters of the central Arctic Ocean: Impact of Arctic river water and ice-melt, *Journal of Geophysical Research*, *117*(C1), C01027.

Lasternas, S., and S. Agustí (2010), Phytoplankton community structure during the record Arctic ice-melting of summer 2007, *Polar Biology*, *33*(12), 1709-1717.

Lea, D. W. (2014), *Elemental and Isotopic Proxies of Past Ocean Temperatures*, 2 ed., 373-397 pp., Elsevier Ltd.

Leduc, G., L. Vidal, K. Tachikawa, F. Rostek, C. Sonzogni, L. Beaufort, and E. Bard (2007), Moisture transport across Central America as a positive feedback on abrupt climatic changes, *Nature*, *445*(7130), 908-911.

Li, C., D. S. Battisti, and C. M. Bitz (2010), Can North Atlantic Sea Ice Anomalies Account for

Dansgaard–Oeschger Climate Signals?*, *Journal of Climate*, *23*(20), 5457-5475.
Li, W. K. W., F. A. McLaughlin, C. Lovejoy, and E. C. Carmack (2009), Smallest Algae Thrive As the Arctic Ocean Freshens, *Science*, *326*(5952), 539-539.

Marcott, S. A., et al. (2011), Ice-shelf collapse from subsurface warming as a trigger for Heinrich events, *Proceedings of the National Academy of Sciences*, *108*(33), 13415-13419.

Margold, M., K. N. Jansson, J. Kleman, A. P. Stroeven, and C. J. J (2013), Retreat pattern of the Cordilleran Ice Sheet in central British Columbia at the end of the last glaciation reconstructed from glacial meltwater landforms, *Boreas, 42*, 830-847.

Martin, J., J. É. Tremblay, and N. M. Price (2012), Nutritive and photosynthetic ecology of subsurface chlorophyll maxima in Canadian Arctic waters, *Biogeosciences*, *9*(12), 5353-5371.

Maslanik J., J. Stroeve, C. Fowler, and W. Emery (2011), Distribution and trends in Arctic sea ice age through spring. *Geophysical Research Letters*, *35*, L13502

McLaughlin, F. A., and E. C. Carmack (2010), Deepening of the nutricline and chlorophyll maximum in the Canada Basin interior, 2003-2009, *Geophysical Research Letters*, *37*(24), L24602.

Mosher, D. C., and A. T. Hewitt (2004), Late Quaternary deglaciation and sea-level history of eastern Juan de Fuca Strait, Cascadia, *Quaternary International*, *121*, 23-39.

Motyka, R. J., L. Hunter, K. A. Echelmeyer, and C. Connor (2003), Submarine melting at the terminus of a temperate tidewater glacier, LeConte Glacier, Alaska, U.S.A., *Annals of Glaciology*, *36*, 57-65.

Ohkushi, K., J. P. Kennett, C. M. Zeleski, S. E. Moffitt, T. M. Hill, C. Robert, L. Beaufort, and R. J. Behl (2013), Quantified intermediate water oxygenation history of the NE Pacific: A new benthic foraminiferal record from Santa Barbara basin, *Paleoceanography*, *28*(3), 453-467.

Pak, D. K., D. W. Lea, and J. P. Kennett (2012), Millennial scale changes in sea surface temperature and ocean circulation in the northeast Pacific, 10–60 kyr BP, *Paleoceanography*, *27*(1), PA1212.

Petersen, S. V., D. P. Schrag, and P. U. Clark (2013), A new mechanism for Dansgaard-Oeschger cycles, *Paleoceanography*, *28*, 1-7.

Post, E., U. S. Bhatt, C. M. Bitz, J. F. Brodie, T. L. Fulton, M. Hebblewhite, J. Kerby, I. Stirling, and D. A. Walker (2013), Ecological Consequences of sea-ice decline, *Science*, *341*(6145), 519-524.

Raiswell, R. (2011), Iceberg-hosted nanoparticulate Fe in the Southern Ocean Mineralogy,

origin, dissolution kinetics and source of bioavailable Fe, *Deep-Sea Research Part II*, *58*(11-12), 1364-1375.

Rignot, E., I. Fenty, D. Menemenlis, and Y. Xu (2012), Spreading of warm ocean waters around Greenland as a possible cause for glacier acceleration, *Annals of Glaciology*, *53*(60), 257-266.

Rignot, E., M. Koppes, and I. Velicogna (2010), Rapid submarine melting of the calving faces of West Greenland glaciers, *Nature Geoscience*, *3*, 187-191.

Schmidt, M. W., M. J. Vautravers, and H. J. Spero (2006) Rapid subtropical North Atlantic salinity oscillations across Dansgaard-Oeschger cycles. *Nature 443*, 561–564.

Schulz, H. and U. von Rad (1998) Correlation between Arabian Sea and Greenland climate oscillations of the past 110,000 years. *Nature 393*, 54–57.

Steig, E. J., D. P. Schneider, S. D. Rutherford, M. E. Mann, J. C. Comiso, and D. T. Shindell (2009), Warming of the Antarctic ice-sheet surface since the 1957 International Geophysical Year, *Nature*, *457*(7228), 459-462.

Taylor, M. A., I. L. Hendy, and D. K. Pak (2014), Deglacial ocean warming and marine margin retreat of the Cordilleran Ice Sheet in the North Pacific Ocean, *Earth and Planetary Science Letters*, *403*(C), 89-98.

Taylor, M. A., I. L. Hendy, and D. K. Pak (in revision), The California Current System as a transmitter of millennial scale climate change on the northeastern Pacific margin from 10-50 ka, *Paleoceanography*.

Taylor, R. L., D. M. Semeniuk, C. D. Payne, J. Zhou, J.-É. Tremblay, J. T. Cullen, and M. T. Maldonado (2013), Colimitation by light, nitrate, and iron in the Beaufort Sea in late summer, *Journal of Geophysical Research: Oceans*, *118*(7), 3260-3277.

Tovar-Sánchez, A., C. M. Duarte, J. C. Alonso, S. Lacorte, R. Tauler, and C. Galbán-Malagón (2010), Impacts of metals and nutrients released from melting multiyear Arctic sea ice, *Journal of Geophysical Research*, *115*(C7), C07003.

Tremblay, J. É. and J. Gagnon (2009), The effects of irradiance and nutrient supply on the productivity of Arctic waters: a perspective on climate change, in: Influence of Climate Change on the Changing Arctic and Sub-Arctic Conditions, edited by: Nihoul, J. C. J. and Kostianoy, A. G., Nato Science for Peace and Security Series C – Environmental Security, Elsevier, 73–93.

Wang, Y. J. et al. (2001) A high-resolution absolute-dated Late Pleistocene monsoon record from Hulu Cave, China. *Science 294*, 2345–2348.

Wang, S., D. Bailey, K. Lindsay, J. K. Moore, and M. Holland (2014), Impact of sea ice on the

marine iron cycle and phytoplankton productivity, *Biogeosciences*, *11*(17), 4713-4731.

Xu, Y., E. Rignot, D. Menemenlis, and M. Koppes (2012), Numerical experiments on subaqueous melting of Greenland tidewater glaciers in response to ocean warming and enhanced subglacial discharge, *Annals of Glaciology*, *53*(60), 229-234.

Zhang, X., G. Lohmann, G. Knorr, and C. Purcell (2015), Abrupt glacial climate shifts controlled by ice sheet changes, *Nature*, *512*(7514), 290-294.

Chapter 2

Deglacial ocean warming and marine margin retreat of the Cordilleran Ice Sheet in the North Pacific Ocean

Abstract

A new, high-resolution planktonic foraminiferal Mg/Ca-based ocean temperature record has been generated for deep sea core MD02-2496, sited offshore of Vancouver Island, Western Canada during the last deglaciation (21-12 ka). The relationship between Cordilleran Ice Sheet (CIS) retreat and changing regional ocean temperatures has been reconstructed through glaciomarine sediments in MD02-2496 that capture tidewater glacier response to surface ocean thermal forcing. At CIS maximum extent, the marine margin of the ice sheet advanced onto the continental shelf. During this interval, ocean temperatures recorded by surface ocean dwelling *Globigerina bulloides* remained a relatively constant ~7.5°C while subsurface dwelling *Neogloboquadrina pachyderma* (s.) recorded temperatures of ~5°C. These ocean temperatures were sufficiently warm to induce significant melt along the tidewater ice terminus similar to modern Alaskan tidewater glacial systems. During the deglacial retreat of the CIS, the *N. pachyderma* temperature record shows two distinct warming steps of ~2 and 2.5˚C between 17.2-16 and 15.5-14 ka respectively, coincident with ice rafting events from the CIS, while *G. bulloides* records an ~3˚C warming from 15 to14 ka. We hypothesize that submarine melting resulting from relatively warm ocean temperatures was an important process driving ice removal from CIS tidewater glaciers during the initial stages of deglaciation.

1. Introduction

Recent increases in ice discharge from the Greenland tidewater glaciers and Antarctic Ice Shelves (Rignot et al., 2012; Rignot et al., 2014) indicate that the effects of ocean thermal forcing on marine margin ice may be underestimated (Howat, 2007). Over the last decade, observed submarine melting of modern tidewater glaciers in response to warming sea surface temperatures have refocused investigations of ice sheet responses to climate forcing (Joughin et al., 2012; O'Leary and Christofferson, 2013; Seale et al., 2011; Straneo et al., 2010; Xu et al., 2012). For example Marcott et al. (2011) causally linked subarctic North Atlantic intermediate water warming of 2˚C at 17-16.5 ka to the collapse of the Laurentide Ice Sheet (LIS) resulting in the discharge of icebergs during Heinrich Event 1 (H1). Similarly ocean temperatures may have induced rapid climate change through the destabilization of the LIS during interstadials of the last glacial interval, wherein ocean warming caused rapid sea ice melt and ice shelf collapse, and the subsequent gradual cooling was then paced by ice shelf regrowth (Petersen et al., 2013).

Ocean warming may have operated similarly at the marine margin of the Cordilleran Ice Sheet (CIS) in Western Canada, where ice rafted debris (IRD) deposition (Blaise et al., 1990; Cosma and Hendy, 2008; Hendy and Cosma, 2008) was coincident with CIS retreat at ~17 ka (Clague and James, 2002; Mosher and Hewitt, 2004; Porter and Swanson, 1998). Eustatic sea level rise has been implicated in destabilization and retreat of the marine margin CIS (Clague and James; 2002, Hendy and Cosma, 2008), but the role of ocean thermal forcing has not been directly investigated.

New high-resolution stable oxygen isotope and Mg/Ca-based ocean temperature reconstructions from deep-sea core MD02-2496 (48°58'47"N, 127°02'14"W; 38.38 m core length; 1243 m water depth) for the last deglacial interval (21 to 12 ka) have been generated

from ocean surface dwelling planktonic foraminifera *Globigerina bulloides* and subsurface dwelling *Neogloboquadrina pachyderma* (sinistral), providing a unique opportunity to explore the relationship between surface ocean thermal forcing and ice sheet behavior from 21 to 12 ka. Coeval changes in ocean temperatures, $\delta^{18}O_{seawater}$ and glaciomarine sediment deposition in MD02-2496 provide a unique opportunity to constrain regional marine processes contributing to the timing and rate of CIS retreat from the Vancouver continental margin, Additionally planktonic $\delta^{18}O_{seawater}$ records enable the possible detection of isotopically light meltwater discharge. Evidence for meltwater pulses into the Pacific Ocean from the CIS have proven elusive, even though large glacial lake outburst floods from proglacial Lake Missoula emptied into the North Pacific via the Columbia River (Brunner et al., 1999; Lopes and Mix, 2009; Normark and Reid, 2003). However recent studies in the North Pacific have found $d^{18}O$ anomalies suggestive of CIS meltwater input into the Gulf of Alaska during the late deglacial (Davies et al., 2011).

Here we use the coincidence of warming ocean temperatures and ice rafting debris (IRD) to suggest that submarine melting played a role in the initial deglacial retreat of the marine margin of the CIS between 17- 14.8 ka (Hendy and Cosma, 2008). Retreat from the continental shelf back onto land occurred rapidly, with ice retreating 250 km within ~3 kyr (Clague, 1981; Clague and James, 2002; Porter and Swanson, 1998), supported by the rapid postglacial rebound of Vancouver Island (James et al., 2009). Increasing deglacial ocean temperatures could have impacted calving rates primarily through submarine melting at the glacial terminus. This process promotes calving both by undercutting subaerial ice, and direct melting of the ice terminus (Motyka et al., 2003; Rignot et al., 2010). The relationship between thermal forcing and submarine melting is expected to be linear, such that several degrees of surface ocean warming

could result in melt rates of hundreds of meters in a single season (Jenkins, 2011; Xu, 2012). However, such melting is restricted to tidewater outlet glaciers, where the terminus is submerged and susceptible to surface ocean warming. Understanding how surface ocean temperatures may have contributed to the destabilization of the marine margin of the CIS provides new insight into the deglacial history of the CIS.

1.1 Core site and modern setting

The MD02-2496 core site lies on the continental slope, within an oceanographic region where surface ocean circulation is presently highly variable (Figure 2.1). At ~50°N the eastward flowing North Pacific Current (NPC) bifurcates into the Alaskan Current System to the north and the California Current System to the south (Cummins and Freeland, 2007). It is likely the NPC bifurcation moved equatorward with the Westerlies during the last glacial (Nagashima et al., 2007; COHMAP, 1988). The modern annual average surface salinity at the site is 32.5 ‰, and average sea surface temperature is 12°C, ranging from 8°C in winter to 14°C in summer (Antonov et al., 2005; Locarnini et al., 2005). Modern ocean temperature variability between core site MD02-2496 and the reconstructed CIS grounding line can be assessed using Line PAPA temperature surveys from 125˚ W to 128˚ W (Figure 2.1). The transect contains a surface ocean temperature range (0-10 m) from 11.4˚C to 14˚C, while temperatures at depth (40-50 m) range from 8.2˚C to 10.2˚C during the summer season (May-September). If the upwelling-dominated summer months are removed from the average, cooling at the margin is reduced by ~1˚C, from 11.2˚C at the surface and 8.8˚C at depth, to 12.1˚C at the surface and 9.3˚C at depth on the shelf edge (Figure 2.1 B and C) (Crawford et al., 2007). The seasonal thermocline depth ranges from 10 m in summer to 50 m in winter (Peña et al., 1999; Thompson and Fine, 2003).

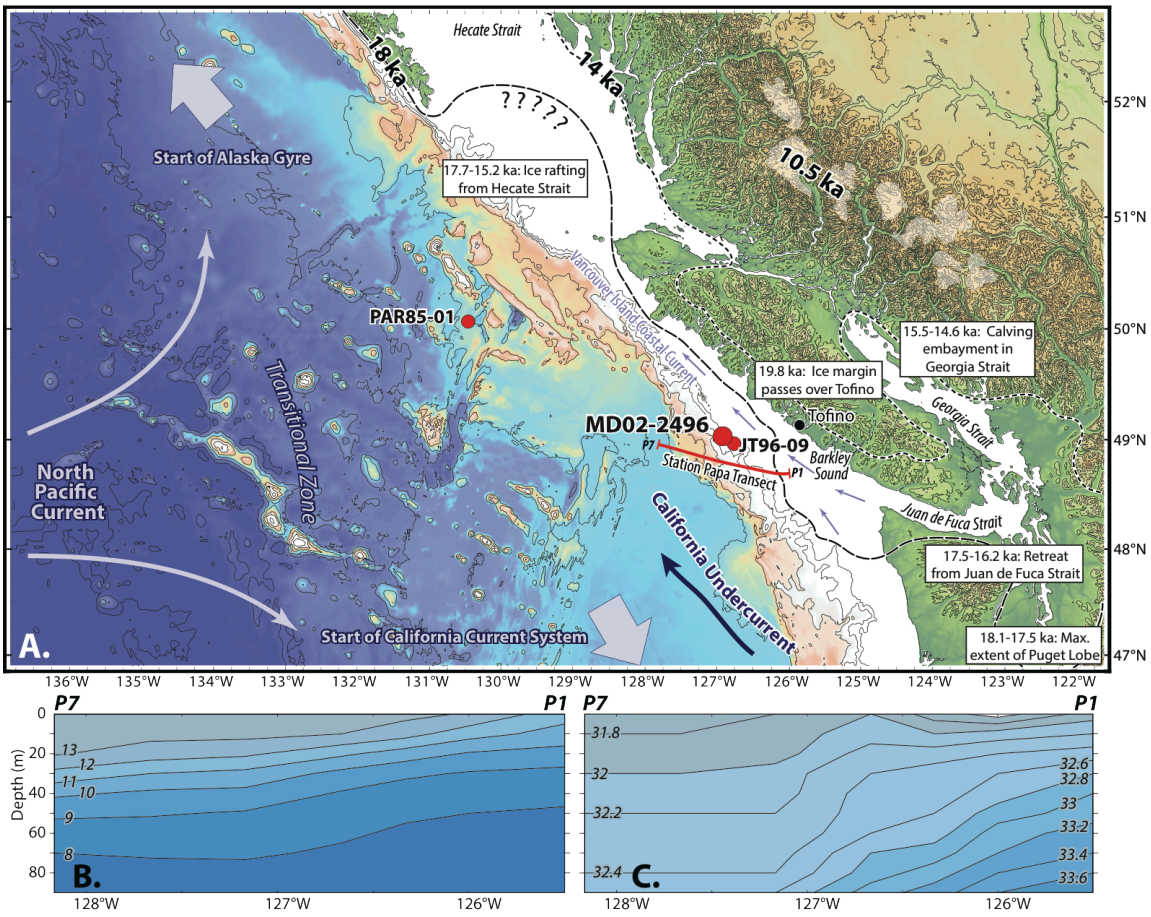

Figure 2.1
Location of core sites (red circles) MD02-2496 (48°58'48"N, 127°02'14"W, 1243 m water depth) and JT96-09 (Kienast and McKay, 2001) and PAR85-01 (Blaise et al., 1990) offshore from Vancouver Island. Black dashed line indicates maximum extent of the Cordilleran Ice Sheet at 19.5 ka (Clague and James, 2002). Dotted line marks the final ice retreat onto land at 14 ka (Hendy and Cosma, 2008). Arrows represent dominant modern current configurations, where the grey arrows represent the California and Alaskan Currents which extend from the continental slope to ~1000 km offshore. The blue arrow represents the core flow of the California Undercurrent, along the shelf break and at 200-300 m depth and upwelled onto the shelf. The small blue arrows show the northward coastal flow of the Vancouver Island Coastal Current, originating with the fresher water emanating from the Strait of Juan de Fuca. Station PAPA CTD survey transect is shown with a red line. Five years (2000-2005) of summer (May-September) season B) temperatures and C) salinities versus depth are presented along the Line PAPA longitudinal transect (http://www.pac.dfo-mpo.gc.ca/science/oceans/data-donnees/line-p/index-eng.html).

The summer season longshore coastal current system is composed of the California Current, the California Undercurrent, and the Vancouver Island Coastal Current (Masson and Fine, 2012). The core flow of the California Current is several hundred kilometers offshore, and the core of the poleward California Undercurrent flows over the continental slope, upwelling onto the shelf (Strub and James, 2002). Seasonal upwelling occurs after the spring transition

when wind forcing changes direction from southerly in winter to northerly dominance in summer around June-July (Hickey and Banas, 2008). Due to seasonal upwelling, summer coastal ocean temperatures are depressed relative to temperatures on the continental shelf edge (Crawford et al., 2007; Cummins and Masson, 2014). Modern nearshore currents on the continental shelf are driven by buoyancy forcing due to freshwater input from the Fraser River into the Georgia and Juan de Fuca Straits (Cummins and Masson, 1999). Fresh waters are tidally mixed with ocean currents entering the Straits, and this relative buoyant water flows northward out of the Straits over the continental shelf forming the Vancouver Island Coastal Current system (Cummins and Masson, 2014). The buoyancy driven current system described here would not have existed in its modern form during the LGM, when grounded ice on the Vancouver Island continental shelf filled the straits (Mosher and Hewitt, 2004) where tidal mixing would have occurred (Figure 2.1).

The southwestern margin of the CIS advanced in two ice lobes during the LGM: A smaller, land locked Puget Lobe flowing south between the Olympic Mountains and the Cascade Range, into the Puget lowlands (Booth et al., 2004); and a westward flowing Juan de Fuca Lobe that overtopped southern Vancouver Island transporting ice through the Juan de Fuca Strait across the continental shelf to the Pacific Ocean (Mosher and Hewitt, 2004; Stumpf et al., 2000; Figure 2.1). Grounded ice extended as far as the shelf break south of MD02-2496 (~49.5˚N) where ice from the Juan de Fuca Strait and the Barkley Sound coalesced into a large piedmont glacial lobe. The continental shelf extending ~55 km from the Juan de Fuca Strait is indented by 6 major submarine canyons (up to 300 m deep), some terminating at the shelf edge, likely scoured by the advancing Juan de Fuca Lobe (Alley and Chatwin, 1979). The southern Vancouver Island continental shelf is characterized by arcuate banks of exposed bedrock topped

by morainal/glacial materials providing evidence for this grounded ice lobe (~48˚30' N; Herzer and Bornhold, 1982). South of 49˚N flat-topped banks of unsorted glacial sediments that are possibly morainal features have been planed off by the modern tidally-driven coastal current system (Herzer and Bornhold, 1982). These described continental shelf features likely provided the morainal shoal (Herzer and Bornhold, 1982), which could have stabilized the marine margin of the CIS with tidewater outlet glaciers during its maximum extent (~20-17.5 ka; Porter and Swanson, 1998).

The development of an ice shelf on the Juan de Fuca lobe was unlikely. Mean annual temperatures must be <5℃ to stabilize an ice shelf (Benn et al., 2007) Modern mean annual temperatures in the Pacific Northwest are temperate (Meier and Post, 1987), however, LGM climate models predict cooler conditions by 4-8˚C (Bush et al., 1999; Otto-Bliesner et al., 2009; Seguinot et al., 2013). Under these conditions floating termini might be expected, however, an embayment is also necessary to protect the ice shelf from wave and storm activity. No such protection for an ice shelf is afforded beyond the Juan de Fuca Strait and fjords of Vancouver Island.

2. Methods

2.1 Radiocarbon age model and core chronology

Forty-seven mixed planktonic foraminiferal and bulk organic carbon radiocarbon dates were generated by Cosma et al., (2008). The original chronology for the deglacial has been modified using the MARINE13 calibration (Reimer et al., 2013) generating a new calendar-year-based chronology through the deglacial interval displayed in supplementary information. A constant regional reservoir correction (DR) of 402.7 ±50 years was assumed (Robinson and

Thompson, 1981). The definition of named climate events is based on the dating of northern European vegetation response during deglaciation (Mangerud et al., 1974).

Samples (2 cm) were collected at 5 cm intervals from 785 to 2025 cm (uncorrected) below core top in MD02-2496. Resolution of the sampling interval changes as a result of changing sedimentation rate within the core: between 21-19.4 ka, each interval represents 200 years (± 124), from 19.4-14.7 ka the sample interval resolution is 50 years (± 128), and from 14.7-12 ka the sedimentation rate decreases such that the sample resolution is 270 years (± 131).

2.2 Foraminiferal stable isotope analysis

Samples consisting of planktonic foraminiferal species *N. pachyderma* (s.) and *G. bulloides* were picked from the >125 μm fraction. 102 *N. pachyderma* and 103 *G. bulloides* samples were prepared using standard techniques for stable isotope analysis. Samples were baked at 200°C under vacuum for 1 hour and dissolved at 76°C with anhydrous phosphoric acid in a Finnigan MAT Kiel device for analysis in a Finnigan MAT 251 triple collector isotope ratio mass spectrometer at the University of Michigan Stable Isotope Laboratory. Machine precision was <0.1 ‰ and replicate $\delta^{18}O$ values yielded a mean standard deviation of 0.14 ‰ for *G. bulloides*, and 0.149 ‰ for *N. pachyderma*. Samples are reported using standard δ notion relative to the Vienna Pee Dee Belemnite (VPDB) standard.

2.3 Foraminiferal Mg/Ca analysis

Samples were analyzed for major and trace metals (Ca, Mg, Sr, Fe, Mn). Approximately 60 individual *N. pachyderma* (s.) and 25 *G. bulloides* were picked to achieve an average sample weight of ~300 μg for each analysis. These analyses were performed on separately picked samples instead of splits from samples analyzed for $\delta^{18}O_{calcite}$. Poor carbonate preservation in the organic carbon-rich Holocene prevented Mg/Ca analysis for samples younger than~10 ka. Visual

inspection prior to analysis confirmed that foraminifera were well preserved prior to the Holocene. Samples were weighed and crushed before undergoing cleaning of contaminant phases via a multi-step protocol involving clay removal, and oxidative and reductive steps. (Martin and Lea, 2002). In this marginal basin environment, reductive cleaning is necessary to remove oxides potentially adsorbed after sedimentation. Although the reductive cleaning step can lead to sample loss due to dissolution, a cleaning study of *N. dutertrei*, which has a similar shell ultrastructure to *N. pachyderma*, indicated that reductive cleaning results in little lattice bound Mg loss (Bian and Martin, 2010). Cleaned samples were analyzed for trace metals using a Thermo-Finnigan Element II high resolution ICP-MS at the University of Michigan (Barker et al., 2003; Boyle and Keigwin, 1985; Keigwin and Boyle, 1989). The analytical precision of Mg/Ca based on 43 replicate analyses of external consistency standards is 0.074 mmol/mol (1 σ). The analytical precision for Mg/Ca splits (6 pairs), reflecting both analytical and sample-processing uncertainty is 0.16 mmol/mol (1 σ), corresponding to 1.5˚C uncertainty. 22% of samples were rejected due to low sample recovery (<10%), or high Mn/Ca and Fe/Ca ratios suggestive of sample contamination.

2.4 Mg/Ca-based ocean temperatures and $\delta^{18}O_{seawater}$ reconstructions

G. bulloides and *N. pachyderma* Mg/Ca values were converted to temperatures using the Elderfield and Ganssen, (2000) calibration equation derived from core-top samples over a latitudinal transect from 30˚ to 60˚ N. While this equation actually reconstructs the temperature at which foraminiferal calcification occurred, for simplicity we will refer to calcification temperatures hereafter as ocean temperatures. This calibration equation is based on multiple temperate and subpolar species (Mean annual temperature 8˚-22˚C) including both *G. bulloides* and *N. pachyderma* (s.):

$$Mg/Ca = 0.52 * e^{(0.10*Temperature)} \quad (\pm 0.7°C \text{ standard error}) \quad (1)$$

Other published calibration equations (Mashiotta et al., 1999; von Langen et al., 2005; Nürnberg et al., 1995; Kozdon et al., 2009) based on temperate and subpolar planktonic foraminiferal species have a similar exponential constant to the Elderfield and Ganssen (2000) calibration, therefore the choice of another calibration equation does not result in a significant difference in reconstructed temperature. As the species-specific *G. bulloides* Mg/Ca calibration equation (Mashiotta et al., 1999) is an extrapolation at the low temperatures observed at our study site, we opt to use a single calibration equation based on multiple temperate and subpolar species. In choosing a single calibration equation for both foraminiferal species, potential artifacts from propagated uncertainties in the species-specific calibration equations are avoided, but potential vital effects in the species-specific uptake of Mg relative to Ca are not. The use of species-specific calibration equations leads to *N. pachyderma* Mg/Ca temperatures that are approximately 1˚C cooler, while the *G. bulloides* temperature are approximately 0.5˚C warmer than the temperatures reconstructed using the Elderfield and Ganssen (2000) calibration, leading to a greater apparent difference in near-surface and sub-surface temperature reconstructions (Fig. S3). However, the temperature trends remain the same.

Mg/Ca-based reconstructed temperatures and the $\delta^{18}O$ of coeval samples were used to calculate $\delta^{18}O$-seawater during the deglacial era at MD02-2496. For this, we used the calibration for $\delta^{18}O$ of foraminiferal calcite and temperature detailed by Shackleton (1974):

$$T\ (°C) = 16.9 - 4.38\ (\delta^{18}O_{calcite} - \delta^{18}O_{seawater}) + 0.1\ (\delta^{18}O_{calcite} - \delta^{18}O_{seawater})^2 \quad (2)$$

$\delta^{18}O$ values were converted from VPDB to VSMOW by the addition of 0.2 ‰ (Marchitto et al., 2014). There is a reported offset of -0.5 to -1.6 ‰ when using Shackleton (1974) with *N. pachyderma*, which is the result of regional vital effects (Jonkers et al., 2013). The selection of a

different equation shifts the data by approximately -0.2 ‰ (e.g., Craig, 1965) or 0.4 ‰ (e.g., Kim and O'Neil, 1997), but does not change the trends reported. The effect of continental ice sheets on $\delta^{18}O_{seawater}$ was corrected for using the stacked benthic isotopic records (Waelbroeck et al. 2002) and incorporating a full glacial-interglacial shift of 1.1‰ (Chappell and Shackleton, 1986; Schrag et al, 1996).

3. Results

The dominant planktonic foraminiferal species in the subpolar waters of the Pacific Northwest are *N. pachyderma* (sinistral) and *G. bulloides*. *N. pachyderma* (dextral) is found in modern sediment traps, but almost entirely absent in pre-14 ka MD02-2496 sediments, likely because temperatures were cooler during the last glacial than the preferred 8-14°C range of the species (Sautter and Thunell, 1991; Reynolds and Thunell, 1985). *G. bulloides* are present from April to October, and *N. pachyderma* (both morphotypes) are present year round, with peak abundances in May and early June at the Station PAPA sediment trap (50˚N, 145˚W; Reynolds and Thunell, 1985). *G. bulloides* is tolerant of a wide temperature range (6-26°C) but dominates in cool upwelling conditions and is found predominately in surface waters (0-20 m; Kuroyanagi and Kawahata, 2004, Sautter and Thunell, 1986). The Mg/Ca and stable isotope geochemistry of *G. bulloides* in Southern California agrees with this preferred depth habitat (Sautter and Thunell, 1989; Pak et al., 2004). *N. pachyderma* (s.) prefers ocean temperatures cooler than 8°C and dominates the foraminiferal fauna in weakly stratified subpolar water (Reynolds and Thunell, 1986). In the Japan Sea, this species is associated with the pycnocline (~20-40 m; Kuroyanagi and Kawahata, 2004). At MD02-2496, within the range of depth habitats occupied by *N. pachyderma* and *G. bulloides*, the difference in ocean temperatures may range from 0-5˚C.

Since the uncertainty in Mg/Ca-reconstructed temperatures is ±1.5˚C, our data may not be able to detect significant difference in temperature at depths inhabited by these species.

3.1 Mg/Ca of *N. pachyderma* and *G. bulloides*

The Mg/Ca record of both planktonic foraminiferal species at MD02-2496 varies through time as illustrated in the running 1-sigma standard deviation envelope displayed in Fig. 2. The full range of Mg/Ca values recorded by both *N. pachyderma* and *G. bulloides* is ~1 mmol/mol with *G. bulloides* Mg/Ca values greater than *N. pachyderma* by 0.25 mmol/mol on average. *N. pachyderma* and *G. bulloides* Mg/Ca ratios are within the uncertainties of one another, and display similar trends. Average Mg/Ca ratios of both species decrease by 0.2 mmol/mol from the LGM (21 ka) to the interval when the CIS became proximal to the core site (19.5 ka). From 17-15 ka, the average Mg/Ca value of N. pachyderma increases by 0.2 mmol/mol from a minimum value of 0.7 mmol/mol. There is a second increase for both species of an average 0.3 mmol/mol at 14.7 ka (the initiation of the Bølling) to maximum values of 1.6 mmol/mol.

3.2 Reconstructed temperatures from *N. pachyderma* and *G. bulloides*

A nearby sediment trap study suggests that *N. pachyderma*- and *G. bulloides*-based proxy records should be biased towards recording the warmer season temperatures due to nutrient availability (Reynolds and Thunell, 1985). Surface dwelling foraminifera *G. bulloides* generally record warmer temperatures (2.7°C average, ranging from 4.1-12.1°C) than thermocline dweller *N. pachyderma* (temperatures range from 1.5-11.3°C) at MD02-2496 (Figure 2.2). The *G. bulloides* record a range of temperatures from 7.3-8.8°C from 21-14.7 ka. After the Bølling (14.7-12 ka) *G. bulloides* average temperatures indicate warming to 9.4°C. The *N. pachyderma* temperature record shows more variability during the glacial than the *G. bulloides* record with the coolest temperatures (average of 3.8°C) between 19.5-17.2 ka. During this interval, *N.*

pachyderma records temperatures ~4°C cooler than *G. bulloides*. *N. pachyderma* temperatures warm from ~3.5-5.5°C between 17.5-16.5. From 15.2 to 14.7 ka *G. bulloides* and *N. pachyderma* record similar temperatures (7-9°C), with a further warming of ~3°C from 15.5-14 ka. Throughout the record, changes in temperatures of both species are in phase with the exception of the pre-Bølling/Allerød warming. Here, warming in the *N. pachyderma* record occurs between

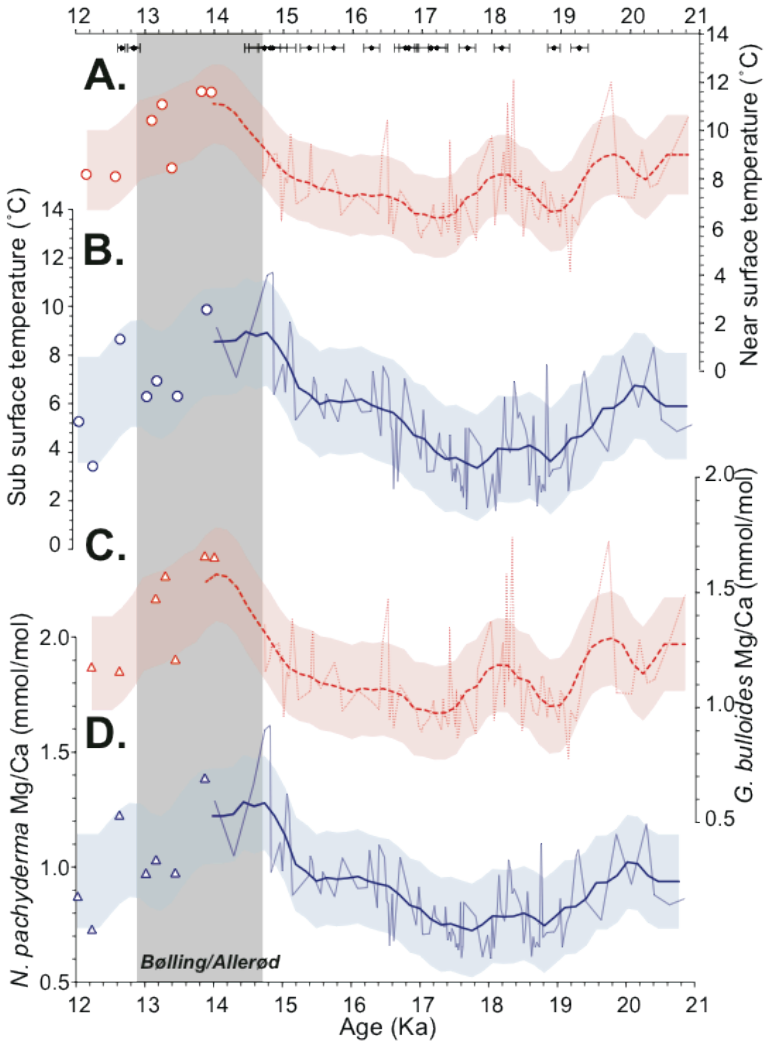

Figure 2.2
Calculated ocean temperatures (A) for *G. bulloides* (thin dotted red line and red circles) with smoothing (thick red dashed line) and *N. pachyderma* (s.) (thin blue line and blue circles) with smoothing (thick blue line). Calibrated radiocarbon tiepoints (black circles) with age model error are marked along the top axis. Measured Mg/Ca of the planktonic foraminifera species (C) *G. bulloides* (thin dotted red line and red triangles) and smoothed data (thick red dashed line), and (D) *N. pachyderma* (thin blue line and blue triangles) and smoothed data (thick blue line). Data were smoothed with a 150-year resampling and then a 5-point centered mean. Error envelope of 1 σ is calculated from a running standard deviation of samples.

16-15 ka, while warming of the *G. bulloides* record is gradual until after 15 ka, reaching peak values just after 14 ka.

3.3 $\delta^{18}O_{calcite}$ and reconstructed $\delta^{18}O_{seawater}$ of *N. pachyderma* and *G. bulloides*

$\delta^{18}O_{calcite}$ records are displayed in Figure 2.3A. The *N. pachyderma* $\delta^{18}O_{calcite}$ record has been presented previously in Hendy and Cosma, 2008. In comparison to temperature reconstructions of the planktonic foraminifera at MD02-2496, the $\delta^{18}O_{calcite}$ values display less variability (Figure 2.3A). From the LGM to 17.8 ka the $\delta^{18}O_{calcite}$ values of both species ranged from 3.3 to 2.4‰, increasing at 16.8 ka to maximum values of 3.4‰ (*N. pachyderma*) and 3.5‰ (*G. bulloides*). From 16.8 to 14.7 ka, $\delta^{18}O_{calcite}$ values gradually decrease by 0.6-0.3‰ to ~3‰, and to 2.4-2.8‰ by 12.2 ka.

The $\delta^{18}O_{seawater}$ record of both species follows Mg/Ca-reconstructed temperatures through time, where high $\delta^{18}O_{seawater}$ values correspond with warmer ocean temperatures (Figures 2.3B and 2.3C). Similar to reconstructed temperature, the *G. bulloides* reconstructed $\delta^{18}O_{seawater}$ demonstrates little variability, ranging in values from a minimum of -1.3‰ around 19 ka to a maximum value of 1.2‰ around 13.8 ka (Figure 2.3D). *N. pachyderma* $\delta^{18}O_{seawater}$ values range from minimum values of ~-2.0‰ at 19 ka to 1.0‰ at the initiation of the Bølling. Between 16-14 ka the $\delta^{18}O_{seawater}$ appear to be out of phase. Like the reconstructed temperatures, *N. pachyderma* $\delta^{18}O_{seawater}$ increases after 16 ka to peak at 15 ka, while *G. bulloides* increases begin ~15 ka and reaches peak values after 14 ka.

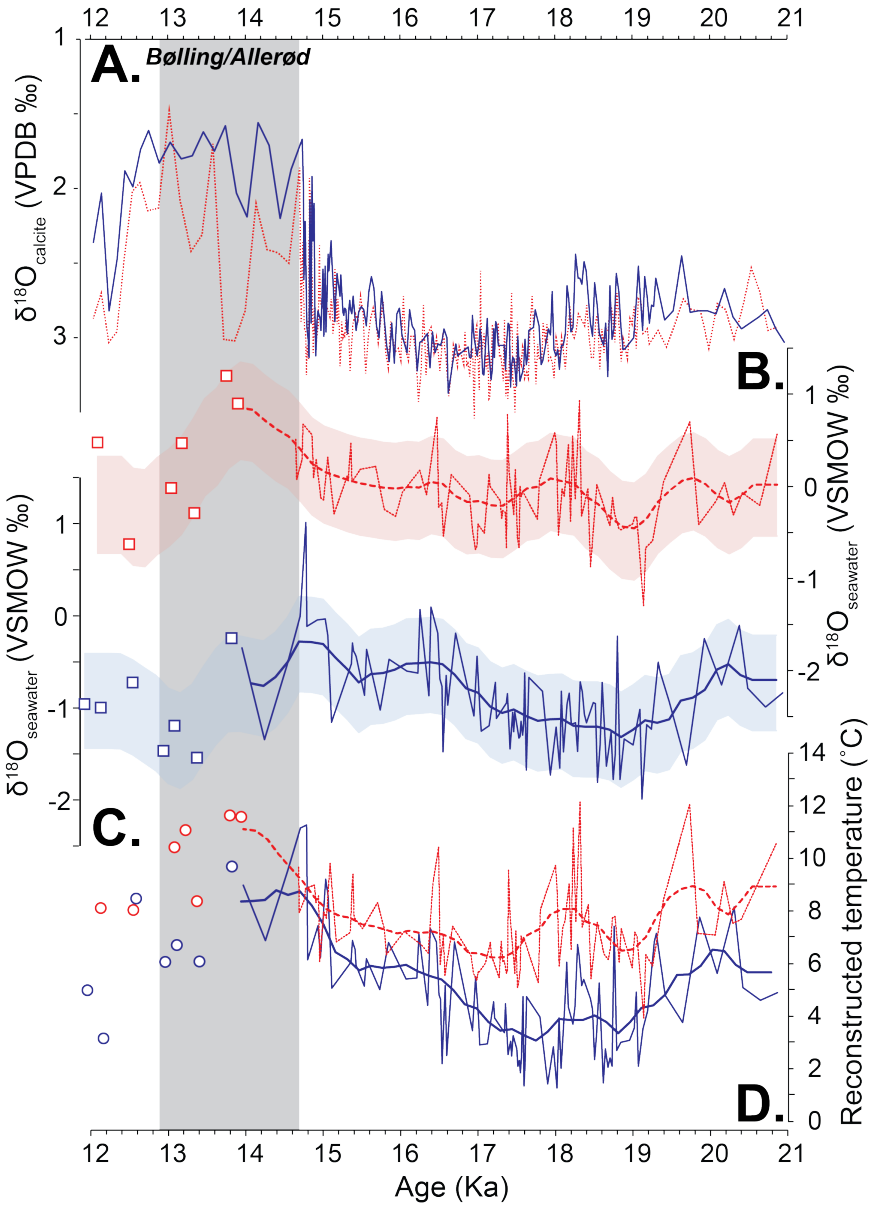

Figure 2.3
(A) *N. pachyderma* (blue line) and *G. bulloides* (red dotted line) $\delta^{18}O_{calcite}$ data (‰, Vienna Peedee belemnite (VPDB)) against calibrated calendar years. (B) Reconstructed *G. bulloides* (thin dotted red line and red squares) $\delta^{18}O_{seawater}$ (‰, Vienna Standard Mean Ocean Water (VSMOW)) with smoothing (thick red dashed line), and (C) *N. pachyderma* (thin blue line and blue squares) with smoothing (thick blue line). Data were smoothed with a 150-year resampling and then a 5-point centered mean. Error envelope of 1 σ is calculated from a running standard deviation of samples. (D) Calculated ocean temperatures for *N. pachyderma* (thin blue line and blue circles) with smoothed data (thick blue line) and *G. bulloides* (thin dotted red line and red circles) with smoothed data (thick red dashed line).

3.4 Vital and salinity effects on Mg/Ca-based temperature reconstructions

Mg/Ca values in *G. bulloides* and *N. pachyderma* (d.) tests from a Santa Barbara Basin sediment trap demonstrate good agreement with measured ocean temperatures and with

previously published culture-based Mg/Ca-temperature equations (Pak et al., 2004). A recent high latitude (59°N) North Atlantic sediment study shows that *G. bulloides* Mg/Ca and $\delta^{18}O_{calcite}$ follow summer surface ocean temperatures while the Mg/Ca of *N. pachyderma* (s) is invariant compared to $\delta^{18}O_{calcite}$ (Jonkers et al., 2013). An Arctic Mg/Ca temperature calibration study found, however, that *N. pachyderma* (s) $d^{18}O$-derived calcification temperatures deviate from the $d^{44/40}Ca$ and Mg/Ca temperature proxies (Kozdon et al., 2009). In contrast, in MD02-2496 sediments *N. pachyderma* (s.) Mg/Ca values vary through time. Additionally reconstructed temperatures produced from *N. pachyderma* test Mg/Ca closely follow those based on *G. bulloides* test Mg/Ca and another independent method of reconstructing temperature - alkenones (Kienast and McKay, 2001). These results suggest *N. pachyderma* (s.) Mg/Ca is sensitive to temperature change in the temperate-subpolar Northeast Pacific.

G. bulloides test Mg/Ca has no apparent salinity relationship based on core top calibrations in the Northeast Pacific, Southeast Atlantic, and North Atlantic (Martinez-Boti et al., 2011; Patton et al., 2011). Moreover, sediment trap data indicates salinity effects on other species increase Mg/Ca ratios at salinities (>36.5 ‰), significantly higher than average salinity in the North Pacific (~32.5 ‰) (Ferguson et al., 2008). Therefore any salinity bias is likely to be minor. Finally growth rate and specimen size can impact the relative Mg to Ca uptake in foraminiferal tests (Schmidt et al., 2004; Schmidt et al., 2008; Friedrich et al., 2012). *G. bulloides*, calculated Mg/Ca temperatures were shown to have varied by 4°C between the 100 μm and ~300 μm size fraction (Friedrich et al., 2012). In most species, Mg/Ca uptake decreases with increasing test size; therefore analysis of a narrow size fraction is preferred. In MD02-2496, the size fraction utilized was >125 μm, however, subpolar foraminiferal specimens fall within a

narrower size range than specimens found in warmer regions. Thus in MD02-2496 sediments test size-based bias is unlikely to be significant.

4. Discussion

Given the proximity of MD02-2496 to the CIS marine margin and the homogeneity of ocean surface temperatures along the modern 3˚ longitudinal transect (Fig. 1), reconstructed temperatures at the core site should approximate those at the ice margin. A late deglacial (~15.5 ka to present) alkenone-based temperatures reconstruction (core JT96-09; Fig. 1) from nearby on the continental slope of Vancouver Island supports the Mg/Ca-based temperatures reconstruction from MD02-2496 (Fig. 4) with temperatures of ~6˚C at 15.5 ka, increasing to ~8˚C at 14.5 ka, and ~9-10˚C by 14 ka (Kienast and McKay, 2001). Temperatures recorded by near-surface dwelling planktonic foraminifera *G. bulloides* indicate that local ocean temperatures from the LGM through the deglacial (20 to 15 ka) were ~7°C. Thus at the time of maximum CIS extent when the ice sheet was grounded on the continental shelf (~19.8 ka), temperatures would have been sufficient to induce significant melt at the ice terminus, most likely during the summer. The tidewater margin of the CIS on Vancouver Island can be compared to ocean thermal forcing in similar modern Alaskan tidewater glacier systems. In Leconte Bay, 6-13˚C seawater from the Alaskan Coastal Current (annual surface temperature = 10˚C; Locarnini et al., 2005) interacts with Leconte glacier, a grounded tidewater glacier whose mass is primarily below sea level (Motyka et al., 2003). Ocean temperatures are estimated to be 6˚C at the surface within 200-500 m of the ice terminus, and up to 7.2˚C at depth, similar to our estimated temperatures. This ocean thermal forcing results in high summer season melt rates of ~12 md^{-1} (Motyka et al., 2003).

4.1 CIS conditions at the LGM

The presence of coastal temperatures able to exert <8˚C thermal forcing ~ 2 kyr prior to the onset of retreat requires a reassessment of the stability of the western marine margin of the CIS. Based on our understanding of modern summer Alaskan tidewater systems and the similarity of our reconstructed temperatures to LeConte glacier we assume that ocean thermal forcing drove high melt rates on Juan de Fuca Lobe. How then did the CIS maintain a marine margin and the maximum extent of the CIS lag the LIS? Modern temperate tidewater glaciers that lose volume during thinning, retreat rapidly from their marine margins (Hunter and Powell, 1998; Motyka et al., 2003), yet the CIS maintained a marine margin for nearly 2 ka from ~19 to 17 ka. We argue that there were two important features of the CIS that prevented substantial retreat before 17.2 ka: the presence of morainal shoals (Herzer and Bornhold, 1982) and a significant supply of ice from the Coast Mountains (Margold et al., 2013b).

Ice rafted debris deposition was relatively rare between 19-17 ka. Either calving events were infrequent and/or minor from the time the CIS achieved a marine margin at 19.8 ka (16.7 ^{14}C kyr BP; Clague et al., 1980) until 17.2 ka (Cosma and Hendy, 2008; Blaise et al., 1990) or ocean currents transported the icebergs outside the region. One exception occurs at ~18 ka where >250 μm grains increase to >10 grains g^{-1} following an ~1-2°C warm event that lasted ~500 years.

Bathymetric evidence for the presence of a morainal shoal stabilizing the ice sheet terminus provides a mechanism for reinforcing the western margin of the CIS against iceberg discharge (Hendy and Cosma, 2008; Porter and Swanson, 1998; Blaise et al., 1990; Herzer and Bornhold, 1982). The CIS was primarily a warm-based, temperate ice sheet (Clague and James, 2002) with the ability to move stabilizing sediments to the grounding line relatively rapidly. There is evidence for extensive outwash sediments and infilling of trough scours with unsorted

till in addition to moraine-like banks on the continental shelf (Herzer and Bornhold, 1982). Additionally the extensive Juan de Fuca Lobe transported a significant supply of ice from the Coast Mountains and could have balanced thinning of the western CIS. The Juan de Fuca Lobe was a large reservoir of ice estimated to have covered ~75,700 km^2 with ice up to 2 km thick, and supplied by ice flowing out of the glaciated Coast Mountains which are ~340,000 km^2 (Booth, 1986),

4.2 Timing and magnitude of CIS calving events during the early deglacial (17-15 kyr)

Eventually as northern hemisphere summer insolation increased, the balance between winter precipitation and summer ablation elevated the equilibrium line altitude, and increased subglacial discharge (Clark et al., 2009). An early deglacial shift in the CIS divide was produced by hypothesized ice lost from the grounded continental shelf-based margin of the ice sheet (Margold et al., 2013b). This increase in ice discharge via rapidly thinning outlet glaciers lowered ice-surface profiles on the west side of the Coast Mountains, shifting the ice divide to the east. Recent mapping of glacial meltwater landforms suggests that CIS retreat was an active process, comprised of frontal retreat at the margins and downwasting in central regions land (Margold et al., 2013a; Margold et al., 2013b). Thus CIS retreat on the landlocked western side of the Coastal Mountains requires significant marine ice removal and is consistent with modern studies implicating warm ocean temperatures in large-scale drawdown of land-based ice (Shepherd et al., 2004).

From 17.2 to 16.5 ka *N. pachyderma* temperatures warmed by ~2°C coincident with the first significant deposition of ice rafted debris (IRD) and drop stones at MD02-2496 during the Fraser Glaciation (Figure 2.4B; Cosma and Hendy, 2008; Hendy and Cosma, 2008). During this interval the number of >250 μm grains, g^{-1} increased from a background of <1 to a maximum of

>500 grains, g^{-1} at 16.3 ka, abruptly ending at 16.1 ka. A similar trend was found in the 150-250 μm size fraction. IRD provides direct evidence of CIS retreat by ice calving (Cosma and Hendy, 2008), while physical evidence exists for CIS retreat through the Juan de Fuca Strait between 17.5-16.2 ka (Mosher and Hewitt, 2004). During this interval, glaciomarine sediments at core site PAR85-01 in the Queen Charlotte Island region to the north in Hecate Strait (~400 km NW of MD02-2496; Figure 2.1) also provide evidence for a similar ice calving driven retreat. IRD is identified between 17.7–15.2 ka (15.6-13.6 ^{14}C ka), with a peak in IRD at 17.7 ka (15.6 ^{14}C ka), during which time sedimentation rates rose abruptly and IRD (grains >250 μm) increased from 0 to >95% (percentage of rock and mineral grains >250 μm size fraction) for ~ 1 ka. (Blaise et al., 1990). Thus, from ~17.5 to 15.5 ka retreat via calving is indicated along the tidewater margin of the CIS in western Canada as ocean thermal forcing increased.

As the ice retreated through the narrow Juan de Fuca Strait around 17 ka, and into complex fjords on the Vancouver coast (Mosher and Hewitt, 2004), subglacial discharge would be more narrowly focused and warm seawater increasingly entrained at the edge, resulting in higher rates of submarine melt (Bartholomaus et al., 2013). Moreover, water depth in the strait increases abruptly relative to the continental shelf from ~100 m to >250 m depth. Irreversible retreat can be triggered by the retreat of the ice margin from its morainal shoal into deeper waters like those of the Juan de Fuca and Georgian Straits (Ritchie et al., 2008), at which point the influx of ice is insufficient to counteract melting and iceberg discharge. Modern measurements show that summer upper ocean temperatures (>50 m) in the straits are consistent with those further offshore due to vigorous tidal mixing and likewise, warm seawater was probably mixed into the Straits during the deglacial (Hickey and Banas, 2003).

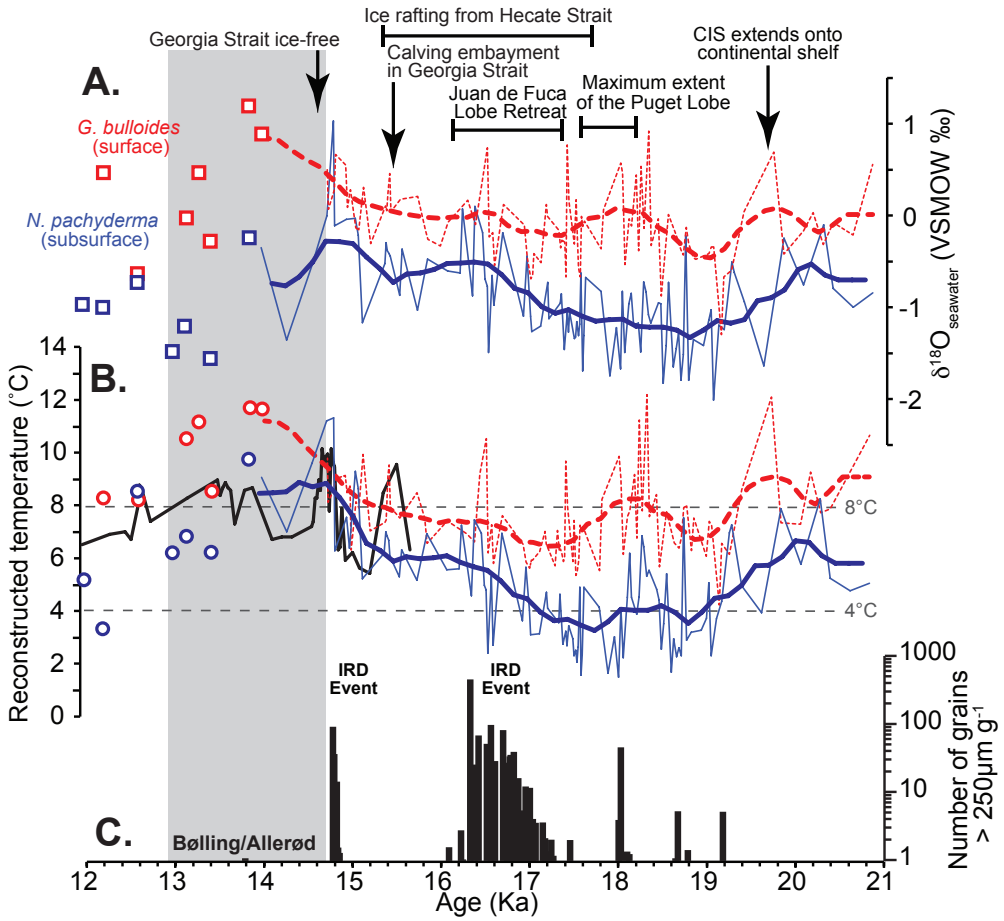

Figure 2.4
Comparison of δ ^{18}O seawater and temperature with IRD recorded at MD02-2496 and local CIS events. (A) Smoothed (thick blue line) and unsmoothed δ $^{18}O_{seawater}$ (‰, Vienna Mean Ocean Water (VSMOW)) for *N. pachyderma* (thin blue line and blue squares), and smoothed (thick red dashed line) and unsmoothed δ $^{18}O_{seawater}$ for *G. bulloides* (thin dotted red line and red squares). (B) Smoothed (thick blue line) and unsmoothed reconstructed ocean subsurface temperatures for *N. pachyderma* (thin blue line and blue circles), and smoothed (thick red dashed line) and unsmoothed *G. bulloides* (thin dotted red line and red circles). Data were smoothed with a 150-year resampling and then a 5-point centered mean. Alkenone-based temperatures from JT96-09 are shown for comparison (thick black line). (C) Ice rafted debris (IRD) measured as the number of grains > 250 µmg^{-1} (black bars), plotted on a logarithmic scale (Cosma and Hendy, 2008). The glacial history of the CIS is annotated on the graph (Clague and James, 2002; Porter and Swanson, 1998; Cosma and Hendy, 2008).

4.3 Timing and magnitude of CIS calving events during the early deglacial (15-13 kyr)

CIS retreat continued on the eastern side of Vancouver Island such that by 15.5 ka (13 ^{14}C ka BP) ice had receded into the deeper Georgian Strait (~400 m water depth) forming a second calving embayment (Clague, 1981; Huntley et al., 2001). A ~3°C temperature increase was recorded at MD02-2496 between 15.5-14 ka indicating further warming into the Bølling

with associated increased ocean thermal forcing on any remaining tidewater glacier systems. A final short IRD event that occurred at MD02-2496 between 14.85-14.79 ka (Hendy and Cosma, 2008) coincident with ocean temperatures of~ 9.5°C recorded by both *G. bulloides* and *N. pachyderma* was likely associated with the Georgia Strait calving embayment. At the same time in the Hecate Strait, IRD-sized rock and mineral grains declined to ~40%, until the ice had retreated from the continental shelf (Blaise et al., 1990). Georgia Strait was ice-free by 14.6 ka (12.5 ^{14}C kyr; Guilbault et al., 2003).

4.4 $\delta^{18}O_{seawater}$ and meltwater from the CIS

Reconstructed $\delta^{18}O_{seawater}$ enables us to further deconvolve deglacial changes in seawater associated with the addition of fresh isotopically depleted glacial meltwater to the relatively saline open ocean water. Meltwater pulses into the Pacific Ocean from the CIS are limited to a few deep sea records. On the Gulf of Alaskan margin Davies et al., (2011) implicate meltwater input as a mechanism for freshening/warming in the surface ocean between 16.65 and 13.8 ka based on depleted $\delta^{18}O_{calcite}$ values of *G. bulloides* and *N. pachyderma* (s.). Additionally an abrupt 1 ‰ decrease in benthic $\delta^{18}O_{calcite}$ at ~14.2 ka provides evidence for the hyperpycnal flow of meltwater at intermediate water depths (~680 m). Large glacial lake outburst floods from proglacial Lake Missoula (Brunner et al., 1999; Lopes and Mix, 2009; Normark and Reid, 2003) provided freshwater that has been identified by the presence of fresh water diatoms in offshore southern Oregon sediments, indicating a freshening of <6 psu in distinct pulses between 31-16 ka (Lopes and Mix, 2009).

No evidence for depleted $d^{18}O_{seawater}$ meltwater pulses can be detected at MD02-2496 as the CIS retreated. Through deglaciation, ocean temperatures and $\delta^{18}O_{seawater}$ are generally in phase, however, enriched $\delta^{18}O_{seawater}$/higher relative salinity was associated with warmer water,

while depleted $\delta^{18}O_{seawater}$/ freshening occurred during cooling of surface waters (Figure 2.3). The most depleted $\delta^{18}O_{seawater}$ values (~-1.5‰) are recorded by *N. pachyderma* (s.) between 19-18 ka. The MD02-2496 benthic $\delta^{18}O_{calcite}$ record located 600 m deeper than the Gulf of Alaska example, displays a gradual shift to enriched isotopic values from the LGM into the Holocene (Cosma et al., 2008), but no abrupt isotopic shifts indicative of hyperpycnal flow.

Several possibilities exist to explain the absence of depleted $\delta^{18}O_{seawater}$ in a region where meltwater from the CIS was entering the Pacific Ocean. As CIS ice accumulated from snow falling at temperate latitudes with a proximal moisture source the isotopic composition of the CIS (-18 to -23‰) may not be sufficiently distinct from that of local seawater. Convection near the terminal ice face could also have reduced $\delta^{18}O_{seawater}$ depletion from melt as fresh, cold subglacial discharge entrained warm, saline ocean water at depth, forcing mixing upward along the terminus (Motyka et al., 2003).

Another possibility relates to how meltwater entered the ocean off western Canada compared to North Atlantic examples. Meltwater indicated by abruptly depleted $\delta^{18}O_{seawater}$, has been detected in the Gulf of Mexico (Williams et al., 2012; Flower et al., 2004) and in association with ice discharge into the Hudson Bay from the LIS (van Kreveld et al., 2000). Drainage of LIS meltwater via the Mississippi River into the Gulf of Mexico was recorded in a small, shallow offshore sedimentary basin that was protected from open ocean currents (Flower et al., 2004). In the northern North Atlantic, there is evidence that the marine margin of the LIS terminated in large ice shelves, where sea ice was commonly present (Petersen et al., 2013). As $\delta^{18}O_{seawater}$ anomalies were often coincident with IRD in the North Atlantic, icebergs calving from the ice shelf may have melted in surface waters, leaving a surface meltwater plume to be

recorded by $\delta^{18}O_{calcite}$ of planktonic foraminifera (Marcott et al., 2011). These environments are not characteristic of the marine CIS margin in Western Canada.

5. Conclusions

While the retreat of the LIS after the LGM (Last Glacial Maximum), corresponded with increasing both northern hemisphere summer insolation at mid- to high latitudes and rising sea level around 19 ka, the CIS growth and retreat lagged (Clark et al., 2009; Carlson and Clark, 2012). Glacial deposits from Tofino on the west coast of Vancouver Island indicate that the ice sheet did not reach the continental shelf until after 19.8 ka (16.7 ^{14}C kyr BP; Clague et al., 1980), and began to retreat from its marine margin at 17.5 ka, leaving the Juan de Fuca Strait ice-free by 16.2 ka (Mosher and Hewitt, 2004).

Reconstructed ocean temperatures in the Northeast Pacific from the LGM through the deglacial (21-12 ka) demonstrate ocean thermal forcing was factor in initial Cordilleran Ice Sheet (CIS) retreat. The glaciomarine sedimentation at MD02-2496, and concomitant changes in Mg/Ca based temperatures and $\delta^{18}O_{seawater}$ suggest possible mechanisms for ice removal and retreat. These results indicate that warm ocean temperatures (4-8°C) throughout deglaciation could have helped to destabilize the marine margin of the CIS. The stepwise ocean warming of ~2°C at 17.2 was associated with significant iceberg calving that began the rapid retreat of the Juan de Fuca Lobe at 17.2 ka. The Bølling was associated with a further ~3°C ocean temperature increase from 15.5 to 14 ka coincident the removal of the ice embayment from Georgia Strait. There is no evidence of a significant (>1 ‰) decrease in $\delta^{18}O_{calcite}$ of planktonic or benthic species, nor in the reconstructed $\delta^{18}O_{seawater}$ record at MD02-2496 in association with meltwater input to the region. We hypothesize that ocean thermal forcing was, through submarine glacial melt processes similar to modern tidewater glacier systems, an important driver of the initial CIS

retreat from its western marine margin. As summer insolation increased through deglaciation, high seasonal subglacial discharge alongside the warm ocean temperatures recorded at MD02-2496 would have produced submarine melting in the tidewater glacier systems of the CIS. These results support evidence for significant, rapid ice removal during early deglaciation that shifted ice divides in the CIS (Margold et al., 2013a; Margold et al., 2013b) and produced rapid isostatic rebound in western Canada (Clague and James, 2002). These results are also consistent with modern studies implicating warm ocean temperatures in increasing ice discharge from ice shelves and the large-scale drawdown of land-based ice (Shepherd et al., 2004; Rignot et al., 2014; Jacobs et al., 2011).

References

Alley, N. F., and S. C. Chatwin (1979), Late Pleistocene history and geomorphology, southwestern Vancouver Island, British Columbia, *Canadian Journal of Earth Sciences*, *16*(9), 1645-1657.

Antonov, J. I., R. A. Locarnini, T. P. Boyer, A. V. Mishonov, and H. E. Garcia (2006), World Ocean Atlas 2005, Volume 2: Salinity. S. Levitus, Ed. NOAA Atlas NESDIS 62, U.S. Government Printing Office, Washington, D.C., 182 pp.

Barker, S., M. Greaves, and H. Elderfield (2003), A study of cleaning procedures used for foraminiferal Mg/Ca paleothermometry, *Geochemistry Geophysics Geosystems*, *4*(9), 8407.

Bartholomaus, T. C., C. F. Larsen, and S. O'Neel (2013), Does calving matter? Evidence for significant submarine melt, *Earth and Planetary Science Letters*, *380*(C), 21-30.

Benn, D. I., C. R. Warren, and R. H. Mottram (2007), Calving processes and the dynamics of calving glaciers, *Earth Science Reviews*, *82*(3-4), 143-179.

Bian, N., and P. A. Martin (2010), Investigating the fidelity of Mg/Ca and other elemental data from reductively cleaned planktonic foraminifera, *Paleoceanography*, *25*(2), PA2215.

Blaise, B., J. J. Clague, and R. W. Mathewes (1990), Time of Maximum Late Wisconsin Glaciation, West Coast of Canada, *Quaternary Research*, *34*, 282-295.

Booth, D. B. (1986), Mass Balance and Sliding Velocity of the Puget Lobe of the Cordilleran Ice Sheet during the Last Glaciation, *Quaternary Research*, *25*, 269-280.

Booth, D. B., K. G. Troost, J. J. Clague, and R. B. Waitt (2004), The Cordilleran Ice Sheet, *The Quaternary period in the United States*, *1*, 17-43.

Boyle, E. A., and L. D. Keigwin (1985), Comparison of Atlantic and Pacific paleochemical records for the last 215,000 years: changes in deep ocean circulation and chemical inventories, *Earth and Planetary Science Letters*, *76*, 135-150.

Brunner, C. A., W. R. Normark, S. F, and G. G. Zuffa (1999), Deep-sea sedimentary record of the late Wisconsin cataclysmic floods from the Columbia River, *Geology*, *27*(5), 463-466.

Bush, A. B. G., and S. G. H. Philander (1999), The climate of the Last Glacial Maximum: Results from a coupled atmosphere-ocean general circulation model, *Journal of Geophysical Research*, *104*(D20), 24509-24525.

Carlson, A. E., and P. U. Clark (2012), Ice sheet sources of sea level rise and freshwater discharge during the last deglaciation, *Reviews of Geophysics*, *50*, RG4007.

Chappell, J., and N. J. Shackleton (1986), Oxygen isotopes and sea level, *Nature*, *324*, 137-140.

Clague, J. J., J. E. Armstrong, and W. H. Matthews (1980), Advance of the Late Wisconsin Cordilleran Ice Sheet in Southern British Columbia Since 22,000 Yr B.P., *Quaternary Research*, *13*, 322-326.

Clague, J.J. (1981), Late Quaternary geology and geochronology of British Columbia, Part 2, *Geological Survey of Canada, 80*, 41pp.

Clague, J. J., and T. S. James (2002), History and isostatic effects of the last ice sheet in southern British Columbia, *Quaternary Science Reviews*, *21*, 71-87.

Clark, P. U., A. S. Dyke, J. D. Shakun, A. E. Carlson, J. Clark, B. Wohlfarth, J. X. Mitrovica, S. W. Hostetler, and A. M. McCabe (2009), The Last Glacial Maximum, *Science*, *325*, 710-714.

COHMAP Members (1988), Climatic Changes of the Last 18,000 Years: Observations and Model Simulations, *Science*, *241*(4869), 1043-1052.

Cosma, T., and I. L. Hendy (2008), Pleistocene glacimarine sedimentation on the continental slope off Vancouver Island, British Columbia, *Marine Geology*, *255*, 45-54.

Cosma, T. N., I. L. Hendy, and A. S. Chang (2008), Chronological constraints on Cordilleran Ice Sheet glaciomarine sedimentation from core MD02-2496 off Vancouver Island (western Canada), *Quaternary Science Reviews*, *27*(9-10), 941-955.

Craig, H. (1965), The measurement of oxygen isotope paleotemperatures, *Spoleto Conference on Stable Isotopes in Oceanographic Studies and Paleotemperature*, 161-182.

Crawford, W., J. Galbraith, and N. Bolingbroke (2007), Line P ocean temperature and salinity, 1956–2005, *Progress In Oceanography*, *75*(2), 161-178.

Cummins, P. F., and H. J. Freeland (2007), Variability of the North Pacific Current and its bifurcation, *Progress In Oceanography*, *75*(2), 253-265.

Cummins, P. F., and D. Masson (2014), Climatic variability and trends in the surface waters of coastal British Columbia, *Progress In Oceanography*, *120*(C), 279-290.

Davies, M. H., A. C. Mix, J. S. Stoner, J. A. Addison, J. Jaeger, B. Finney, and J. Wiest (2011), The deglacial transition on the southeastern Alaska Margin: Meltwater input, sea level rise, marine productivity, and sedimentary anoxia, *Paleoceanography*, *26*(2), PA2223.

Elderfield, H., and G. Gannsen (2000), Past temperature and $\delta^{18}O$ of surface ocean waters inferred from foraminiferal Mg/Ca ratios, *Nature*, *405*, 442-445.

Ferguson, J. E., G. M. Henderson, M. Kucera, and R. E. M. Rickaby (2008), Systematic change of foraminiferal Mg/Ca ratios across a strong salinity gradient, *Earth and Planetary Science Letters*, *265*(1-2), 153-166.

Flower, B. P., D. W. Hastings, H. W. Hill, and T. M. Quinn (2004), Phasing of deglacial warming and Laurentide Ice Sheet meltwater in the Gulf of Mexico, *Geology*, *32*(7), 597.

Friedrich, O., R. Schiebel, P. A. Wilson, S. Weldeab, C. J. Beer, M. J. Cooper, and J. Fiebig (2012), Influence of test size, water depth, and ecology on Mg/Ca, Sr/Ca, $\delta^{18}O$ and $\delta^{13}C$ in nine modern species of planktic foraminifers, *Earth and Planetary Science Letters*, *319-320*, 133-145.

Guilbault, J. P., J.V. Barrie, K. Conway, M. Lapointe, M., and T. Radi (2003), Paleoenvironments of the Strait of Georgia, British Columbia during the last deglaciation: microfaunal and microfloral evidence, *Quaternary Science Reviews, 22*, 839-857.

Hendy, I. L., and T. Cosma (2008), Vulnerability of the Cordilleran Ice Sheet to iceberg calving during late Quaternary rapid climate change events, *Paleoceanography*, *23*(2), PA2101.

Herzer, R. H., and B. D. Bornhold (1982), Glaciation and post-glacial history of the continental shelf off southwestern Vancouver Island, British Columbia, *Marine Geology*, *48*, 285-319.

Hickey, B. M., and N. S. Banas (2008), Why is the northern end of the California Current system so productive?, *Oceanography*, *21*(4), 90-107.

Howat, I. M., I. Joughin, and T. A. Scambos (2007), Rapid changes in ice discharge from Greenland outlet glaciers, *Science*, *315*(5818), 1559-1561.

Hunter, L. E., and R. D. Powell (1998), Ice foot development at temperate tidewater margins in Alaska, *Geophysical Research Letters*, *25*(11), 1923-1926.

Huntley, D., J. J. Clague, and P. T. Bobrowsky (2001), Ocean Drilling Program Leg 169S: surficial geology, stratigraphy and geomorphology of the Saanich Inlet area, southeastern Vancouver Island, British Columbia, *Marine Geology*, *174*, 27-41.

Jacobs, S. S., A. Jenkins, C. F. Giulivi, and P. Dutrieux (2011), Stronger ocean circulation and increased melting under Pine Island Glacier ice shelf, *Nature Geoscience*, *4*(8), 519-523.

James, T., E. J. Gowan, I. Hutchinson, C. J. J, J. V. Barrie, and K. W. Conway (2009), Sea-level change and paleogeographic reconstructions, southern Vancouver Island, British Columbia, Canada, *Quaternary Science Reviews*, *28*(13-14), 1200-1216.

Jenkins, A. (2011), Convection-driven melting near the grounding lines of ice shelves and tidewater glaciers, *Journal of Physical Oceanography*, *41*, 2279-2294.

Jonkers, L., P. Jiménez-Amat, P. G. Mortyn, and G.-J. A. Brummer (2013), Seasonal Mg/Ca variability of *N. pachyderma* (s) and *G. bulloides*: Implications for seawater temperature reconstruction, *Earth and Planetary Science Letters*, *376*(C), 137-144.

Joughin, I., R. B. Alley, and D. M. Holland (2012), Ice-sheet response to oceanic forcing, *Science*, *338*(6111), 1172-1176.

Keigwin, L. D., and E. A. Boyle (1989), Late Quaternary paleochemistry of high-latitude surface waters, *Palaeogeography, Palaeoclimatology, Palaeoecology*(73), 85-106.

Kienast, S. S., and J. L. McKay (2001), Sea surface temperatures in the subarctic Northeast Pacific reflect millennial-scale climate oscillations during the last 16 kyrs, *Geophysical Research Letters*, *28*(8), 1563-1566.

Kim, S.-T., and J. R. O'Neil (1997), Equilibrium and nonequilibrium oxygen isotope effects in synthetic carbonates, *Geochimica et Cosmochimica Acta*, *61*(16), 3461-3475.

Kozdon, R., A. Eisenhauer, M. Weinelt, M. Y. Meland, and D. Nurnberg (2009), Reassessing Mg/Ca temperature calibrations of *Neogloboquadrina pachyderma* (sinistral) using paired $\delta^{44}/^{40}$Ca and Mg/Ca measurements, *Geochemistry Geophysics Geosystems*, *10*(3), Q03005.

Kuroyanagi, A., and H. Kawahata (2004), Vertical distribution of living planktonic foraminifera in the seas around Japan, *Marine Micropaleontology*, *53*(1-2), 173-196.

Locarnini, R. A., A. V. Mishonov, J. I. Antonov, T. P. Boyer, and H. E. Garcia (2006), World Ocean Atlas 2005, Volume 1: Temperature. S. Levitus, Ed. NOAA Atlas NESDIS 61, U.S. Government Printing Office, Washington, D.C., 182 pp.

Lopes, C., and A. C. Mix (2009), Pleistocene megafloods in the northeast Pacific, *Geology*, *37*(1), 79-82.

MacFadyen, A., B. M. Hickey, and W. P. Cochlan (2008), Influences of the Juan de Fuca Eddy on circulation, nutrients, and phytoplankton production in the northern California Current System, *Journal of Geophysical Research*, *113*(C8), C08008.

Mangerud, J., S. T. Andersen, B. E. Berglund, J. J. Donner (1974), Quaternary stratigraphy of norden, a proposal for terminology and classification, *Boreas 3*, 109–126.

Marchitto, T. M., W. B. Curry, J. Lynch-Stieglitz, S. P. Bryan, K. M. Cobb, and D. C. Lund (2014), Improved oxygen isotope temperature calibrations for cosmopolitan benthic foraminifera, *Geochimica et Cosmochimica Acta*, *130*(C), 1-11.

Marcott, S. A., et al. (2011), Ice-shelf collapse from subsurface warming as a trigger for Heinrich events-supporting info, *Proceedings of the National Academy of Sciences*, *108*(33), 13415-13419.

Margold, M., K. N. Jansson, J. Kleman, and A. P. Stroeven (2013)a, Lateglacial ice dynamics of the Cordilleran Ice Sheet in northern British Columbia and southern Yukon Territory: retreat pattern of the Liard Lobe reconstructed from the glacial landform record, *Journal of Quaternary Science*, *28*(2), 180-188.

Margold, M., K. N. Jansson, J. Kleman, A. P. Stroeven, and C. J. J (2013)b, Retreat pattern of the Cordilleran Ice Sheet in central British Columbia at the end of the last glaciation reconstructed from glacial meltwater landforms, *Boreas*, *42,* 830-847.

Martin, P. A., and D. W. Lea (2002), A simple evaluation of cleaning procedures on fossil benthic
foraminiferal Mg/Ca, *Geochemistry Geophysics Geosystems*, *3*(10), 8401.

Martínez-Botí, M. A., P. G. Mortyn, D. N. Schmidt, D. Vance, and D. B. Field (2011), Mg/Ca in foraminifera from plankton tows: Evaluation of proxy controls and comparison with core tops, *Earth and Planetary Science Letters*, *307*, 113-125.

Mashiotta, T. A., D. W. Lea, and H. J. Spero (1999), Glacial–interglacial changes in subantarctic sea surface temperature and δ^{18}O-water using foraminiferal Mg, *Earth and Planetary Science Letters*, *170*, 417-432.

Masson, D., and P. F. Cummins (1999), Numerical simulations of a buoyancy-driven coastal countercurrent off Vancouver Island, *Journal of Physical Oceanography*, *29*, 418-435.

Masson, D., and I. Fine (2012), Modeling seasonal to interannual ocean variability of coastal British Columbia, *Journal of Geophysical Research*, *117*(C10), C10019.

Meier, M. F., and A. Post (1987), Fast tidewater glaciers, *Journal of Geophysical Research*, *92*(B9), 9051-9058.

Mosher, D. C., and A. T. Hewitt (2004), Late Quaternary deglaciation and sea-level history of eastern Juan de Fuca Strait, Cascadia, *Quaternary International*, *121*, 23-39.

Motyka, R. J., L. Hunter, K. A. Echelmeyer, and C. Connor (2003), Submarine melting at the terminus of a temperate tidewater glacier, LeConte Glacier, Alaska, U.S.A., *Annals of Glaciology*, *36*, 57-65.

Nagashima, K., R. Tada, H. Matsui, T. Irino, A. Tani, and S. Toyoda (2007), Orbital- and millennial-scale variations in Asian dust transport path to the Japan Sea, *Palaeogeography, Palaeoclimatology, Palaeoecology*, *247*(1-2), 144-161.

Normark, W. R., and J. A. Reid (2003), Extensive deposits on the Pacific plate from late Pleistocene North American glacial lake outbursts, *The Journal of Geology*, *111*, 617-637.

Nürnberg, D. (1995), Magnesium in tests of *Neogloboquadrina pachyderma sinistral* from high northern and southern latitudes, *Journal of Foraminiferal Research*, *25*(4), 350-368.

O'Leary, M., and P. Christoffersen (2013), Calving on tidewater glaciers amplified by submarine frontal melting, *The Cryosphere*, *7*, 119-128.

Pak, D. K., D. W. Lea, and J. P. Kennett (2004), Seasonal and interannual variation in Santa Barbara Basin water temperatures observed in sediment trap foraminiferal Mg/Ca, *Geochemistry Geophysics Geosystems*, *5*(12), Q12008.

Patton, G. M., P. A. Martin, A. Voelker, and E. Salgueiro (2011), Multiproxy comparison of oceanographic temperature during Heinrich Events in the eastern subtropical Atlantic, *Earth and Planetary Science Letters*, *310*, 45-58.

Peña, L. D., S. L. Goldstein, S. R. Hemming, K. M. Jones, E. Calvo, C. Pelejero, and I. Cacho (2013), Rapid changes in meridional advection of Southern Ocean intermediate waters to the tropical Pacific during the last 30kyr, *Earth and Planetary Science Letters*, *368*(C), 20-32.

Petersen, S. V., D. P. Schrag, and P. U. Clark (2013), A new mechanism for Dansgaard-Oeschger cycles, *Paleoceanography*, *28*, 1-7.

Porter, P. C., and T. W. Swanson (1998), Radiocarbon Age Constraints on Rates of Advance and Retreat of the Puget Lobe of the Cordilleran Ice Sheet during the Last Glaciation, *Quaternary Research*, *50*, 205-213.

Reimer, P. J., et al. (2013), INTCAL13 and MARINE13 radiocarbon age calibration curves 0-50,000 years cal BP, *Radiocarbon*, *55*(4), 1869-1887.

Reynolds, L., and R. C. Thunell (1985), Seasonal succession of planktonic foraminifera in the subpolar North Pacific, *Journal of Foraminiferal Research*, *15*(4), 282-301.

Rignot, E., I. Fenty, D. Menemenlis, and Y. Xu (2012), Spreading of warm ocean waters around Greenland as a possible cause for glacier acceleration, *Annals of Glaciology*, *53*(60), 257-266.

Rignot, E., M. Koppes, and I. Velicogna (2010), Rapid submarine melting of the calving faces of West Greenland glaciers, *Nature Geoscience*, *3*, 187-191.

Rignot, E., J. Mouginot, M. Morlighem, H. Seroussi, and B. Scheuchl (2014), Widespread, rapid grounding line retreat of Pine Island, Thwaites, Smith, and Kohler glaciers, West Antarctica, from 1992 to 2011, *Geophysical Research Letters*, *41*, 3502-3509.

Ritchie, J. B., C. S. Lingle, R. J. Motyka, and M. Truffer (2008), Seasonal fluctuations in the advance of a tidewater glacier and potential causes: Hubbard Glacier, Alaska, USA, *Journal of Glaciology*, *54*(186), 401-411.

Robinson, S.W., and G. Thompson (1981), Radiocarbon corrections for marine shell dates with application to southern Pacific Northwest coast prehistory. *Syesis 14,* 45-57.

Sautter, L. R., and R. C. Thunell (1989)a, Seasonal succession of planktonic foraminifera: Results from a four-year time-series sediment trap experiment in the Northeast Pacific, *Journal of Foraminiferal Research, 19*, 253–267.

Sautter, L. R., and R. C. Thunell (1989)b, Foraminifera and Chlorophyll Maximum: Vertical Distribution, Seasonal Succession, and Paleoceanographic Significance, *Journal of Foraminiferal Research*, *19*, 253-267.

Schmidt, D. N., T. Elliott, and S. A. Kasemann (2008), The influences of growth rates on planktic foraminifers as proxies for palaeostudies - a review, *Geological Society, London, Special Publications*, *303*, 73-85.

Schmidt, D. N., S. Renaud, J. Bollmann, R. Schiebel, and H. R. Thierstein (2004), Size distribution of Holocene planktic foraminifer assemblages: biogeography, ecology and adaptation, *Marine Micropaleontology*, *50*, 319-338.

Schrag, D. P., G. Hampt, and D. W. Murray (1996), Pore fluid constraints on the temperature and oxygen isotopic composition of the glacial ocean, *Science*, *272*(5270), 1930-1932.

Seale, A., P. Christoffersen, R. I. Mugford, and M. O'Leary (2011), Ocean forcing of the Greenland Ice Sheet: Calving fronts and patterns of retreat identified by automatic satellite monitoring of eastern outlet glaciers, *Journal of Geophysical Research*, *116*.

Seguinot, J., C. Khroulev, I. Rogozhina, A. P. Stroeven, and Q. Zhang (2013), The effect of climate forcing on numerical simulations of the Cordilleran ice sheet at the Last Glacial Maximum, *The Cryosphere Discussions*, *7*(6), 6171-6212.

Shackleton, N. J. (1974), Attainment of isotopic equilibrium between ocean water and the benthonic foraminifera genus, *Colloques Internationaux du C.N.R.S.*, *219*, 203-209.

Shepherd, A. (2004), Warm ocean is eroding West Antarctic Ice Sheet, *Geophysical Research Letters*, *31*(23), L23402.

Straneo, F., G. S. Hamilton, D. A. Sutherland, L. A. Stearns, F. Davidson, M. O. Hammill, G. B. Stenson, and A. Rosing-Asvid (2010), Rapid circulation of warm subtropical waters in a major glacial fjord in East Greenland, *Nature Geoscience*, *3*, 182-186.

Strub, P. T., and C. James (2002), Altimeter-derived surface circulation in the large–scale NE Pacific Gyres. Part 1. Seasonal variability, *Progress In Oceanography*, *53*, 163-183.

Stumpf, A. J., B. E. Broster, and V. M. Levson (2000), Multiphase flow of the late Wisconsinan Cordilleran ice sheet in western Canada, *Geological Society of America Bulletin*, *112*(12),

1850-1863.

Thomson, R. E., and I. V. Fine (2003), Estimating mixed layer depth from oceanic profile data, *Journal of Atmospheric and Oceanic Technology*, 1-11.

van Kreveld, S., M. Sarnthein, H. Erlenkeuser, P. M. Grootes, S. Jung, M. J. Nadeau, U. Pfaumann, and A. Voelker (2000), Potential links between surging ice sheets, circulation changes, and the Dansgaard-Oeschger cycles in the Irminger Sea, 60-18 kyr, *Paleoceanography*, *15*(4), 425-442.

von Langen, P. J. (2005), Effects of temperature on Mg/Ca in neogloboquadrinid shells determined by live culturing, *Geochemistry Geophysics Geosystems*, *6*(10), Q10P03.

Waelbroeck, C., L. Labeyrie, E. Michel, J.-C. Duplessy, J. F. McManus, K. Lambeck, E. Balbon, and M. Labracherie (2002), Sea-level and deep water temperature changes derived from benthic foraminifera isotopic records, *Quaternary Science Reviews*, *21*, 295-305.

Williams, C., B. P. Flower, and D. W. Hastings (2012), Seasonal Laurentide Ice Sheet melting during the "Mystery Interval" (17.5-14.5 ka), *Geology*, *40*(10), 955-958.

Xu, Y., E. Rignot, D. Menemenlis, and M. Koppes (2012), Numerical experiments on subaqueous melting of Greenland tidewater glaciers in response to ocean warming and enhanced subglacial discharge, *Annals of Glaciology*, *53*(60), 229-234.

Chapter 3

The California Current System as a transmitter of millennial scale climate change on the northeastern Pacific margin from 10-50 ka

Abstract

A high resolution record of $\delta^{18}O$ and Mg/Ca-based temperatures spanning 10-50 ka has been reconstructed from the Vancouver margin of the northeastern Pacific Ocean (MD02-2496) from two planktonic foraminiferal species, *Neogloboquadrina pachyderma* (s.) and *Globigerina bulloides*. While $\delta^{18}O_{calcite}$ is synchronous with Dansgaard-Oeschger Interstadials (DOIs) throughout the record, sea surface temperatures (SSTs) and reconstructed $\delta^{18}O_{seawater}$ are out of phase with Greenland climate after 30 ka as the Cordilleran and Laurentide Ice Sheet reached their maximum extent. Prior to 30 ka, through the warmest interval of Marine Isotope Stage 3 (MIS 3), changes in water mass characteristics such as $\delta^{18}O_{seawater}$ and enriched $\delta^{15}N$ events apparently responded to millennial-scale climate change, such that warmer SSTs and higher $\delta^{18}O_{seawater}$ coincided with heavier $\delta^{15}N$ values associated with DOIs.

These water mass characteristic shifts are suggestive of the presence of surface water advected from the Eastern Tropical North Pacific (ETNP) by relative strengthening of the California Undercurrent (CUC) bringing warm, salty tropical waters poleward during DOIs. The linkage between the strength of the CUC on the NE Pacific margin and DOIs may be related to increased sea surface heights off Central America as the Intertropical Convergence Zone (ITCZ) shifted northward in response to changes in North Atlantic Ocean circulation. However, this

linkage appears to weaken from 30 ka through deglaciation. This could result from either a significant local climate overprint from the expanding Cordilleran Ice Sheet (CIS), and/or the increasing topographic height of the Laurentide Ice Sheet (LIS) that influenced atmospheric circulation over western North America.

1. Introduction

Reconstructions of oceanographic conditions on the northeastern Pacific margin during the last glacial interval have displayed a high coherence with abrupt millennial scale climate events recorded in the North Atlantic deep sea and Greenland ice cores (Behl and Kennett, 1996; Cannariato and Kennett, 1999; Hendy and Kennett, 2000; Seki et al., 2002; Hendy et al., 2004; Hendy and Pedersen, 2005; Chang et al., 2008; Hendy and Cosma, 2008; Hendy, 2010; Pak et al., 2012; Ohkushi et al., 2014) despite their position distal to the LIS and regional North Atlantic climate forcing. Floral and faunal temperature proxies from ocean sediment cores at Santa Barbara Basin (Behl and Kennett, 1996; Hendy and Kennett, 2000), Point Conception (Seki et al., 2002; Hendy, 2010; Pak et al., 2012), Northern California (Mix et al., 1999), and Vancouver Island (Chang et al., 2008; Hendy and Cosma, 2008) display shifts suggesting warming during DOIs and cooling during stadials. Furthermore, changes in northeastern Pacific subsurface water mass characteristics (eg: warm and relatively salty waters during DOIs, cold and relatively fresh waters during stadials) and upwelling related productivity are also coherent with DOI events (Cannariato and Kennett, 1999; Hendy et al., 2004; Hendy and Pedersen, 2005; Chang et al., 2008; Chang et al., 2014; Ohkushi et al., 2014).

The mechanism responsible for SST/isotopic shifts in the extratropical North Pacific in response to DOI warming is not well understood, although the rapidity of the North Pacific oceanic response to the abrupt DOI climate events implicates atmospheric reorganization over

the Pacific Ocean (Hendy and Kennett, 2000; Hendy et al., 2002). An atmospheric response can be linked to North Atlantic climate change via shifts in the ITCZ (Leduc et al., 2009; Okumura et al., 2009). Model simulations and proxy reconstructions indicate that cooling in the North Atlantic leads to a southward shift in the ITCZ, resulting in reduced precipitation in the North Pacific, while abrupt warming is associated with a northward movement of the ITCZ (Zhang and Delworth, 2005; Leduc et al., 2009; Denton et al., 2010; Deplazes et al., 2013). Other Atlantic to Pacific Ocean basinal connections could be the result of anomalously cool westerly winds during North Atlantic stadials causing larger surface heat fluxes and southward Ekman transport in the central Pacific (Okumura et al., 2009), and/or relative changes in the strength of pressure systems such as the Arctic Low (Manabe and Stouffer, 1988).

Planktonic foraminiferal faunal and $\delta^{18}O_{calcite}$ shifts during DOI climate events suggest that the northeastern Pacific Ocean surface waters responded to rapid climate change with a simple temperature response (Hendy et al., 2002). However, recent Mg/Ca-based SST reconstructions from planktonic foraminifera off California at ODP Site 1017, revealed warming of 3˚ to 7˚C during DOI events that was also associated with higher $\delta^{18}O_{seawater}$ (Pak et al., 2012), suggesting that incursions of relatively warm and saline waters during interstadial warming in the North Atlantic could be ascribed to changes in the relative strength of the California Current System (CCS). Thus interstadials were associated with warm, high $\delta^{18}O_{seawater}$ water due to an increased contribution of saline, tropically sourced CUC water, while stadials were associated with increased contribution of fresh, subpolar water in the California Current System (CCS) (Pak et al., 2012).

Paired proxies to measure temperature and $\delta^{18}O_{seawater}$ in paleoceanographic studies provide a powerful tool for reconstructing ocean circulation response to rapid climate change.

The temperature-salinity characteristics of surface waters have been used as a conservative tracer to assess the modern ratio of ETNP to North Pacific water masses within the coastal current along North America with increasing temperature and salinity referred to as "spiciness" (Flament, 2002; Meinvielle and Johnson, 2013). Presently relatively warm, saline or spicy CUC water is detectable as far north as the Gulf of Alaska (Thomson and Krassovski, 2010), and is estimated to comprise up to ~20-40% of the upper water column offshore of Vancouver Island (Meinvielle and Johnson, 2013). Additionally the $\delta^{15}N$ composition and oxygen concentration of ETNP oxygen minimum zone waters influence water mass characteristics along the coast of North America. In the modern ocean, low oxygen, denitrified water enriched in $\delta^{15}N$ moves northward from the ETNP via the CUC (Liu and Kaplan, 1989), and is associated with salinity maxima.

Here we investigate abrupt climate changes in the northern Northeast Pacific using the deep-sea core MD02-2496 (48°58'47"N, 127°02'14"W; 38.38 m core length; 1243 m water depth) retrieved from the continental slope, offshore from Vancouver Island, Canada. This sediment core represents the northernmost core site within the CCS yet studied, spanning the last 50 ka. High resolution planktonic foraminiferal $\delta^{18}O_{calcite}$ (This study; Cosma et al., 2008) and Mg/Ca based ocean temperature records were generated from the surface dwelling *Globigerina bulloides* and thermocline dwelling *Neogloboquadrina pachyderma* (sinistral). $\delta^{18}O_{seawater}$ records for the two foraminiferal species have been generated using the coeval $\delta^{18}O_{calcite}$ and Mg/Ca-based ocean temperature records in order to reconstruct SST and salinity changes connected with poleward undercurrent flow during the last glacial in association with millennial scale climate variability.

1.1 Core site and modern setting

The MD02-2496 core site lies within the transition zone between subtropical and subpolar gyral circulation, and is sensitive to changes in gyral strength and wind forcing, which may affect ocean temperatures by increased advection of surface waters or changes in upwelling regime (Freeland, 2006; Cummins and Freeland, 2007). The North Pacific Current (NPC) forms the northern branch of the North Pacific gyre, advecting colder, fresher surface waters from the western to the eastern North Pacific (Figure 3.1). The NPC bifurcates near the northeastern Pacific coast at ~50˚N latitude to form the Alaskan Coastal Current to the north and California Current to the south (Chelton and Davis, 1982). On the eastern boundary of the North Pacific Ocean, locally driven changes in ocean surface temperature and salinity are thought to be regulated primarily by the strengthening and weakening of the CCS, which makes up the eastern branch of the North Pacific gyre (Lynn and Simpson, 1987), and is driven by the strength and position of the NPH. The relative strength of the CCS/CUC is among the most important factors controlling variability in surface water characteristics along the Pacific margin. Wind field strength affects the amount of NPC entering the CCS from the north as well as the return flow of the CUC (Strub and James, 2002; Douglass et al., 2006; Freeland, 2006).

While the mechanisms for generating enhanced CUC flow are not fully understood, sea surface height at the southern CCS boundary is known to be important (Connolly et al., 2014). In the modern climate system, the development of increased sea surface heights off Central America due to northward shifts in the ITCZ or Walker circulation result in enhanced poleward flow of surface waters in the northeastern Pacific originating in the tropics (Strub and James, 2002). Upwelling/wind stress along the California coast also strengthens the CUC significantly in the northern CCS, where increased upwelling at ~40˚N creates a steeper density gradient to the north, enhancing poleward undercurrent flow (Connolly et al., 2014). The North Pacific High

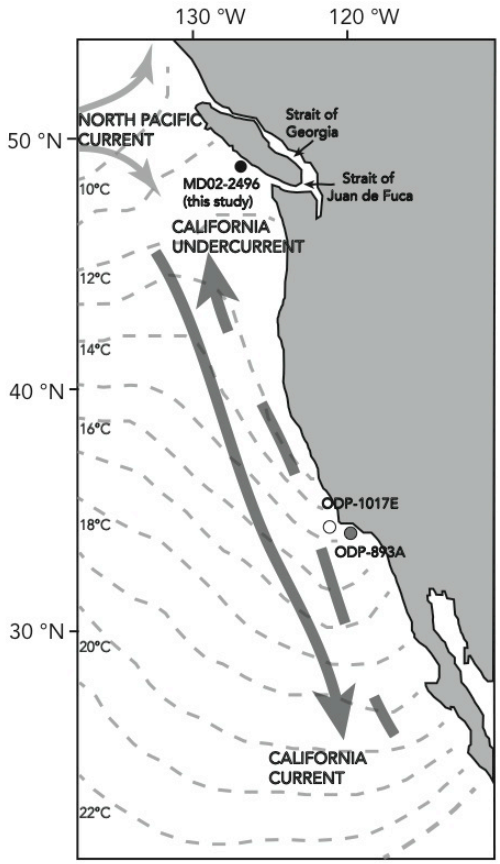

Figure 3.1
Location of core sites (black circle, this study) MD02-2496 (48°58'48"N, 127°02'14"W, 1243 m water depth), (white circle) ODP-1017E (34°32'N, 121°06'W, 966 m water depth) (Pak et al., 2012; Hendy, 2010), and (grey circle) ODP-893A (Hendy and Kennett, 2000) (34°17'15"N, 120°02'12"W, 576.5 m water depth) along the northeastern Pacific margin. Dashed lines indicate annual average SSTs (Auad et al., 2011). Arrows represent dominant modern current configurations, where the light grey arrows represent the North Pacific Current. The California Current (dark grey arrow) extends from the continental slope to ~1000 km offshore. The northward pointing dark grey arrow represents the core flow of the California Undercurrent, along the shelf break and at 200-300 m depth and upwelled onto the shelf.

(NPH) is thought to have strengthened and moved northward during DOIs, commensurate with more upwelling favorable winds (Hendy et al., 2004) and strengthened flow of the CUC (Hendy and Kennett, 2003). Thus multiple mechanisms exist that could drive the poleward flow of tropical surface waters in the northeastern Pacific during DOI climate events.

The modern annual average salinity at the site is 32.5 PSU, and average surface ocean temperature is ~12°C, ranging from 8°C in winter to 14°C in summer (Antonov et al., 2005; Locarnini et al., 2005). The summer season longshore coastal current system is composed of the California Current, the CUC, and the Vancouver Island Coastal Current (Masson and Fine,

2012). The central flow of the California Current is several hundred kilometers offshore, while the core of the poleward CUC flows over the continental slope, upwelling onto the shelf (Strub and James, 2002). Seasonal upwelling occurs after the spring transition when wind forcing changes direction from southerly in winter to northerly dominance in summer around June-July (Hickey and Banas, 2008). Modern nearshore currents on the continental shelf are driven by buoyancy forcing due to freshwater input from the Fraser River into the Georgia and Juan de Fuca Straits (Masson and Cummins, 1999). Fresh waters are tidally mixed with ocean currents entering the Straits, and this relatively buoyant water flows northward out of the Straits over the continental shelf, forming the Vancouver Island Coastal Current system (Cummins and Masson, 2014).

2. Methods

2.1 Core Chronology

Samples were analyzed at 5-10 cm intervals from 695 (uncorrected) to 3835 cm below core top in MD02-2496. Resolution of the 5 cm intervals ranges from ~15 to 160 years as a result of changing sedimentation rate within the core; the sedimentation rate is highest during the deglacial (15-20 ka).

Core chronology was established by Cosma et al., (2008), and is based upon forty-seven mixed planktonic foraminiferal and bulk organic carbon radiocarbon dates. The original chronology has been modified using the MARINE13 calibration (Reimer et al., 2013) generating a new calendar year based chronology (Taylor et al., 2014). Age model errors were estimated using a Bayesian model, Bacon 2.2 (Blaauw and Christen, 2011) and range from ± ~0.2 to 2 ka. A constant regional reservoir correction (ΔR) of 402.7 ±50 years was assumed (Robinson and

Thompson, 1981). Greenland climate events date assignments were made according to Blockley et al. (2012).

2.2 Stable isotope and Mg/Ca analysis

Oxygen isotope analyses were performed on the surface dwelling foraminifera *G. bulloides*. Samples consisting of planktonic foraminiferal species *G. bulloides* were picked from the >125 μm fraction, and 190 *G. bulloides* samples were prepared using standard techniques for stable isotope analysis. Samples were baked at 200°C under vacuum for 1 hour and dissolved at 76°C with anhydrous phosphoric acid in a Finnigan MAT Kiel device for analysis in a Finnigan MAT 251 triple collector isotope ratio mass spectrometer at the University of Michigan Stable Isotope Laboratory. Machine precision was <0.1 ‰ and replicate $\delta^{18}O$ values yielded a mean standard deviation of 0.14 ‰ for *G. bulloides*. Samples are reported using standard δ notion relative to the Vienna Pee Dee Belemnite (VPDB) standard.

Samples were analyzed for major and trace metals (Ca, Mg, Sr, Fe, Mn). Approximately 60 individual *N. pachyderma* (s.) and 25 *G. bulloides* were picked to achieve an average sample weight of ~300 μg for each analysis. Poor carbonate preservation in the organic carbon-rich Holocene prevented Mg/Ca analysis for samples younger than~10 ka. Visual inspection prior to analysis confirmed that foraminifera were well preserved prior to the Holocene. Samples were weighed and crushed before undergoing cleaning of contaminant phases via a multi-step protocol involving clay removal, and oxidative and reductive steps (Martin and Lea, 2002). In this marginal environment, reductive cleaning is necessary to remove oxides potentially adsorbed after sedimentation. Although the reductive cleaning step can lead to sample loss due to dissolution, a cleaning study of *N. dutertrei*, which has a similar shell ultrastructure to *N. pachyderma*, indicated that reductive cleaning results in little lattice bound Mg loss (Bian and

Martin, 2010). Cleaned samples were analyzed for trace metals using a Thermo-Finnigan Element II high resolution ICP-MS at the University of Michigan (Barker et al., 2003; Boyle and Keigwin, 1985; Keigwin and Boyle, 1989). The analytical precision of Mg/Ca based on 43 replicate analyses of external consistency standards is 0.074 mmol/mol (1 σ). The analytical precision for Mg/Ca splits (6 pairs), reflecting both analytical and sample-processing uncertainty is 0.16 mmol/mol (1 σ), corresponding to 1.5˚C uncertainty. 22% of samples were rejected due to low sample recovery (<10%), or high Mn/Ca and Fe/Ca ratios suggestive of sample contamination.

G. bulloides and *N. pachyderma* Mg/Ca values were converted to temperatures using the Elderfield and Ganssen (2000) calibration equation derived from core-top samples over a latitudinal transect from 30˚ to 60˚ N. This calibration equation is based on multiple temperate and subpolar species (Mean annual temperature 8˚-22˚C) including both *G. bulloides* and *N. pachyderma* (s.):

$$Mg/Ca = 0.52 * e^{(0.10*Temperature)} \quad (\pm 0.7°C \text{ standard error}) \quad (1)$$

While the error based on Mg/Ca analysis is well constrained, the error associated with the pre-exponential and exponential constants in the Mg/Ca-temperature calibration are not. Propagation of this error would overwhelm any real variability in the temperature record. We therefore confine our error estimates to variance in the raw Mg/Ca values, and while we assign absolute temperatures to these values, we emphasize here that we are most confident in the relative magnitude of changes rather than definitive temperature reconstructions.

Mg/Ca-based temperature reconstructions and the $\delta^{18}O_{calcite}$ of coeval samples were used to calculate changes in $\delta^{18}O_{seawater}$ at MD02-2496. For this, we used the calibration for $\delta^{18}O$ of foraminiferal calcite and temperature detailed by Shackleton (1974):

$$T\ (°C) = 16.9 - 4.38\ (\delta^{18}O_{calcite} - \delta^{18}O_{seawater}) + 0.1\ (\delta^{18}O_{calcite} - \delta^{18}O_{seawater})^2 \quad (2)$$

$\delta^{18}O$ values were converted from VPDB to VSMOW by the addition of 0.2 ‰ (Marchitto et al., 2014). There is a reported offset of -0.5 to -1.6 ‰ when using Shackleton (1974) with *N. pachyderma* (Jonkers et al., 2013). The selection of a different equation shifts the data by approximately -0.2 ‰ (e.g., Craig, 1965) or 0.4 ‰ (e.g., Kim and O'Neil, 1997), but does not change the trends reported.

The effect of continental ice sheets on $\delta^{18}O_{seawater}$ was corrected for using the stacked benthic isotopic records of Waelbroeck et al. (2002) and incorporating a full glacial-interglacial shift of 1.1‰ (Chappell and Shackleton, 1986; Schrag et al, 1996).

3. Results

3.1 *N. pachyderma* and *G. bulloides* stable isotopes

The $\delta^{18}O_{calcite}$ values recorded by both species of planktonic foraminifera are similar, showing decreased (~1 ‰) values during MIS 3 interstadials (Figure 3.2H and I). The average and ranges of the 2 species are statistically indistinguishable until 14.5 to 10 ka where the variability of *G. bulloides* increases, and the running standard deviation (calculated from a 3 kyr moving average) increases from 0.15 to 0.50 (Figure 3.2H). During the Bølling/Allerød, *N. pachyderma* $\delta^{18}O_{calcite}$ values decrease from ~ 3.2 to 1.5 ‰, increase to 2.5 ‰ during the Younger Dryas, and decrease to ~1.7 ‰ moving into the Holocene (Figure 3.2I).

3.2 Mg/Ca and ocean temperatures

N. pachyderma Mg/Ca values ranged between 0.594 mmol/mol at 31.9 ka during Heinrich event 3, and 1.74 mmol/mol at 41.2 ka during DOI 10. *G. bulloides* Mg/Ca values ranged between 0.79 after the Last Glacial Maximum (LGM) at 19.2 ka, and 1.74 during the deglacial at 18.4 ka. Due to low abundance in sampled intervals between 30-40 ka, the analytical

resolution of the *G. bulloides* Mg/Ca data set is too low to capture centennial scale variations. *N. pachyderma* samples were analyzed at sufficient resolution to reveal a high degree of variability in Mg/Ca values, >1 standard deviation (exceeds 0.2), between 46.7 to 46.2, 41.2 to 40, 37.3 to 36, 34.7 to 30.1, 28.9 to 27.7, 25.8 to 25, 24.3 to 22.9 and 14.4 to 11.4 ka. Positive excursions of >1 standard deviation from mean temperatures occur in short (<100 year) intervals (Figure 3.2B and C). These intervals of high variability, with the exception of 25.8-25 ka, coincide with DOIs (specifically DOI 12, 9, 8, 6, 5, 4, 3 and 2) and the Bølling/Allerød as measured in NGRIP (NGRIP members, 2004; Blockley et al., 2012).

Between 35 and 51 ka, anomalously warm ocean temperatures (7-12˚C) occur during DOI 7-13 (Figure 3.2D and E). From 24-35 ka, warm ocean temperatures are coincident with DOI 3-6, but also frequently occur during DO stadials. From 17-24 ka, ocean temperature variation is muted, and maximum ocean temperatures are cooler (mean value: 8.3˚C). Ocean temperatures warm after 17 ka, reaching a maximum of ~11˚C during the Bølling/Allerød warming at 14.8 ka, and then cooling to 3˚C at 12.2 ka during the Younger Dryas.

3.3 Reconstructed $\delta^{18}O_{seawater}$

Reconstructed $\delta^{18}O_{seawater}$ (ice volume corrected) values are positively related to the record of ocean temperatures, where relatively light (heavy) values are coincident with cooler (warmer) ocean temperatures (Figure 3.2F and G). Values range from 1.21 ‰ to -1.93 ‰ (*N. pachyderma*) and from 1.27 ‰ to -1.23 ‰ (*G. bulloides*). For comparison, modern surface $\delta^{18}O_{seawater}$ in the northeastern Pacific varies between 0.2 ‰ in the ETNP, and -0.3 ‰ on the California margin to -1.0 ‰ offshore of Vancouver Island (LeGrande and Schmidt, 2006). The variability in *N. pachyderma* $\delta^{18}O_{seawater}$ from one sample interval to the next is consistently lowest (<0.4 ‰) between 25 and 15 ka (Figure 3.2G). It is also lower during this interval for

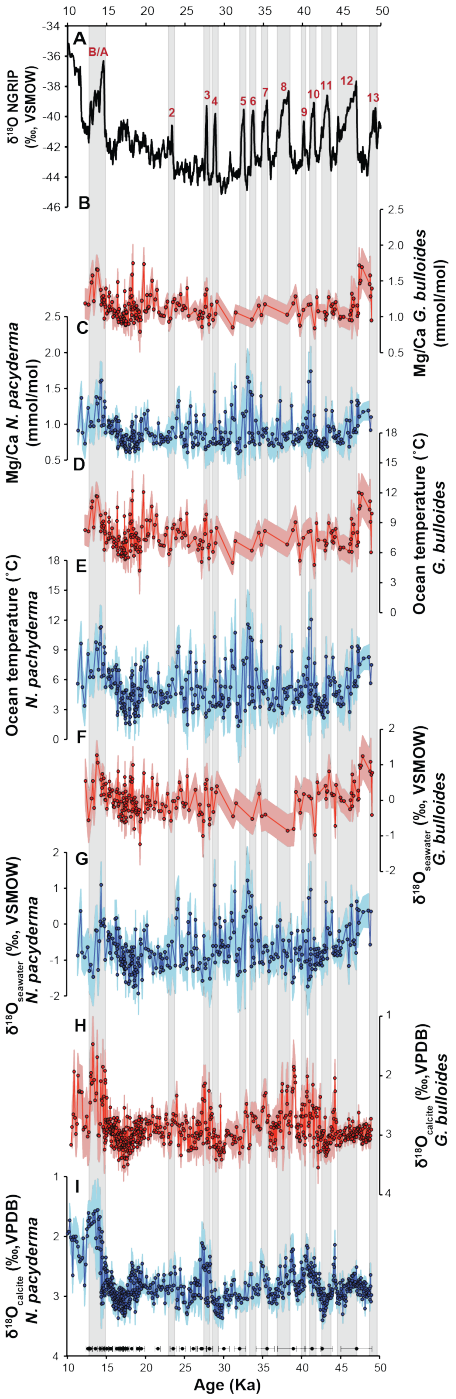

Figure 3.2
Top panel (A) NGRIP $\delta^{18}O$ (black line) and DOIs numbered in red and shaded in gray (NGRIP members, 2004; Blockley et al., 2012). For panels B-I, *G. bulloides* samples are red circles and red lines. Width represents running (2 kyr) standard deviation. *N. pachyderma* samples are blue circles and blue lines. Width represents running (2 kyr) standard deviation of samples. Measured Mg/Ca of the planktonic foraminifera species (B) *G. bulloides* and (C) *N. pachyderma*. Calculated SSTs for *G. bulloides* (D) and *N. pachyderma* (E), and calculated $\delta^{18}O_{seawater}$ for *G. bulloides* (F) and for *N. pachyderma* (G). Bottom panels show $\delta^{18}O_{calcite}$ for *G. bulloides* (H) and *N. pachyderma* (I) (Hendy and Cosma, 2008) with calibrated radiocarbon tie points (black circles) and age model error calculated from Bacon 2.2 (Blaauw and Christen, 2011) marked along the bottom axis.

G. bulloides although it is also low between 40 and 30 ka, probably as the *G. bulloides* record is poorly resolved through this interval due to insufficient specimens (Figure 3.2F).

4. Discussion

The preferential habitats of the two planktonic foraminiferal species, *G. bulloides* and *N. pachyderma* (s.), employed at MD02-2496 have not been directly observed within the Vancouver margin. Generally *G. bulloides* tolerate a wide temperature range (6-26°C) and are found in surface waters, but also dominate during cool upwelling conditions (0-20 m; Kuroyanagi and Kawahata, 2004, Sautter and Thunell, 1989). This depth habitat is confirmed by measurements of Mg/Ca and stable isotope geochemistry of *G. bulloides* in Southern California (Sautter and Thunell, 1989; Pak et al., 2004). *N. pachyderma* (s.) live within the pycnocline in the Japan sea, and is associated with ocean temperatures cooler than 8°C (~20-40 m; Kuroyanagi and Kawahata, 2004). This species dominates the foraminiferal fauna in weakly stratified subpolar water (Reynolds and Thunell, 1986). While the calibration equations used actually reconstructs the temperature at which foraminiferal calcification occurred, for simplicity we will refer to calcification temperatures hereafter as sea surface temperatures (SSTs). At MD02-2496, the reconstructed temperatures of *G. bulloides* are an average of 2.5˚C warmer than *N. pachyderma* (s.), although the standard deviation of both sets of temperatures (*N. pachyderma* stdev = 2.1˚C, *G. bulloides* stdev = 1.6˚C) frequently overlap, suggesting that the two species occupy a similar depth habitat or that the water column is weakly stratified (Figure 3.3). Additionally reconstructed SSTs from MD02-2496 are in good agreement with a shorter (0-16 ka) alkenone-based sea surface temperature record taken approximately 13 km to the southeast (JT96-09mc) (Kienast and McKay, 2001; Taylor et al., 2014). The ocean temperatures recorded off the Vancouver margin over 45 ka have a broad range (1˚ to 12˚C) encompassing abrupt SST

warming and glacial-interglacial climate change. For reference, the modern annual surface ocean temperature range is 8-14˚C, recorded at the nearby Station Papa for the past 50 years (http://www.pac.dfo-mpo.gc.ca/science/oceans/data-donnees/line-p/index-eng.html).

4.1 MD02-2496 records of DOI events

We compare 300-year running averages of $\delta^{18}O_{calcite}$ reconstructed $\delta^{18}O_{seawater}$, and SSTs from MD02-2496 and ODP-1017E in order to minimize the effects of outliers on interpretation of noisy records (Figure 3.3, 3.4, 3.5). Within age model error, normalized SSTs and $\delta^{18}O_{seawater}$ from MD02-2496 show relatively warm/saline surface conditions during DOIs 12, 11, and 9-10 (Figure 3.4). $\delta^{18}O_{calcite}$ values are more negative during these DOIs, although the excursions are less pronounced than in the SST and $\delta^{18}O_{seawater}$ records (Figure 3.6). SST and $\delta^{18}O_{seawater}$ reconstructions show a lesser response than $\delta^{18}O_{calcite}$ during DOI 8 with weakly warm/saline conditions (Figure 3.4). Generally during this interval, SSTs are warming from ~3-6˚C to 6-8˚C, or an amplitude (from the 300-year smoothing) of 3˚C, which is consistent with records to the south at ODP-1017E where 300-year running average *G. bulloides* reconstructed SST warming from ~7-8˚C to 11-12 ˚C, or an amplitude of 4˚C (Figure 3.3). Cross correlation analysis between *N. pachyderma* $\delta^{18}O_{calcite}$ and SSTs at MD02-2496 show that they are often strongly negatively correlated (> 0.9) between 50 and 30 ka, with exceptions during DOI 12 and 8 where the amplitude and duration of these intervals are mismatched (Figure 3.5). The $\delta^{18}O_{calcite}$ record shows a sequence of 3 negative excursions during DOIs 6-7, that are smaller than those during previous DOIs, and generally decreasing into Greenland stadial/H3 (Figure 3.4 and 3.5). In contrast reconstructed SSTs and $\delta^{18}O_{seawater}$ show increased warming/salinity starting after DOI 7 and sustained throughout the stadial/H3 around 30 ka (Figure 3.4 and 3.5).

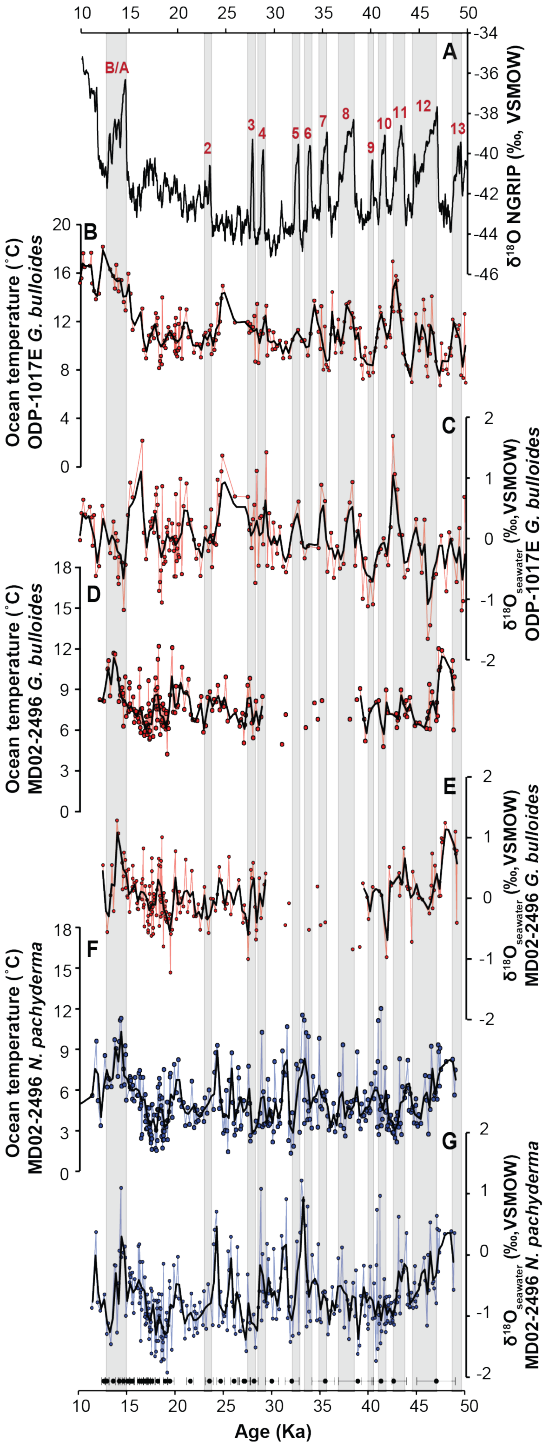

Figure 3.3
Top panel (A) NGRIP $\delta^{18}O$ (black line) and DOIs numbered in red and shaded in gray (NGRIP members, 2004; Blockley et al., 2012). Reconstructed SSTs (B) and $\delta^{18}O_{seawater}$ (C) from *G. bulloides* (red circles) and red line width represents running (2 kyr) standard deviation at site ODP-1017E, Point Conception, CA (Pak et al., 2012). Reconstructed SSTs (D) and $\delta^{18}O_{seawater}$ (E) from *G. bulloides* (red circles) from core site MD02-2496 are plotted in red circles and red line width represents running (2 kyr) standard deviation. Reconstructed SSTs (F) and $\delta^{18}O_{seawater}$ (G) from *N. pachyderma* (blue circles) and blue line width represents running (2 kyr) standard deviation of samples. Calibrated radiocarbon tie points (black circles) and age model error calculated from Bacon 2.2 (Blaauw and Christen, 2011) are marked along the bottom axis.

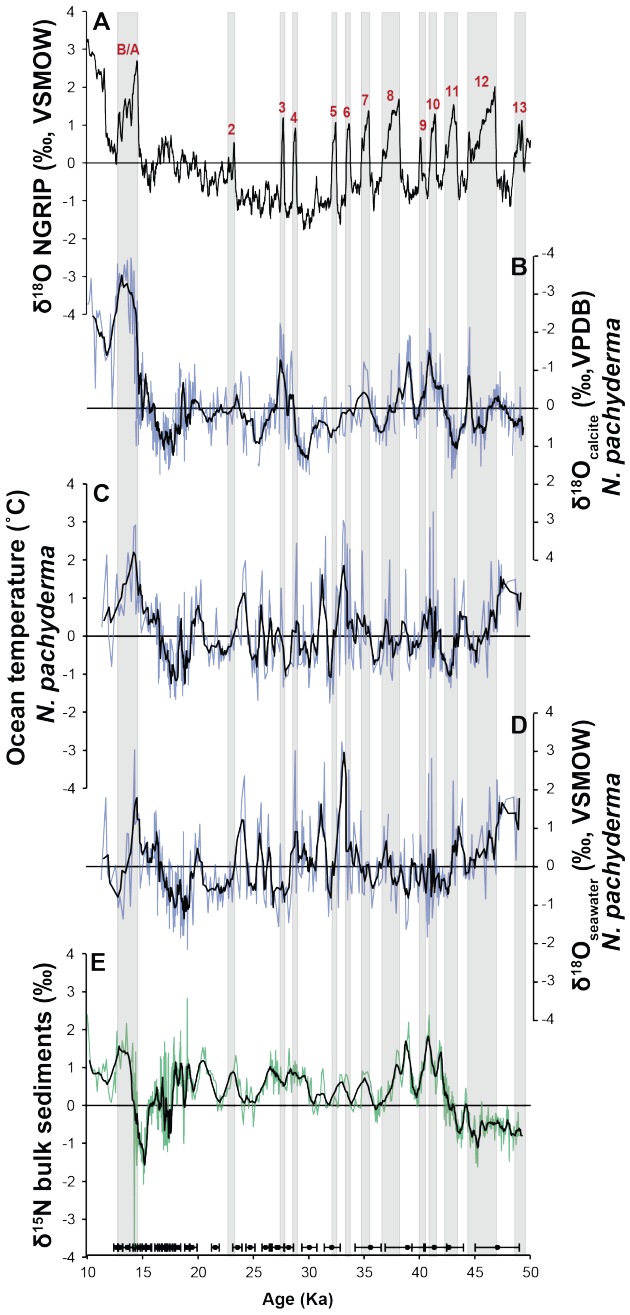

Figure 3.4
All panels (A-E) normalized to zero mean and unit variance. Top panel (A) NGRIP $\delta^{18}O$ (black line) and DOIs numbered in red and shaded in gray (NGRIP members, 2004; Blockley et al., 2012). B) Normalized *N. pachyderma* $\delta^{18}O_{calcite}$ (blue line) (Hendy and Cosma, 2008) and running (1 kyr) average (black line), (C) normalized *N. pachyderma* SST (blue line) and running (1 kyr) average (black line), (D) normalized *N. pachyderma* $\delta^{18}O_{seawater}$ (blue line) and running (1 kyr) average (black line), and (E) normalized $\delta^{15}N$ of bulk sediments (green line) and running (1 kyr) average (black line) (Chang et al., 2012) from MD02-2496, with calibrated radiocarbon tie points (black circles) and age model error calculated from Bacon 2.2 (Blaauw and Christen, 2011) marked along the bottom axis.

The SST shifts in N. pachyderma increase during this time to 5˚C, warming from an average of 3 to 8˚C, while the magnitude of SST increase does not change for G. bulloides at MD02-2496 or in ODP-1017, suggesting that either subsurface warming has increased or that the *N. pachyderma* record is noisier during this interval (Figure 3.3).

Coincident with DOIs 3-4, the $\delta^{18}O_{calcite}$ went negative by ~1 ‰ (Figure 3.6) while coeval SSTs and $\delta^{18}O_{seawater}$ were relatively cool/fresh and weakly warm/saline (Figure 3.4). $\delta^{18}O_{calcite}$ increases and remains relatively stable from ~ 25 to 17 ka, while SSTs and $\delta^{18}O_{seawater}$ show increased warming/salinity through Greenland stadial/H2, which can also be seen in a coincident warming in the record at ODP-1017 to >12˚C (Figure 3.3 and 3.4). After DOI 2, at around 20 ka, SSTs and $\delta^{18}O_{seawater}$ indicate relatively warm/saline conditions (warming of ~2˚C of all records), followed by a cooling just before Greenland stadial/H1 and then a significant warming during the Bølling/Allerød (Figure 3.3 and 3.4). Alkenone derived SSTs from the Okhotsk Sea in the subpolar northwestern Pacific showed increases during DOIs between 20-60 ka of between 6-8˚C, although these SST anomalies were accompanied by surface ocean freshening that is not observed in the northeastern Pacific (Harada et al., 2008).

$\delta^{18}O_{seawater}$ exhibits relatively large, high frequency $\delta^{18}O_{seawater}$ shifts (> 0.4 ‰) in records at MD02-2496 and ODP-1017 occur approximately twice per kyr in coherence with SST warming (Figure 3.3) (Pak etal., 2012). While these shifts are less frequent in the *G. bulloides* record, notably in the low resolution interval of the record, shifts in excess of 0.4 ‰ do persist (Figure 3.3). Although it might be argued that the variability in the $\delta^{18}O_{seawater}$ records is an artifact of the variable SST record, large shifts (>1‰) $\delta^{18}O_{calcite}$ that occur between 30-25 ka support real variability in the SST and $\delta^{18}O_{seawater}$ records (Figure 3.2H and I,; Figure 3.6B). Assuming a similar geographical $\delta^{18}O_{seawater}$ distribution during the last glacial, $\delta^{18}O_{seawater}$ shifts

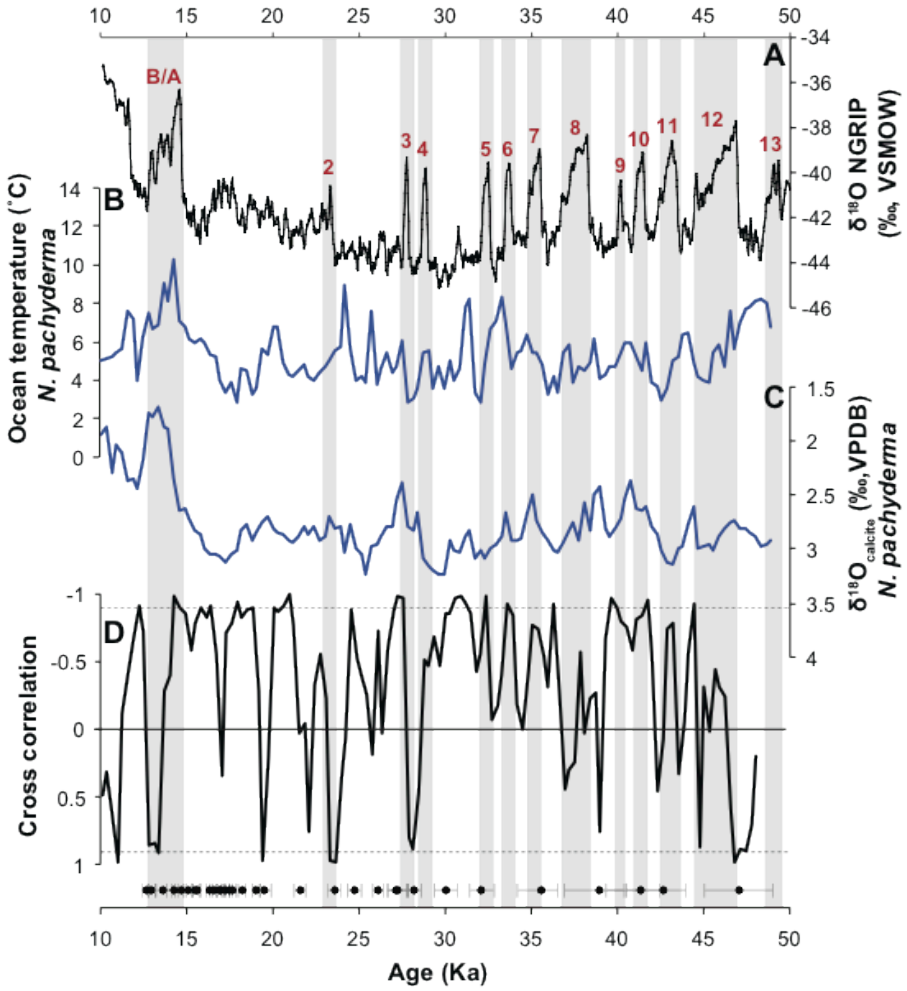

Figure 3.5
Top panel (A) NGRIP $\delta^{18}O$ (black line) and DOIs numbered in red and shaded in gray (NGRIP members, 2004; Blockley et al., 2012). MD02-2496 records of calculated *N. pachyderma* SST (B) *N. pachyderma* $\delta^{18}O_{calcite}$ (Hendy and Cosma, 2008) (C) were resampled at 300-years (blue lines) and a running cross correlation was measured between *N. pachyderma* SST and $\delta^{18}O_{calcite}$ for a 1 ka moving window (black line) with calibrated radiocarbon tie points (black circles) and age model error calculated from Bacon 2.2 (Blaauw and Christen, 2011) marked along the bottom axis.

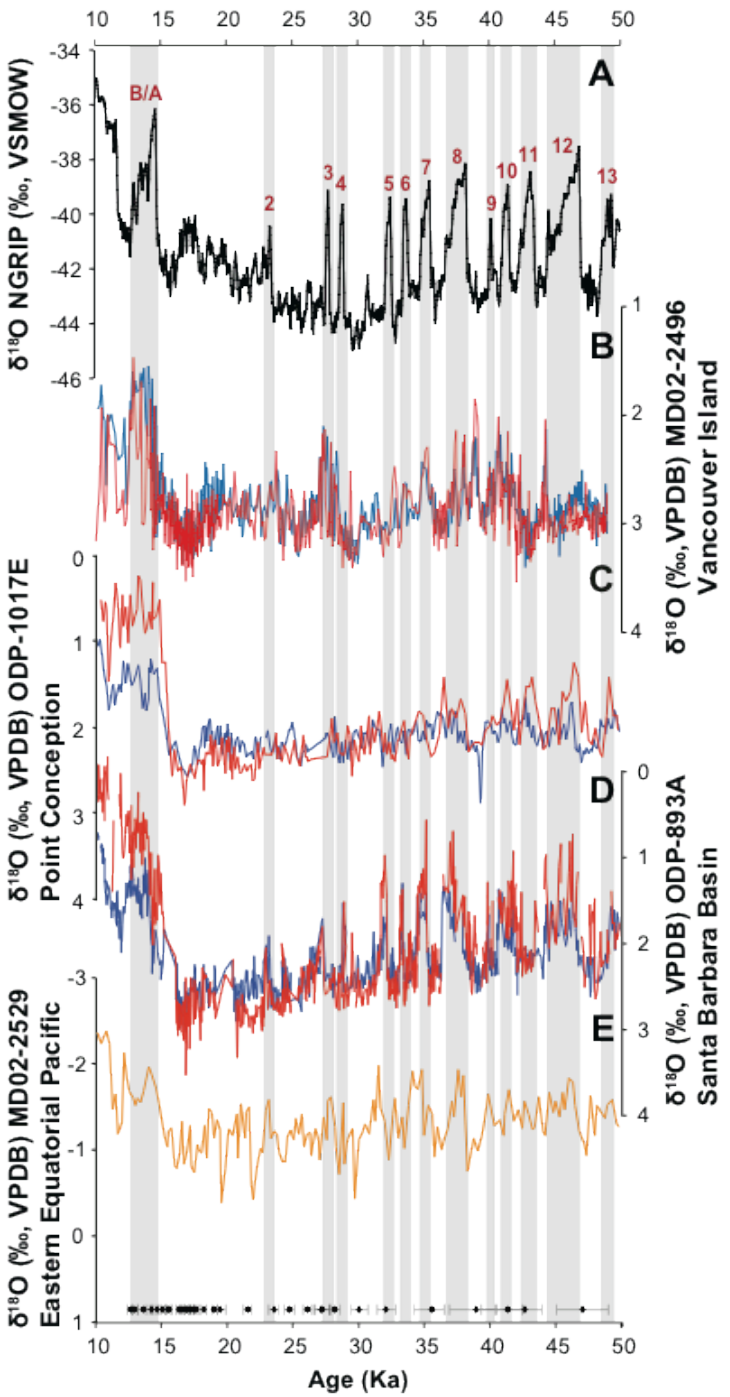

Figure 3.6
Top panel (A) NGRIP $\delta^{18}O$ (black line) and DOIs numbered in red and shaded in gray (NGRIP members, 2004; Blockley et al., 2012). B) $\delta^{18}O_{calcite}$ of *N. pachyderma* (blue line) (Hendy and Cosma, 2008) and *G. bulloides* (red line) from core site MD02-2496, Vancouver Island, CA, C) $\delta^{18}O_{calcite}$ of *N. pachyderma* (blue line) and *G. bulloides* (red line) at site ODP-1017E, Point Conception, CA (Hendy 2010), D) $\delta^{18}O_{calcite}$ of *N. pachyderma* (blue line) and *G. bulloides* (red line) at site ODP-893A, Santa Barbara, CA (Hendy et al., 2002), and E) $\delta^{18}O_{calcite}$ of *G. ruber* (orange line) from MD02-2529, Costa Rica (8˚12.33' N latitude, 84˚ 7.32' W longitude, 1619 m water depth) (Leduc et al., 2007) with calibrated radiocarbon tie points (black circles) and age model error calculated from Bacon 2.2 (Blaauw and Christen, 2011) marked along the bottom axis.

of 0.5 ‰ would imply waters coming from offshore Baja, CA, while larger shifts fall outside modern observations (Legrande and Schmidt., 2006).

Global scale mechanisms, such as expansion of sea ice in the northern North Pacific, could influence $\delta^{18}O_{seawater}$ at MD02-2496. During the Heinrich 1 and Younger Dryas stadials, the sea-ice boundary was shifted southward in the Okhotsk and western Bering Seas (Max et al., 2013). Records in the Okhotsk Sea have shown millennial scale expansion of sea ice during stadials and sea surface freshening corresponding to interstadials extending back to the beginning of MIS 3 (Harada et al., 2008; Riethdorf et al., 2013). However, recent modeling has shown that the isotopic shifts from interglacial to glacial intervals due to sea ice expansion were small, increasing by 0.12 ‰ in the North Atlantic surface waters (Brennan et al., 2013).

Changes in the tropical hydrologic cycle in response to shifts in the average position of the ITCZ and intensity of the Asian monsoon could also influence $\delta^{18}O_{seawater}$ at MD02-2496. Gibbons et al. (2014) estimate a shift in surface water $\delta^{18}O_{seawater}$ during deglacial stadials of up to ~0.6 ‰ in the eastern tropical Pacific via southward movement of the ITCZ resulting in decreased water vapor export from the Atlantic to the Pacific tropical basins and resulting in increased salinity in the eastern equatorial Pacific (Figure 3.6E) (Leduc et al., 2009; Leduc et al., 2010).

$\delta^{18}O_{calcite}$ values have been employed in a number of paleoceanographic studies to characterize DOI events in the North Pacific (Leduc et al., 2009; Kennett et al., 2000; Hendy and Kennett, 2000). Similarly the $\delta^{18}O_{calcite}$ records of both *G. bulloides* and *N. pachyderma* at MD02-2496 demonstrate rapid climate variability during DOIs (Hendy and Cosma, 2008) (Figure 3.6B). $\delta^{18}O_{calcite}$ at MD02-2496 appears to be influenced strongly by both temperature and changes in salinity, and $\delta^{18}O_{seawater}$ shifts towards positive values often coincide with warmer

ocean temperatures. During the minimal ice sheet extent of ~30 and 50 ka and during the deglacial, SSTs and $\delta^{18}O_{calcite}$ were often in phase (negatively correlated) while, during intervals of ice sheet growth the records were strongly anti-correlated (Figure 3.5). Moreover, SST warming and positive $\delta^{18}O_{seawater}$ values were not expressed in the $\delta^{18}O_{calcite}$ record during some NGRIP stadials after 30 ka (Figure 3.4) (NGRIP members, 2004). As large shifts in both salinity and temperature are implied in the SST reconstruction at MD02-2496, the $\delta^{18}O_{calcite}$ record alone is insufficient to understand the surface water characteristics in the NE Pacific. Recent observations of isotopic decoupling during the deglacial in the Gulf of Alaska showed that $\delta^{18}O_{calcite}$ became inversely correlated with NGRIP $\delta^{18}O$ from 18 to 16 ka, and then became significantly synchronized during the Bølling/Allerød and Holocene (Davies et al., 2011; Praetorius and Mix, 2014). At MD02-2496, after the LGM, $\delta^{18}O_{calcite}$ becomes strongly decoupled from the NGRIP $\delta^{18}O$ record, suggesting that dynamic coupling between North Atlantic and North Pacific climate extends beyond the Gulf of Alaska (Figure 3.2A, H, I).

4.2 A Spicy California Undercurrent water mass

The CUC is characterized as warm, salty (spicy), nutrient-rich, oxygen-poor waters in contrast with the California Current, which is cold, fresh, nutrient poor and oxygen rich (Meinvielle and Johnson, 2013). Contribution of tropically sourced waters from the CUC is another modern driver of decadal salinity variability along the Vancouver margin, where saline intermediate waters consisting of at least 30% ETNP waters advected poleward by the CUC are pumped to the surface via upwelling (Foreman et al., 2008; Thomson and Krassovski, 2010). With modern climate warming, increased ETNP water advection into higher latitudes via the CUC has been established by observations of a sharp decrease in subsurface dissolved oxygen concentration and increase in spicy water along the west coast of North America between 25˚

and 50˚ N latitude (Meinvielle and Johnson, 2013). This is consistent with both an increase in transport of the CUC, and shoaling of the core CUC such that a greater proportion of ETNP waters are upwelled onto the continental shelf (Meinvielle and Johnson, 2013).

High bulk sedimentary $\delta^{15}N$ values are produced by denitrification within the ETNP oxygen minimum zone, and carried northward with the CUC along the eastern Pacific margin, thereby operating as a proxy for the relative strength of the current (Kienast et al., 2002; Chang et al., 2008). The general coherence of the $\delta^{15}N$ records along the northeastern Pacific margin is suggestive of large-scale processes dominating the $\delta^{15}N$ signal (Kienast et al., 2002; Hendy et al., 2004; Chang et al., 2008; Galbraith et al., 2008). The CUC brings relatively denitrified, low oxygen spicy waters to the extratropics, with a core flow along the continental slope, upwelling onto the continental margin. Records on the North American margin have demonstrated coherence between millennial scale climate change and $\delta^{15}N$ of bulk sediments at MD02-2496 (Chang et al., 2008), indicating that sediments were more enriched in ^{15}N during DOIs of MIS 3. This has been interpreted as a higher influx of ETNP-sourced, denitrified waters during DOIs, with the California Current System serving to physically link the ETNP to the northeastern Pacific from the Mexican margin as far north as the Vancouver Margin (Kienast et al., 2002; Galbraith et al., 2008; Chang et al., 2008; Hendy et al., 2004).

Comparison of normalized bulk sediment $\delta^{15}N$ at MD02-2496 with coincident SST and stable isotope samples provides a more robust identification of changes in CUC strength on the Vancouver margin (Figure 3.4), where coeval enrichments in both MD02-2496 bulk sedimentary $\delta^{15}N$ (Chang et al., 2008) and relatively warm/saline waters support increased ETNP advection to the Vancouver Margin. Variations in $\delta^{15}N$ and *N. pachyderma* $\delta^{18}O_{calcite}$, $\delta^{18}O_{seawater}$, and SST records (Figure 3.4) indicate that positive anomalies in both records were co-incident within age

model error with DOIs 6-11. $\delta^{15}N$ values are higher during DOI 6/7 and then decrease slightly from ~32 ka to 29.5 ka, during the NGRIP stadial/H3 (NGRIP members, 2004). Values increase again after 30 ka, roughly coinciding with DOIs 3 and 4 until ~26 ka, decline again briefly during another NGRIP stadial/H2, and increase again during DOI 2 and at 20 ka, and during the Bølling/Allerød warming. These more enriched $\delta^{15}N$ values generally coincide with relatively warm SSTs/salinity, although enrichment decreases during NGRIP stadials (Figure 3.4). During the last deglaciation (15-17 ka), the penultimate deglaciation after 45 ka, depletion in $\delta^{15}N$ at MD02-2496 resulted from increased terrestrial organic carbon flux to the sediments as the CIS retreated (Chang et al., 2014). Thus surface water chemical characteristics indicate that during large DOI events, there was a greater influence of CUC water in surface waters off Vancouver Island, Canada but as the ice sheets grew during the last glacial, this relationship was lost. To the south, at ODP-1017E, millennial scale variability in surface waters through the last glacial was also dominated by changes in water mass spiciness (Hendy et al., 2004; Pak et al., 2012). These trends support the presence of the CUC during early DOIs, and then intermittent and less predictable CUC flow through the LGM as local ocean circulation dominated the Vancouver Margin.

Several possible mechanisms driving CUC strengthening during past DOIs exist. A relationship between abrupt warming in the North Atlantic and northward movement of the ITCZ has been identified in paleoclimate records (Leduc et al., 2009; Deplazes et al., 2013), which may have enhanced the sea surface height at the southern boundary of the CCS, increasing poleward flow of the CUC. Upwelling is also associated with interstadials along the California margin and may serve to strengthen the CUC on the northern end of the CCS (Hendy et al., 2004). It is also possible that warm saline water may also be advected to the site via the North

Pacific Drift (NPD). A SST reconstruction from the Northwestern Pacific (MD01-2404) exhibits warming during similar intervals after 30 ka, which has been attributed to dynamic heat transport of the Kuroshio Current in response to Antarctic warming (Chen et al., 2010). As the Kuroshio Current feeds into the NPD, this reconstruction provides an additional mechanism to explain warm saline water at MD02-2496, however, water advected via the NPD does not contain enriched $\delta^{15}N$.

4.3 Local influences and conditions

Regional influences on $\delta^{18}O_{seawater}$ at MD02-2496 may offer one explanation for the lack of coherency between MD02-2496 and other proxy records along the NE Pacific margin between 30 and 20 ka. These regional factors include changes in precipitation/evaporation balances and changes in ocean circulation, while local variability in the wind stresses could produce the high frequency temperature variability on the Vancouver margin during this interval. On the modern ice-free Vancouver Margin, fresh waters are tidally mixed with ocean currents entering the Straits, mixing with seasonally upwelled waters flowing onto the continental shelf (Cummins and Masson, 2014). However, the effect of the ice sheet growth during the interval from 30 to the LGM could have played an important role in overprinting global climate events. With the growth of the CIS, the buoyancy driven current system would not have existed in its modern form (Taylor et al, 2014). During the LGM grounded ice on the Vancouver Island continental shelf filled the straits (Mosher and Hewitt, 2004) where tidal mixing would have occurred. Grounded ice extended as far as the shelf break south of MD02-2496 (~49.5˚N) where ice from the Juan de Fuca Strait and the Barkley Sound coalesced into a large piedmont glacial lobe.

Modern ocean temperatures in this region are also influenced by the latitudinal position of the NPC, which can vary considerably over short times scales (~8˚ latitude in 2002) as a result

of stochastic wind forcing (Sydeman et al., 2011), leading to sea surface cooling of ~1˚C (Freeland et al., 2003). The average latitude of NPC bifurcation is 42-52˚N. Bifurcation of the NPC to the north of its average position results in enhanced advection of cool/fresh subarctic waters into the CCS (Sydeman et al., 2011). It is possible that the bifurcation of the NPC moved south as global climate cooled towards the LGM.

At present, variability in ocean temperatures and salinities along the Vancouver margin are in part a manifestation of noisy atmospheric forcing and coastal precipitation/runoff with SST and salinity anomalies ranging by ±2 (˚C, PSU) over the last 70 years (Cummins and Masson, 2014). Ocean temperature anomalies are significantly correlated with fall/winter wind stress, while local salinity is primarily controlled by fluctuations of coastal freshwater runoff (Cummins and Masson, 2014). The seasonal input of freshwater runoff changed dramatically as the Cordilleran Ice Sheet grew from 30 to the LGM as winter precipitation entered coastal waters during summer.

Thus, while seawater proxies on the Vancouver margin are recording broad scale changes in circulation via atmospheric reorganization during the last glacial, surface ocean characteristics such as salinity and temperature may also be subject to overprinting by very local processes such as variable inshore upwelling and freshwater runoff via meltwater.

4.4 North Atlantic and North Pacific teleconnections

Alternatively, the breakdown of coherency between North Atlantic and North Pacific climate may be related to changes in large scale atmospheric circulation coincident with the growth of the LIS and CIS after 30 ka. Modeling studies have shown that ice sheet topography is a dominant factor altering northern hemisphere extratropical atmospheric circulation, and may change the strength and position of the subtropical jet, thereby altering storm tracks (COHMAP

members, 1988; Pausata et al., 2011; Beghin et al., 2014; Zhang et al., 2024). The westerly winds are posited as one method of teleconnection between the North Atlantic and North Pacific, communicating SSTs changes between basins (COHMAP members, 1988; Timmerman et al., 2004). Small changes in ice sheet topography have also been posited as a mechanism for DOIs as a result of splitting and shifting westerly winds to the North in the Atlantic (Zhang et al., 2014). As North American ice sheets grew to maximum extent at the LGM, model results suggest that the westerlies could have weakened, causing a warming in the eastern North Pacific (COHMAP members, 1988; Timmermann et al., 2004). The topographic barrier formed by the LIS and the CIS alters atmospheric circulation in the North Pacific, Northern Canada, and Alaska during the LGM (Timmermann et al., 2004; Justino et al., 2005) that is coincident with apparent warming, independent from climate events in the North Atlantic, recorded by Mg/Ca-SSTs between 20 and 30 ka.

5. Conclusions

A 50 ka record of *G. bulloides* $\delta^{18}O_{calcite}$ and Mg/Ca-based SSTs from the Vancouver margin (MD02-2496) coupled with the previously published *N. pachyderma* $\delta^{18}O_{calcite}$ record (Hendy and Cosma, 2008), reveals a complex relationship between isotopic and SST records as ice sheets expanded during the last glacial. Large shifts in $\delta^{18}O_{seawater}$ were recorded, of at least 0.5 ‰. If the geographical $\delta^{18}O_{seawater}$ distribution during the last glacial was similar to the modern, $\delta^{18}O_{seawater}$ increases of 0.5 ‰ would imply waters coming from offshore Baja, CA, but larger positive shifts cannot be explained by advection of tropical waters alone. At MD02-2496 and ODP-1017, large variability in the reconstructed SST records show that on the NE Pacific margin $\delta^{18}O_{calcite}$ records alone may not be sufficient to resolve simultaneous temperature and salinity shifts.

Millennial-scale warming frequently coincided with positive anomalies in the $\delta^{15}N$ record, indicating that SST warming was associated with changes in water mass characteristics including spiciness and denitrification suggestive of increased transport of waters from the Eastern Tropical North Pacific via the California Undercurrent (CUC). Higher $\delta^{15}N$ values are recorded in sediment cores along the NE Pacific margin, suggestive of temporally coherent, large scale changes in the California Current System (CCS) and transport of tropical water northward (Kienast et al., 2002; Chang et al., 2008; Galbraith et al., 2008). Previous studies indicate a strong teleconnection between North Atlantic climate forcing, and the position of the Intertropical Convergence Zone (ITCZ) in the tropical North Pacific (Leduc et al., 2009; Okumura et al., 2009; Leduc et al., 2010; Deplazes et al., 2013). This may result in an increase in the relative strength of the CUC during SST warming at DOIs. CUC strengthening could have developed as sea surface heights increased at the southern end of the CCS when the ITCZ was displaced northward. While this teleconnection was communicated along the Pacific margin as far north as 50˚N latitude during early MIS 3, at MD02-2496 the teleconnection breaks down after 30 ka as ice sheet growth at mid- and high latitudes, increasingly impacted northern hemisphere atmospheric circulation patterns.

The interval between 20-30 ka displays an apparent decoupling between SSTs and $\delta^{18}O_{calcite}$. We interpret this lack of coherency as either an increase in the influence of local ocean circulation on seawater geochemistry as Cordilleran Ice Sheet growth changed local surface ocean circulation and the timing and composition of freshwater. Additionally the vertical expansion of the Laurentide Ice Sheet topography impacted westerly wind strength, causing SST anomalies in the North Pacific independent from DOIs (Timmermann et al., 2004; Justino et al.,

2005). At the Bølling/Allerød (14.7 ka), proxies for increased advection of ETNP sourced water mass become coherent once again.

References

Auad, G., D. Roemmich, and J. Gilson (2011), The California Current System in relation to the Northeast Pacific Ocean circulation, *Progress In Oceanography*, *91*(4), 576-592.

Barker, S., M. Greaves, and H. Elderfield (2003), A study of cleaning procedures used for foraminiferal Mg/Ca paleothermometry, *Geochemistry Geophysics Geosystems*, *4*(9), 8407.

Beghin, P., S. Charbit, C. Dumas, M. Kageyama, D. M. Roche, and C. Ritz (2014), Interdependence of the growth of the Northern Hemisphere ice sheets during the last glaciation: the role of atmospheric circulation, *Climate of the Past*, *10*(1), 345-358.

Behl, R. J., and J. P. Kennett (1996), Brief interstadial events in the Santa Barbara basin, NE Pacific, during the past 60 kyr, *Nature*, *379*(18), 243-246.

Bian, N., and P. A. Martin (2010), Investigating the fidelity of Mg/Ca and other elemental data from reductively cleaned planktonic foraminifera, *Paleoceanography*, *25*(2), PA2215.

Blaauw, M., and J. A. Christen (2011), Flexible paleoclimate age-depth models using an autoregressive gamma process. *Bayesian Analysis 6,* 457–474.

Blockley, S. P. E., et al. (2012), Synchronisation of palaeoenvironmental records over the last 60,000 years, and an extended INTIMATE1 event stratigraphy to 48,000 b2k, *Quaternary Science Reviews*, *36*(C), 2-10.

Boyle, E. A., and L. D. Keigwin (1985), Comparison of Atlantic and Pacific paleochemical records for the last 215,000 years: changes in deep ocean circulation and chemical inventories, *Earth and Planetary Science Letters*, *76*, 135-150.

Brennan, C. E., K. J. Meissner, M. Eby, C. Hillaire-Marcel, and A. J. Weaver (2013), Impact of sea ice variability on the oxygen isotope content of seawater under glacial and interglacial conditions, *Paleoceanography*.

Cannariato, K. G., and J. P. Kennett (1999), Climatically related millennial-scale fluctuations in strength of California margin oxygen-minimum zone during the past 60 k.y., *Geology*, *27*, 975-978.

Chang, A. S., T. F. Pedersen, and I. L. Hendy (2008), Late Quaternary paleoproductivity history on the Vancouver Island margin, western Canada: a multiproxy geochemical study, *Canadian Journal of Earth Sciences*, *45*(11), 1283-1297.

Chang, A. S., T. F. Pedersen, and I. L. Hendy (2014), Effects of productivity, glaciation and ventilation on late Quaternary sedimentary redox and trace element accumulation on the Vancouver Island margin, western Canada, *Paleoceanography, 29,* PA002581.

Chappell, J., and N. J. Shackleton (1986), Oxygen isotopes and sea level, *Nature*, *324*, 137-140.
Chelton, D. B., and R. E. Davis (1982), Monthly mean sea-level variability along the west coast of North America, *Journal of Physical Oceanography*, *12*, 757-784.

Chen, M. T., X. P. Lin, Y. P. Chang, Y. C. Chen, L. Lo, C. C. Shen, Y. Yokoyama, D. W. Oppo, W. G. Thompson, and R. Zhang (2010), Dynamic millennial-scale climate changes in the northwestern Pacific over the past 40,000 years, *Geophysical Research Letters*, *37*(23), L23603.

COHMAP (1988), Climatic Changes of the Last 18,000 Years: Observations and Model Simulations, *Science*, *241*(4869), 1043-1052.

Connolly, T. P., B. M. Hickey, I. Shulman, and R. E. Thomson (2014), Coastal Trapped Waves, Alongshore Pressure Gradients, and the California Undercurrent*, *Journal of Physical Oceanography*, *44*(1), 319-342.

Cosma, T. N., I. L. Hendy, and A. S. Chang (2008), Chronological constraints on Cordilleran Ice Sheet glaciomarine sedimentation from core MD02-2496 off Vancouver Island (western Canada), *Quaternary Science Reviews*, *27*(9-10), 941-955.

Cummins, P. F., and H. J. Freeland (2007), Variability of the North Pacific Current and its bifurcation, *Progress In Oceanography*, *75*(2), 253-265.

Cummins, P. F., and D. Masson (2014), Climatic variability and trends in the surface waters of coastal British Columbia, *Progress In Oceanography*, *120*(C), 279-290.

Davies, M. H., A. C. Mix, J. S. Stoner, J. A. Addison, J. Jaeger, B. Finney, and J. Wiest (2011), The deglacial transition on the southeastern Alaska Margin: Meltwater input, sea level rise, marine productivity, and sedimentary anoxia, *Paleoceanography*, *26*(2), PA2223.

Denton, G. H., R. F. Anderson, J. R. Toggweiler, R. L. Edwards, J. M. Schaefer, and A. E. Putnam (2010), The last glacial termination, *Science*, *328*(5986), 1652-1656.

Deplazes, G., et al. (2013), Links between tropical rainfall and North Atlantic climate during the last glacial period, *Nature Geoscience*, *6*(3), 213-217.

Douglass, E., D. Roemmich, and D. Stammer (2006), Interannual variability in northeast Pacific circulation, *Journal of Geophysical Research*, *111*(C4), C04001.

Elderfield, H., and G. Gannsen (2000), Past temperature and $\delta^{18}O$ of surface ocean waters inferred from foraminiferal Mg/Ca ratios, *Nature*, *405*, 442-445.

Flament, P. (2002), A state variable for characterizing water masses and their diffusive stability: spiciness. *Progress In Oceanography 54*, 493–501.

Foreman, M. G. G., W. Callendar, A. MacFadyen, B. M. Hickey, R. E. Thomson, and E. Di Lorenzo (2008), Modeling the generation of the Juan de Fuca Eddy, *Journal of Geophysical Research*, *113*(C3), C03006.

Freeland, H. J. (2003), Cold halocline in the northern California Current: An invasion of subarctic water, *Geophysical Research Letters*, *30*(3), 1141.

Freeland, H. J. (2006), What Proportion of the North Pacific Current Finds its Way into the Gulf of Alaska?, *Atmosphere-Ocean*, *44*(4), 321-330.

Galbraith, E. D., M. Kienast, S. L. Jaccard, T. F. Pedersen, B. G. Brunelle, D. M. Sigman, and T. Kiefer (2008), Consistent relationship between global climate and surface nitrate utilization in the western subarctic Pacific throughout the last 500 ka, *Paleoceanography*, *23*(2), n/a-n/a.

Gibbons, F. T., D. W. Oppo, M. Mohtadi, Y. Rosenthal, J. Cheng, Z. Liu, and B. K. Linsley (2014), Deglacial δ18O and hydrologic variability in the tropical Pacific and Indian Oceans, *Earth and Planetary Science Letters*, *387*, 240-251.

Harada, N., M. Sato, and T. Sakamoto (2008), Freshwater impacts recorded in tetraunsaturated alkenones and alkenone sea surface temperatures from the Okhotsk Sea across millennial-scale cycles, *Paleoceanography*, *23*(3), PA2212.

Hendy, I. L. (2010), The paleoclimatic response of the Southern Californian Margin to the rapid climate change of the last 60 ka: A regional overview, *Quaternary International*, *215*(1-2), 62-73.

Hendy, I. L., and T. Cosma (2008), Vulnerability of the Cordilleran Ice Sheet to iceberg calving during late Quaternary rapid climate change events, *Paleoceanography*, *23*(2), PA2101.

Hendy, I. L., and J. P. Kennett (2000), Dansgaard-Oeschger Cycles and the California Current System: Planktonic foraminiferal response to rapid climate change in Santa Barbara Basin, Ocean Drilling Program Hole 893A, *Paleoceanography*, *15*(1), 30-42.

Hendy, I. L., and J. P. Kennett (2003), Tropical forcing of North Pacific intermediate water distribution during Late Quaternary rapid climate change?, *Quaternary Science Reviews*, *22*(5-7), 673-689.

Hendy, I. L., J. P. Kennett, E. B. Roark, and B. L. Ingram (2002), Apparent synchroneity of submillennial scale climate events between Greenland and Santa Barbara Basin, California from 30–10 ka, *Quaternary Science Reviews*, *21*, 1167-1184.

Hendy, I. L., and T. F. Pedersen (2005), Is pore water oxygen content decoupled from productivity on the California Margin? Trace element results from Ocean Drilling Program Hole 1017E, San Lucia slope, California, *Paleoceanography*, *20*(4), PA4026.

Hendy, I. L., T. F. Pedersen, J. P. Kennett, and R. Tada (2004), Intermittent existence of a southern Californian upwelling cell during submillennial climate change of the last 60 kyr, *Paleoceanography*, *19*(3), PA3007.

Hickey, B. M., and N. S. Banas (2008), Why is the northern end of the California Current system so productive?, *Oceanography*, *21*(4), 90-107.

Jonkers, L., P. Jiménez-Amat, P. G. Mortyn, and G.-J. A. Brummer (2013), Seasonal Mg/Ca variability of *N. pachyderma* (s) and *G. bulloides*: Implications for seawater temperature reconstruction, *Earth and Planetary Science Letters*, *376*, 137-144.

Justino, F., A. Timmermann, U. Merkel, and E. P. Souza (2005), Synoptic Reorganization of Atmospheric Flow during the Last Glacial Maximum, *Journal of Climate*, *18*, 2826-2845.

Keigwin, L. D., and E. A. Boyle (1989), Late Quaternary paleochemistry of high-latitude surface waters, *Palaeogeography, Palaeoclimatology, Palaeoecology*(73), 85-106.

Kennett, J. P., E. B. Roark, K. G. Cannriato, B. L. Ingram, and R. Tada (2000), Latest Quaternary paleoclimatic and radiocarbon chronology, Hole 1017E, Southern California margin, *Proceedings of the Ocean Drilling Program, Scientific Results*, *167*, 249-254.

Kienast, S. S., S. E. Calvert, and T. F. Pedersen (2002), Nitrogen isotope and productivity variations along the northeast Pacific margin over the last 120 kyr: Surface and subsurface paleoceanography, *Paleoceanography*, *17*(4), 7-1-7-17.

Kienast, S. S., and J. L. McKay (2001), Sea surface temperatures in the subarctic northeast Pacific reflect millennial-scale climate oscillations during the last 16 kyrs, *Geophysical Research Letters*, *28*(8), 1563-1566.

Kim, S.-T., and J. R. O'Neil (1997), Equilibrium and nonequilibrium oxygen isotope effects in synthetic carbonates, *Geochimica et Cosmochimica Acta*, *61*(16), 3461-3475.

Kuroyanagi, A., and H. Kawahata (2004), Vertical distribution of living planktonic foraminifera in the seas around Japan, *Marine Micropaleontology*, *53*(1-2), 173-196.

Leduc, G., L. Vidal, K. Tachikawa, F. Rostek, C. Sonzogni, L. Beaufort, and E. Bard (2007), Moisture transport across Central America as a positive feedback on abrupt climatic changes, *Nature*, *445*(7130), 908-911.

Leduc, G., L. Vidal, K. Tachikawa, and E. Bard (2009), ITCZ rather than ENSO signature for abrupt climate changes across the tropical Pacific?, *Quaternary Research*, *72*(1), 123-131.

Leduc, G., L. Vidal, K. Tachikawa, and E. Bard (2010), Changes in Eastern Pacific ocean ventilation at intermediate depth over the last 150 kyr BP, *Earth and Planetary Science Letters*, *298*, 217-228.

LeGrande, A. N., and G. A. Schmidt (2006), Global gridded data set of the oxygen isotopic composition in seawater, *Geophysical Research Letters*, *33*(12), L12604.

Liu, K.-K., and I. R. Kaplan (1989), The eastern tropical Pacific as a source of ^{15}N-enriched nitrate in seawater off southern California, *Limnology and Oceanography*, *34*, 820-830.

Lynn, R. J., and J. L. Simpson (1987), The California Current system: The seasonal variability of its physical characteristics, *Journal of Geophysical Research*, *92*(C12), 12947-12966.

Manabe, S., and R. J. Stouffer (1988), Two stable equilibria of a coupled ocean-atmosphere model, *Journal of Climate*, *1*, 841-866.

Marchitto, T. M., W. B. Curry, J. Lynch-Stieglitz, S. P. Bryan, K. M. Cobb, and D. C. Lund (2014), Improved oxygen isotope temperature calibrations for cosmopolitan benthic foraminifera, *Geochimica et Cosmochimica Acta*, *130*(C), 1-11.

Martin, P. A., and D. W. Lea (2002), A simple evaluation of cleaning procedures on fossil benthic foraminiferal Mg/Ca, *Geochemistry Geophysics Geosystems*, *3*(10), 8401.

Masson, D., and P. F. Cummins (1999), Numerical simulations of a buoyancy-driven coastal countercurrent off Vancouver Island, *Journal of Physical Oceanography*, *29*, 418-435.

Masson, D., and I. Fine (2012), Modeling seasonal to interannual ocean variability of coastal British Columbia, *Journal of Geophysical Research*, *117*(C10), C10019.

Max, L., J.-R. Riethdorf, R. Tiedemann, M. Smirnova, L. Lembke-Jene, K. Fahl, D. Nurnberg, A. Matul, and G. Mollenhauer (2012), Sea surface temperature variability and sea-ice extent in the subarctic northwest Pacific during the past 15,000 years, *Paleoceanography*, *27*(3), PA3213.

Meinvielle, M., and G. C. Johnson (2013), Decadal water-property trends in the California Undercurrent, with implications for ocean acidification, *Journal of Geophysical Research: Oceans*, *118*(12), 6687-6703.

Mix, A. C., D. C. Lund, N. G. Pisias, P. Bodén, L. Bornmalm, M. Lyle, and J. Pike (1999), Rapid climate oscillations in the northeast Pacific during the last deglaciation reflect Northern and Southern Hemisphere sources, *Mechanisms of global climate change at millennial time scales*, 127-148.

Mosher, D. C., and A. T. Hewitt (2004), Late Quaternary deglaciation and sea-level history of eastern Juan de Fuca Strait, Cascadia, *Quaternary International*, *121*, 23-39.

Ohkushi, K., J. P. Kennett, C. M. Zeleski, S. E. Moffitt, T. M. Hill, C. Robert, L. Beaufort, and R. J. Behl (2013), Quantified intermediate water oxygenation history of the NE Pacific: A

new benthic foraminiferal record from Santa Barbara basin, *Paleoceanography*, *28*(3), 453-467.

Okumura, Y. M., C. Deser, A. Hu, A. Timmermann, and S.-P. Xie (2009), North Pacific climate response to freshwater forcing in the subarctic North Atlantic: Oceanic and atmospheric pathways, *Journal of Climate*, *22*(6), 1424-1445.

Pak, D. K., D. W. Lea, and J. P. Kennett (2004), Seasonal and interannual variation in Santa Barbara Basin water temperatures observed in sediment trap foraminiferal Mg/Ca, *Geochemistry Geophysics Geosystems*, *5*(12), Q12008.

Pak, D. K., D. W. Lea, and J. P. Kennett (2012), Millennial scale changes in sea surface temperature and ocean circulation in the northeast Pacific, 10–60 kyr BP, *Paleoceanography*, *27*(1), PA1212.

Pausata, F. S. R., C. Li, J. J. Wettstein, M. Kageyama, and K. H. Nisancioglu (2011), The key role of topography in altering North Atlantic atmospheric circulation during the last glacial period, *Climate of the Past*, *7*(4), 1089-1101.

Praetorius, S. K., and A. C. Mix (2014), Synchronization of North Pacific and Greenland climates preceded abrupt deglacial warming, *Science*, *345*(6195), 444-448.

Reimer, P. J., et al. (2013), INTCAL13 and MARINE13 radiocarbon age calibration curves 0-50,000 years cal BP, *Radiocarbon*, *55*(4), 1869-1887.

Riethdorf, J.-R., L. Max, D. Nurnberg, L. Lembke-Jene, and R. Tiedemann (2013), Deglacial development of (sub) sea surface temperature and salinity in the subarctic northwest Pacific: Implications for upper-ocean stratification, *Paleoceanography*, *28*(1), 91-104.

Sautter, L. R., and R. C. Thunell (1989), Seasonal succession of planktonic foraminifera: Results from a four-year time-series sediment trap experiment in the Northeast Pacific, *Journal of Foraminiferal Research*, *19*, 253-267.

Schrag, D. P., G. Hampt, and D. W. Murray (1996), Pore fluid constraints on the temperature and oxygen isotopic composition of the glacial ocean, *Science*, *272*(5270), 1930-1932.

Seki, O. (2002), Millennial climate oscillations in NE Pacific surface waters over the last 82 kyr: New evidence from alkenones, *Geophysical Research Letters*, *29*(23), 2144.

Shackleton, N. J. (1974), Attainment of isotopic equilibrium between ocean water and the benthonic foraminifera genus *Colloques Internationaux du C.N.R.S.*, *219*, 203-209.

Strub, P. T., and C. James (2002), Altimeter-derived surface circulation in the large-scale NE Pacific Gyres. Part 1. Seasonal variability, *Progress In Oceanography*, *53*, 163-183.

Sydeman, W. J., S. A. Thompson, J. C. Field, W. T. Peterson, R. W. Tanasichuk, H. J. Freeland, S. J. Bograd, and R. R. Rykaczewski (2011), Does positioning of the North Pacific Current affect downstream ecosystem productivity?, *Geophysical Research Letters*, *38*(12), L12606.

Taylor, M. A., I. L. Hendy, and D. K. Pak (2014), Deglacial ocean warming and marine margin retreat of the Cordilleran Ice Sheet in the North Pacific Ocean, *Earth and Planetary Science Letters*, *403*, 89-98.

Thomson, R. E., and M. V. Krassovski (2010), Poleward reach of the California Undercurrent extension, *Journal of Geophysical Research*, *115*(C9), C09027.

Timmermann, A., F. Justino, F. F. Jin, U. Krebs, and H. Goosse (2004), Surface temperature control in the North and tropical Pacific during the last glacial maximum, *Climate Dynamics*, *23*(3-4).

Waelbroeck, C., L. Labeyrie, E. Michel, J. C. Duplessy, J. F. McManus, K. Lambeck, E. Balbon, and M. Labracherie (2002), Sea-level and deep water temperature changes derived from benthic foraminifera isotopic records, *Quaternary Science Reviews*, *21*, 295-305.

Zhang, R., and T. L. Delworth (2005), Simulated tropical response to a substantial weakening of the Atlantic thermohaline circulation, *Journal of Climate*, *18*, 1853-1860.

Chapter 4

High concentrations of potentially bioavailable iron on Arctic sea ice particles

Abstract

High spring primary productivity has been documented in association with relatively high nitrate concentrations on the extensive Arctic continental shelf as sea ice thickness and extent has declined (Arrigo et al., 2012). Simultaneously sea ice contributes the micronutrient iron to surface ocean waters during the early spring melt especially in coastal regions. Nitrate (NO^-_3) concentrations are projected to increase in the shallow Arctic Ocean shelf regions as winds and upwelling are enhanced on a warmer planet. As Fe is required by primary producers to assimilate NO^-_3, it may become an important co-limiting factor for algal blooms under sea ice during early spring. Elemental concentrations are presented from sea ice cores collected from shallow coastal regions in the Beaufort/Chukchi Sea and the Canadian Arctic. We report high proportions of labile Fe (~75%) within particulate Fe (pFe) concentrations. As the majority of pFe in sea ice is labile and therefore potentially bioavailable, it constitutes a significant flux to the surface ocean during spring sea ice melt. Elemental ordination suggests the source of bioavailable pFe may be Fe-Mn crusts associated with clays either from atmospheric dust or resuspended continental shelf sediments. A warmer Arctic Ocean, and associated decline in sea ice extent, may provide less bioavailable Fe during the spring algal bloom.

1. Introduction

Iron cycling within Arctic sea ice is not yet well characterized, and the few observations report large spatial heterogeneity of iron (Fe) concentrations (Aguilar-Islas et al., 2008; Tovar-Sánchez et al., 2010; van der Merwe et al., 2011). The seasonal flux of Fe and other bio-essential trace metals in the Arctic Ocean are strongly linked with sea ice sediments, where sea ice aggregates a reservoir of potentially bioavailable Fe to be released in surface waters during spring melt season. The relative importance of sediment sources to sea ice may depend on location and thickness of the ice. Filterable Fe (defined as the sum of soluble, nanoparticulate, and colloidal Fe, <0.2 μm) can be enriched in sea ice by entrainment of particulate detrital and living organic matter that may be degraded into dissolved Fe, and may also be transferred from seawater to bottom layers of sea ice via uptake by sea ice algae (Wang et al., 2014). Particulate Fe (pFe) is delivered to sea ice through dry and wet atmospheric deposition of dust (Tovar-Sánchez et al., 2010) – this deposition is assumed to be especially important in open ocean sites, further from terrestrial sediment sources and dominated by multi-year ice (MYI). In coastal and shelf environments where annual sea ice formation occurs, labile Fe is assumed to derive from glacial melt (Bhatia et al., 2013; Hawkings et al., 2014; Werhmann et al., 2014), sediments resuspended in shallow shelf waters and river runoff (Klunder et al. 2012). Biogenic pFe may be incorporated during sea ice formation, and/or via algae inhabiting the bottom layers of floating sea ice (Deal et al., 2011; Planquette et al., 2013).

Direct measurements of Arctic sea ice sediment trace metal geochemistry and bioavailability are rare, but crucial to understanding the role of sea ice in Arctic marine productivity. Here we present major and trace element concentrations from particles in multiple size fractions within sea ice profiles, offshore from Point Barrow, AK (PB) and in the Canadian Arctic (CAA) between Bathurst and Ellef Rignes Islands, to improve understanding of the role

that Arctic sea ice plays in Fe cycling (Figure 1). Particulate Fe bioavailability was estimated from sea ice sediments using sequential chemical leaches. Potential oceanic and atmospheric sources of bioavailable Fe are suggested based on the elemental ordination from principle component analysis with the relative contribution of atmospheric dust constrained with a global aerosol simulations conducted with the Community Earth System Model (CESM).

2. Methods

2.1 Sample Collection

Samples for total dissolved and particulate metals analysis were collected in first year fast ice (Point Barrow Far Shore (PB FS), 71˚ 24.169169' N, 156˚ 21.402402' W, ~4 km from shore, core length 106 cm; Point Barrow Near Shore (PB NS), 71˚ 22.885885' N, 156˚ 30.637637' W, and ~1 km from shore, core length 153 cm) near Barrow, Alaska in March-April 2014. Pack ice (Canadian Arctic Archipelago First Year Ice (CAA FYI), 77˚ 21.887 N, 99˚ 9.471 W, core length 175 cm; and multiyear ice cores Canadian Arctic Archipelago Multi-year Ice (CAA MYI), 77˚ 20.337 N, 99˚ 56.082 W, core length 242 cm, were collected ~50 km offshore from Ellef Ringnes Island in the Norwegian Bay) north of Resolute Bay, Canada in April 2014. Snow was sampled in polyethylene (PE) containers that had been acid washed and rinsed 3 x with ultra high purity water (UHP; 18.2 MΩ DI water). Ice cores were drilled and then decontaminated in the field. Cores were sectioned and decontaminated at the field sampling sites. To decontaminate ice, 10 cm of ice was removed from the ice core surface on all sides using 10% HNO_3 rinsed titanium chisels. Sections were placed in acid cleaned PE containers and melted at ambient temperature before processing. Seawater was sampled directly from the coring sites PB NS and CAA MYI into a 1 L acid cleaned LDPE Nalgene bottle. All ice, snow, and seawater samples were filtered using a peristaltic pump using acid washed savillex filtration unit in a glove bag in the field.

Filtrate was collected in acid washed LDPE Nalgene bottles. The residue were collected onto acid cleaned (sequentially in HCl, HNO3, HF + HNO3 for 5 days, rinsed 5 X in SDIS water, and stored in acid cleaned centrifuge tubes in SDIS) hydrophobic polytetrafluoroethylene (PTFE) filters (0.2µm, 5µm, 10µm, >30µm pore sizes) and stored in pre-cleaned centrifuge containers in UHP. Filtered sample volumes ranged from 500 to 1000 mL depending on the sample.

2.2 Sample Analysis

The labile particulate leach procedure followed Berger et al. (2008). Filters were transferred from centrifuge containers to 180 mL acid-cleaned FEP beakers. Filters were heated in solution (25% acetic acid and 0.02 M hydroxylamine hydrochloride) on hot plates at ~95˚C for 10 minutes, and then cooled to room temperature for 2 hours. Leachate was removed to acid cleaned beakers and dried down. Limitations of sample size prevented more than 2 successive leaches-separating acetic acid + hydroxylamine leachable from total Fe. The labile Fe leach extracts both crystalline and amorphous Fe (Berger et al., 2008) therefore we report both crystalline and amorphous Fe-oxide phases. As low as 50% of the amorphous Fe leached is estimated to be bioavailable and can be taken up by phytoplankton in culture experiments (Sunda, 2001). Crystalline Fe is more aged and therefore less bioavailable, so the potentially bioavailable Fe pool reported here is an approximation.

All filters were rinsed with UHP water after the leach procedure and then digested with sequential acid additions and then dry downs as follows: 4 mL of concentrated HNO_3 + 0.5 mL of HF were added to the filters in 180 mL FEP beakers and heated for for 3 days. Samples were dried down and redigested in 1 mL aqua regia and heated overnight. Samples were then dried down and rinsed with 1 mL 6 M HCl, the filters were discarded and the remaining solution was

heated overnight. Samples were dried down, and then digested in 2.5 N HNO_3, where an aliquot of 10% concentration by weight was used for ICP-MS analysis.

We report data for 16 element concentrations measured from the digested particulate samples (refractory and leachable) (Al, Ti, Si, Fe, Cu, Mn, Co, Mo, Ni, Zn, Ca, K, Cr, Mg, Cd, P). Some elements were measured using a Thermo-Finnigan Element2 high resolution ICP-MS at the University of Michigan (Si, Ca, K, P), and the rest were determined on a Thermo-Finnigan Element2 high resolution ICPSF-MS at The Ohio State University by using an apex Q desolvant nebulizer as introduction system to increase sensitivity and reduce spectroscopic interferences (Uglietti et al., 2014). Field blanks were processed and filtered using the savillex filtration system the samples in the field. Field blanks consisted of UHP water brought from the University of Michigan. Blanks that were greater than the limit of detection were subtracted from the measurements (Table S4). Instrumental precision was determined by calculating the relative standard deviation of the element concentration from multiple replicate sample analysis and varied from less than 2% for Si, P, K, and Ca, and from 2-5% for Fe, Cu, Mn, Co, Mo, Ni, Zn, Cr, and Cd. Relative 1σ uncertainties were less than 10% for Al and Mg, and less than 20% for Ti.

Filtered samples were acidified with HNO_3 to pH 2.5 for one month. Depending on salinity, samples were diluted for major element determination. Samples were analyzed using a Thermo-Finnigan Element2 high resolution ICP-MS at the University of Michigan.

Particle size samples were collected at the CAA sites (MYI and FYI) from subsamples of cores. Samples were collected in acid cleaned vials and kept frozen until analysis at Milano-Bicocca University. Analyses of dust size and concentration (number and volume) were

performed at the University of Milano-Bicocca using a Beckman Coulter-Multisizer™ 3 Coulter Counter®, following Albani et al., 2012. The size range of measurements is 1–30 µm.

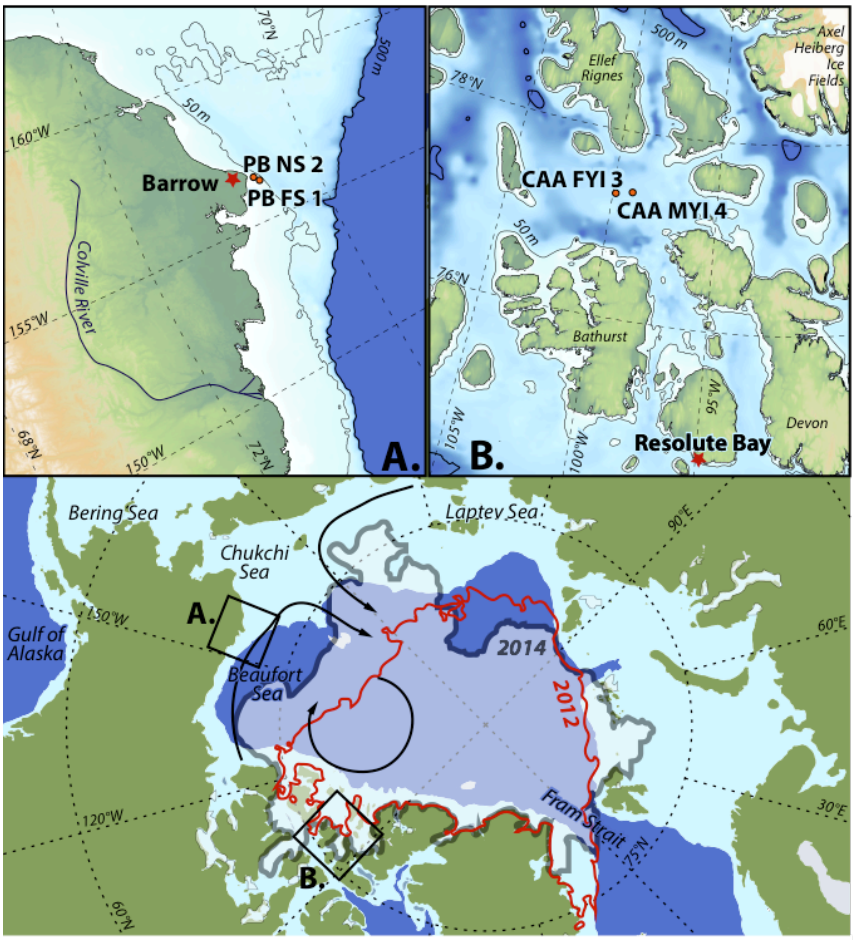

Figure 4.1
Sampling locations within the Arctic. Black boxes represent map inserts of A) first year fast ice core sites (orange circles) offshore of Point Barrow, AK (PB FS 1, 71˚ 24.169 N, 156˚ 21.402 W, ~4 km from shore, core length 106 cm; PB NS 2, 71˚ 22.885 N, 156˚ 30.637 W, ~1 km from shore, core length 153 cm); B) pack ice core sites (orange circles) in the Canadian Arctic Archipelago (CAA FYI 3, 77˚ 21.887 N, 99˚ 9.471 W, core length 175 cm; CAA MYI 4, 77˚ 20.337 N, 99˚ 56.082 W, core length 242 cm, both cores are ~50 km offshore from Ellef Ringnes Island in the Norwegian Bay). 2012 minimum ice extent is shown by a red line, while 2014 is shown by a thick grey line and transparent white shading. Black arrows represent generalized multiyear sea ice circulation. Dark blue shading represents sea floor >500m water depth.

Modeling

Dust mixing ratios in snow and sea ice are simulated using the Community Earth System Model version 1.1.1 (CESM1) with the Bulk Aerosol Model (BAM), which simulates dust in

four size bins. We run CESM fully coupled with all active components and present day radiative forcing (B_2000 compset) for 11 years. We include the final ten years of output in our analysis to allow for temporal averaging with one year of spin-up to allow aerosol fluxes to equilibrate. To calculate monthly mean dust mixing ratios, we take area-weighted means from the nine nearest oceanic gridcells to each location of interest. Values presented here thus represent spatially and temporally averaged monthly dust mixing ratios within snow and sea ice prognosed by the Community Ice Code (CICE) component of CESM.

3. Results and Discussion

3.1 Sediment characterization and provenance

There have been few measurements made characterizing Fe concentrations within Arctic sea ice sediments (Figure 4.2). Sedimentary Fe can be partitioned into particulate (pFe) size fractions (>0.2 μm) and filterable phases (<0.2 μm consisting of the sum of nanoparticulate, colloidal, and soluble Fe) (Cullen et al., 2006; Raiswell and Canfield, 2012). In this study, pFe concentrations were orders of magnitude higher than filterable Fe concentrations, and high relative to other Arctic sea ice studies (Figure 4.2). Sea ice was significantly enriched in filterable Fe relative to seawater at the PB sites but not at the CAA sites (Figure 4.3). Filterable Fe in sea ice can be affected by many processes including biological uptake from seawater by sea ice algae within the lower layers of sea ice or as detrital or living organisms are degraded by heterotrophic processes within the ice (Lannuzel et al., 2011). While concentrations of non bioessential elements in filterable sea ice samples (K, Mg, Mo) were linearly related with Na concentrations (as a proxy for bulk sea ice salinity) bioessential trace metals like filterable Fe in sea ice samples at both sites were non-linear when plotted against Na concentrations. This

deviation from bulk sea ice salinity is suggestive of some bioactive cycling of filterable Fe within sea ice at these sites (Figure 4.3).

Sediment grain size distributions characterized at the CAA core sites indicate sediments from the first year pack ice (FYI) and the multi year ice (MYI) were dominated by grain sizes between 10-30 μm (Figure 4.4). Larger pFe size fractions (>20 μm) tend to be dominated by lithogenic input (Frew et al., 2006), and a relatively high proportion of total pFe (50-95%) are within the >10 μm grain size fractions in this study (Figure 4.5). Principle component analyses of sediments in the particulate size fractions (>0.2 μm) and filterable size fractions (<0.2 μm) identify two main factors: elements (Fe, Cu, Mn, Mo, Co and Ni) associated with Fe-, Mn-oxyhydroxides and elements (P, Ca, Si, K, Mg, and Ti) associated with clays (Figure 4.6), supporting a predominately lithogenic origin. However, a biogenic Fe source component cannot be ruled out, as samples with high biogenic pFe can still contain < 68% lithogenic Fe, potentially obscuring the presence of biogenic pFe (Frew et al., 2006).

Assuming a dominant lithogenic sediment source, atmospheric dust deposition, riverine/melt water run off, or coastal upwelled shelf sediments can all enrich sea ice with sediments (Wang et al., 2014). Results presented here cannot distinguish between these sources as significant overlap in atmospheric dust (0.1 to 10 μm) and shelf sediment grain sizes (0.2 to >30 μm), and trace metal abundance patterns common to Fe-Mn crusts occur in both sediment types (Thiagarajan and Lee, 2004; Mahowald et al., 2011; Planquette et al., 2013). However, CESM simulated dust concentrations in sea-ice suggest that although dust is unlikely to be a dominant sediment source in nearshore FYI, it may contribute significantly to offshore MYI. In the CAA sites, the CESM simulates a mean April total dust concentration of 6.0 ppb (+/- 2.5 ppb) in sea-ice, potentially accounting for 10% of the sediments in the CAA pack ice (754 ppb),

and up to 55% of sediments in the MYI (151 ppb) (Figure 4.7). Consistent with the potential for atmospheric Fe deposition, Fe concentrations are higher in snow at the CAA sites than in seawater (Figure 4.2). Modeled dust accumulation peaks in the summer at PB, when FYI extent is limited or absent, and concentrations are low during winter months (~ 3 ppb), indicating that atmospheric dust input is insignificant at the site (Figure 4.7).

Where sea ice formation extends onto the continental shelf at water depths < 50 m, sediments are commonly incorporated in sea ice by suspension freezing. Resuspended seafloor sediment (wave and tidal activity, currents or wind-driven upwelling) is lifted to the ice-free ocean surface by ice crystals forming at depth (Darby et al, 2011). Potential sources of seafloor sediment at PB include the suspended load of May-June Colville River runoff and other smaller rivers (Reimnitz, 2002). Located over deeper water, sea ice containing resuspended bottom sediment can only be advected to the CAA core sites, however ice rafted glacial sediments from the tidewater glaciers on nearby Axel Heiberg and Ellesmere Islands are another potential advected source.

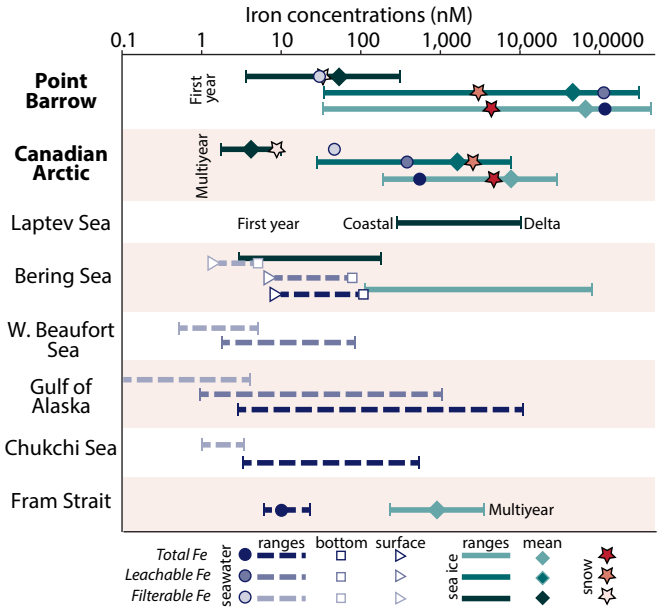

Figure 4.2
Total, leachable, and filterable iron concentrations (nM) in sea ice (ranges in solid lines, averages as diamonds), snow (averages as stars) and seawater (ranges in dashed lines, averages as circles, surface water as triangles, bottom water as squares) for Point Barrow and the Canadian Arctic are compared on a log scale to the Laptev sea (Hölemann et al., 1999), Bering Sea (Aguilar-Islas et al., 2008; Hurst et al., 2010), West Beaufort Sea (Aguilar-Islas et al., 2013), Gulf of Alaska (Lippiatt et al., 2010), Chukchi Sea (Nakayama et al., 2011), and Fram Strait (Tover- Sánchez et al., 2010).

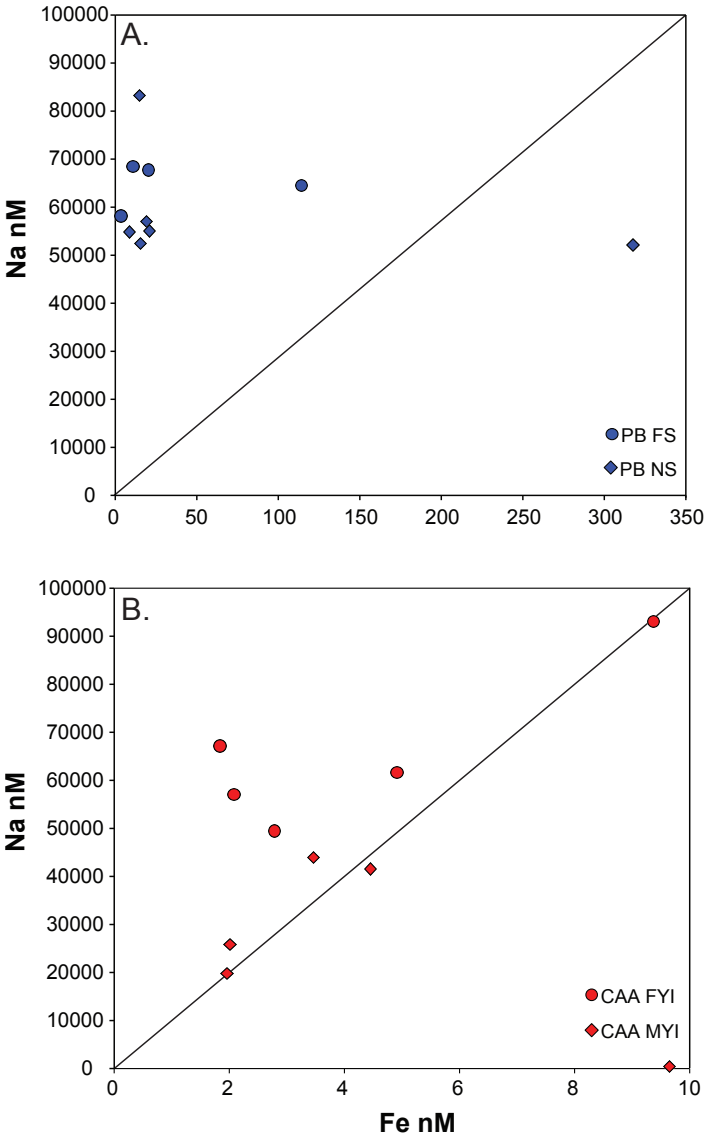

Figure 4.3
Filterable Fe (<0.2 µm) plotted against filterable Na concentrations for CAA cores (A) and Point Barrow, AK, cores (B). 1:1 line is drawn in for reference in both plots.

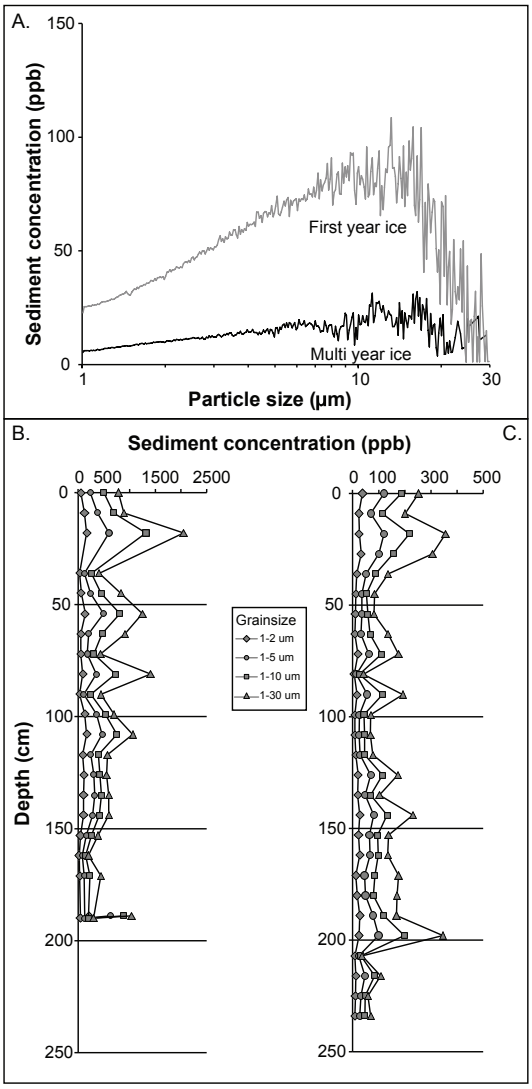

Figure 4.4
Concentration (ppb) of insoluble particles (A) from the Canadian Arctic cores CAA FYI (gray line, first year ice) and CAA MYI (black line, multiyear ice) versus sediment particle sizes (µm). Profiles of sea ice core sediment concentrations (ppb) with depth for Canadian Arctic core sites CAA FYI (B) and CAA MYI (C) for different grain sizes (1-30 µm).

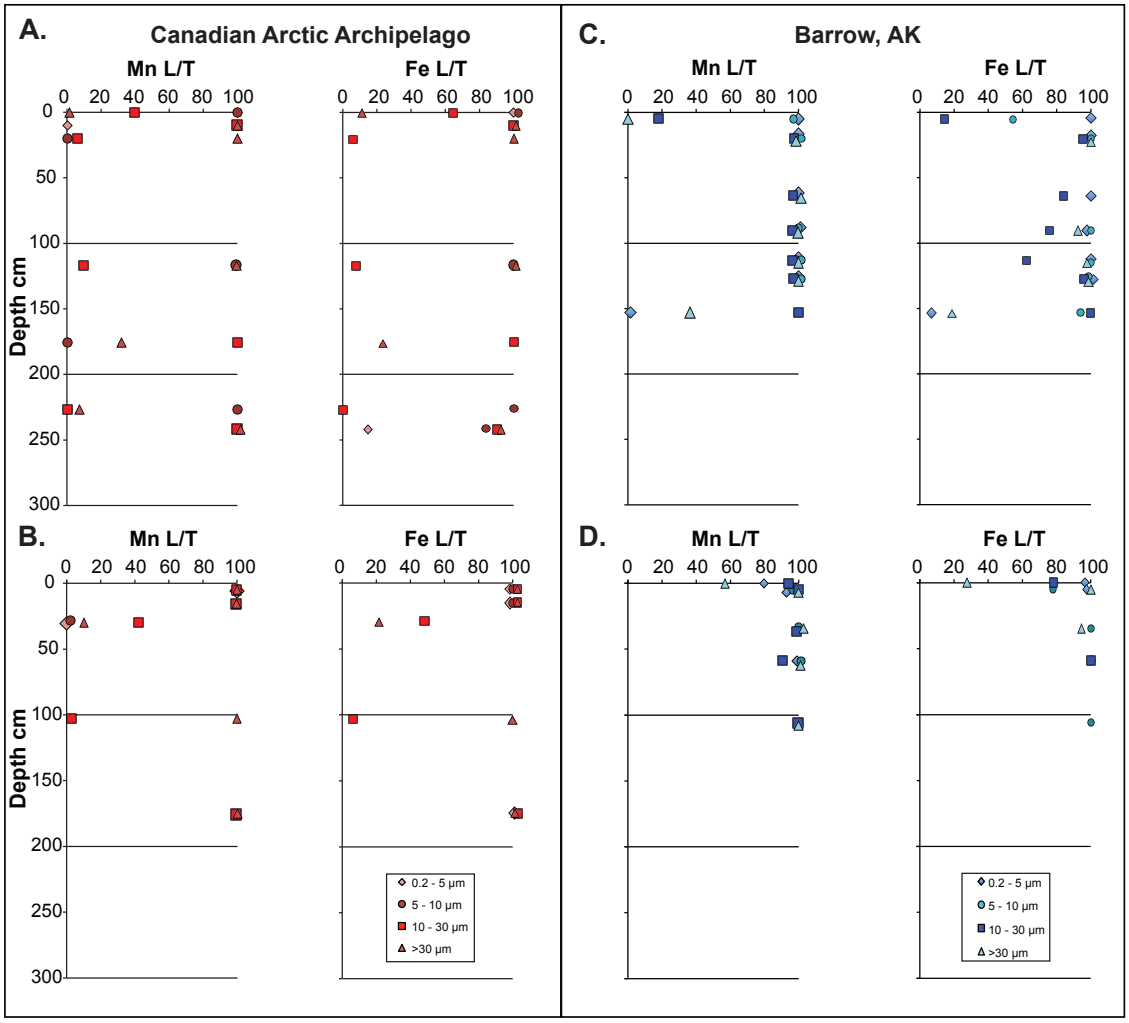

Figure 4.5
Labile to total Mn and Fe ratios in cores CAA MYI (A), CAA FYI (B) in the CAA (red), and in cores PB NS (C) and PB FS (D) at Point Barrow, AK (blue), plotted against core depths. Sediments are plotted by grain size from 0.2 to 5 µm (diamond symbol), 5 to 10 µm (circle symbol), 10 to 30 µm (square symbol) and >30µm (triangle symbol).

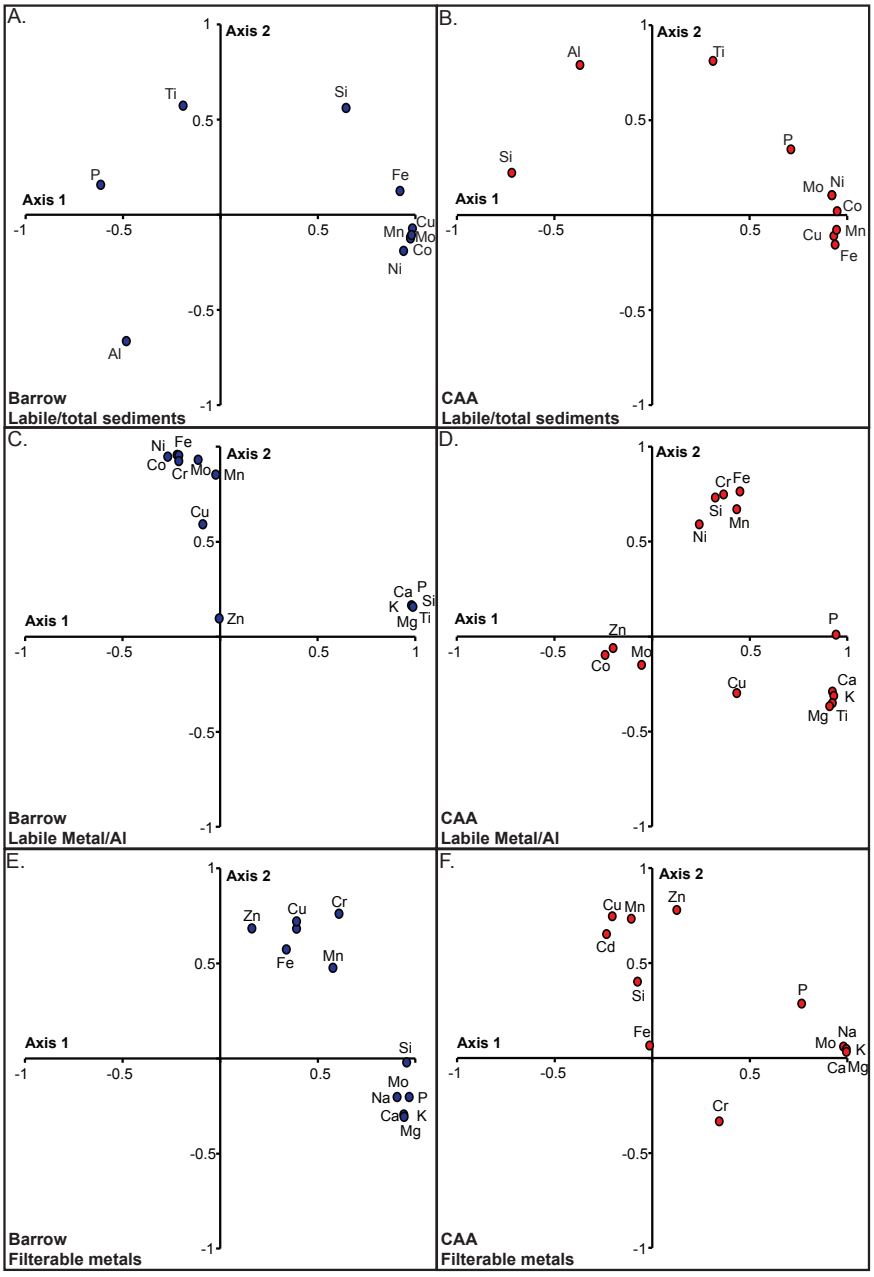

Figure 4.6
Panels show principle component analysis results for 1 and 2 axes for ratios of labile to total metals for all Barrow (A) and Canadian Arctic (B) cores, labile metals normalized to Al for all Barrow (C) and Canadian Arctic (D) cores, and filterable metals all Barrow (E) and Canadian Arctic (F) cores. Coefficients of variance are reported in Tables S1, S2, and S3.

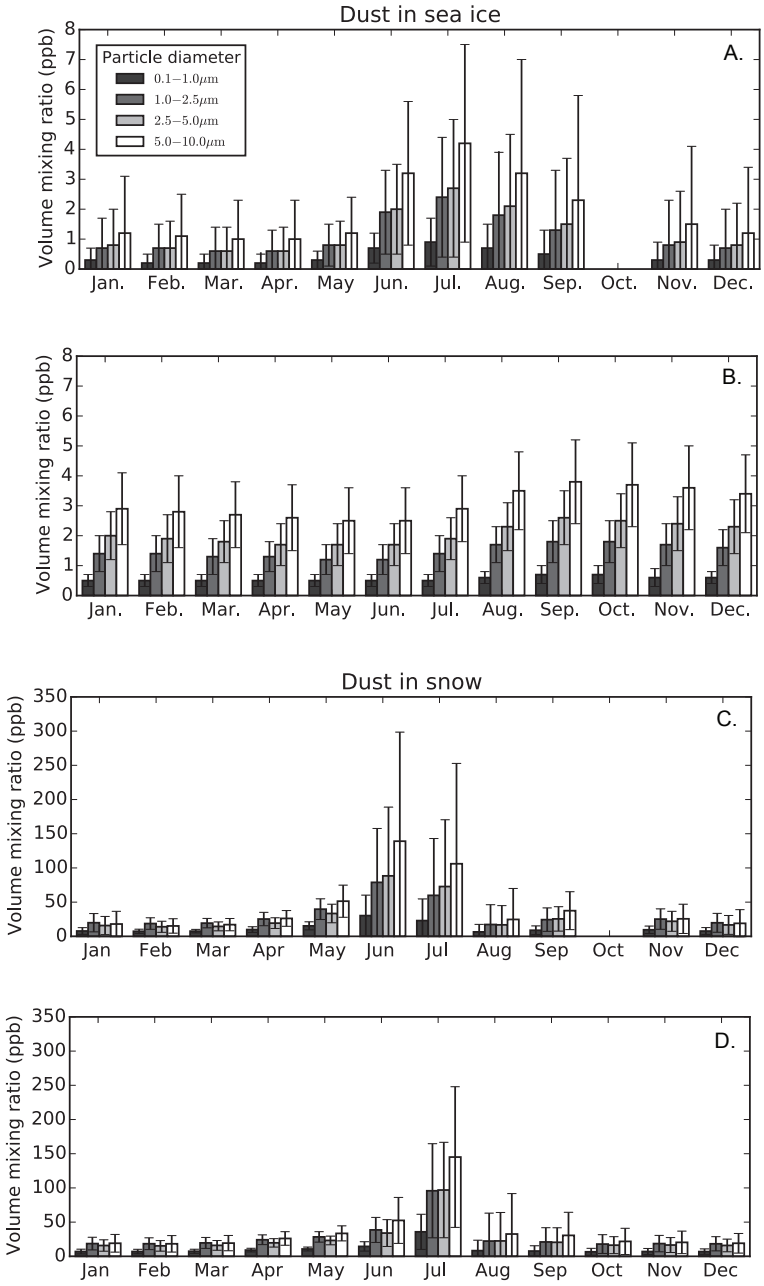

Figure 4.7
CESM –simulated dust concentration in Barrow, AK sea ice (A) and the Canadian Arctic (B) plotted by month and binned by particle diameter (black, 0.1-1.0 μm; dark gray, 1.0-2.5 μm; light gray, 2.5-5.0 μm; white, 5.0-10.0 μm). Simulated dust concentrations in snow at Barrow, AK (C) and the Canadian Arctic (D) plotted by month and binned by particle diameter (black, 0.1-1.0 μm; dark gray, 1.0-2.5 μm; light gray, 2.5-5.0 μm; white, 5.0-10.0 μm).

3.2 Bioavailability

Sediment composition impacts biogeochemical cycling as biogenic pFe is more readily available for uptake by phytoplankton than lithogenic pFe (Frew et al., 2006; Lannuzel et al., 2014). Furthermore, the lability of lithogenic pFe is dependent on grain size, mineralogy, and surface reactivity of Fe-oxyhydroxide species, which depends on crystal structure, related to aging of coatings, and temperature (Poulton and Raiswell, 2005; Sugie et al., 2013). Sea ice at both sites was found to have elevated labile Fe concentrations, ranging from ~32 to 218,000 nmol L^{-1}, or approximately 75% of the total pFe (Figure 4.8). The Barrow cores average 77% and 89% pFe lability, while in the CAA, FYI averages 75%, with MYI containing the least labile pFe (54% the pFe). Lability of pFe relative to total decreases with increasing particle size (Figure 4.5). The highest percent labile pFe in Barrow cores is found in the 0.2 μm size fraction. The pool of labile Fe within sea ice on the shallow continental shelf at CAA and PB is high relative to bioavailable pFe measured from shelf sediments and seawater in other regions (Figure 4.2), suggesting that both FYI and MYI may represent a significant source of bioavailable Fe during spring melt season when algal productivity is highest (Deal et al., 2011). For example, labile pFe measured in seawater in the Gulf of Alaska was found to make up to 32% of the total pFe, which ranged from 2.7 to 10,500 nmol L^{-1} (Lippiatt et al., 2010), while in the coastal Bering Sea, measurements of pFe in shelf sediments yielded total pFe concentrations of up to 312 nmol L^{-1}, 80% of which was considered labile (Hurst et al., 2010). In Spitzbergen highly reducible Fe and Mn oxides generated from benthic recycling of dissolved Fe in sediments were found released into fjord bottom waters providing another source of bioavailable Fe (Wehrmann et al., 2014).

Principle component analyses were conducted to determine elemental associations to constrain the major sources of pFe as the samples were too small to allow for mineral identification. Three analyses are presented: ratios of labile to total elemental concentrations

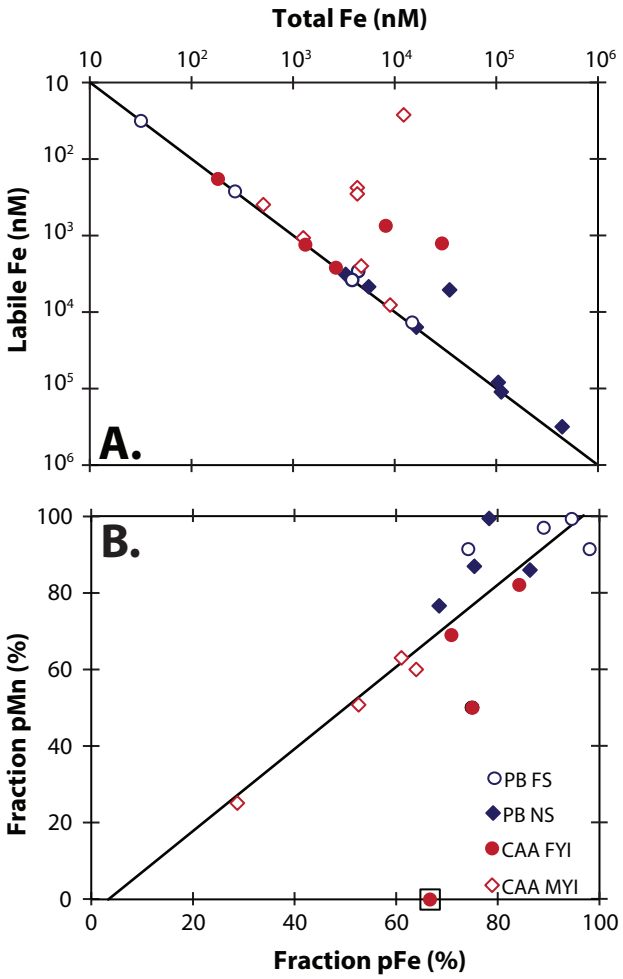

Figure 4.8
Labile versus total Fe (A) plotted on a logarithmic scale from Barrow core samples (blue) and Canadian Arctic core samples (red), with a 1:1 line. Regression of percent particulate labile Mn and Fe (B) from Barrow core samples (blue) and Canadian Arctic core samples (red). Outlier not included in regression is enclosed in a box.

(Figure 4.6; Table 4.1), labile elemental concentrations normalized to labile Al concentrations (Figure 4.6; Table 4.2), and filterable metals (Figure 4.6; Table 4.3). PCA results of all analyses indicate that elements associated with Fe-, Mn- oxyhydroxides (Fe, Cu, Mn, Mo, Co and Ni) are grouped separately from elements associated with clays. (P, Ca, Si, K, Mg, and Ti). Composition based upon PCA results suggest the sea ice sediments consist of clay minerals coated with Fe-oxides. Small spheres of Fe oxides (10-20 nm) can be adsorbed onto the edges of clay minerals

(Poulton and Raiswell, 2005), where labile Fe is concentrated in the finer grain size fractions dominated by clays.

Generally smaller size fractions are considered more bioavailable. Mechanically weathered glacial flours from the European Alps, southwest Greenland, and Signy Island in Antarctica found the greatest concentrations of bioavailable ferrihydrite in finer grain size fractions (<63 μm; Hopwood et al., 2014). However, here sea ice samples with a relatively low fraction of labile pFe do not appear to be associated with changes in either size fraction or elemental associations. The CAA samples generally have lower labile pFe fractions, perhaps reflecting differences in the sediment source and/or degree of aging of Fe-Mn oxyhydroxides such that they are more crystalline and therefore less bioavailable (Figure 4.5).

Perhaps the environmental conditions of Fe-Mn oxyhydroxides coated grains encapsulated within sea ice play a role in the high lability of pFe. The bioavailability of lithogenic pFe in seawater can be enhanced by photochemical reduction or by biological processing (eg: ingestion of colloidal ferrihydrite by phagotrophic protists) (Borer et al., 2009). Finer grain size fractions have a longer residence time in the surface waters enabling chemical transformations that enhance bioavailability (Frew et al., 2006; Lannuzel et al., 2014).

It is not known how primary producers access pFe in this form, but recently Fe isotopes used as a tracer in the South Pacific Ocean demonstrated that a fraction of lithogenic pFe (>0.2 μm) was processed into dissolved Fe and utilized by phytoplankton during a spring algae bloom (Ellwood et al., 2015). Mesocosm experiments also showed that 60-80% of Fe bound to the surface of particulates of various size fractions (0.2 to 2, 2 to 20, >20 μm) was removed by phytoplankton uptake (Ellwood et al., 2015), suggesting that surface-bound pFe may be an important source of bioavailable iron.

This study indicates that under current conditions significant concentrations of labile pFe in FYI and MYI are potentially available allowing phytoplankton to live in an Fe replete habitat during spring melt. Increased NO^-_3 availability projections in coastal, shallow upwelling zones (Tremblay et al., 2011), may not affect primary productivity in the short term as long as seasonal sea ice releases this labile pFe when there is light availability. These trends may be counteracted in a warming Arctic (Perovich and Richter-Menge, 2009) as maximum ice extent decreases and sea ice melts earlier in the year and more rapidly such that (1) primary producers are unable to take advantage of surface ocean nutrient enrichments when light availability is high (2) sea ice formation no longer occurs in regions where freeze up incorporates resuspended shelf sediments, and (3) the flux of potentially bioavailable pFe from sea ice decreases as the sea ice "reservoir" decreases.

Table 4.1
Principle component axes for labile/total elemental data from cores CAA FYI and CAA MYI at CAA, and cores PB FS and PB NS from Point Barrow, AK.

Labile/Total	**Canadian Arctic**		**Point Barrow, AK**	
Variability explained	**Axis 1 69.4**	**Axis 2 16.7**	**Axis 1 66.2**	**Axis 2 12.1**
Elemental coefficients				
Al	-0.38	0.83	-0.48	-0.66
Co	0.98	0.03	0.98	-0.12
Cu	0.96	-0.10	0.99	-0.07
Fe	0.97	-0.15	0.92	0.13
Mn	0.98	-0.07	0.98	-0.11
Mo	0.95	0.12	0.98	-0.12
Ni	0.95	0.12	0.94	-0.19
P	0.74	0.37	-0.62	0.16
Si	-0.74	0.24	0.64	0.56
Ti	0.32	0.85	-0.19	0.57

Table 4.2
Principle component axes for labile metal/Al data from cores CAA FYI and CAA MYI at CAA, and cores PB FS and PB NS from Point Barrow, AK.

Labile Me/Al	**Canadian Arctic**		**Point Barrow, AK**	
Variability explained	**Axis 1 37.6**	**Axis 2 21.7**	**Axis 1 43.2**	**Axis 2 34.6**
Elemental coefficients				
Ca	0.93	-0.29	0.99	0.16
Co	-0.24	-0.10	-0.21	0.92
Cr	0.32	0.73	-0.22	0.96
Cu	0.43	-0.30	-0.09	0.59
Fe	0.45	0.77	-0.27	0.95
K	0.93	-0.31	0.99	0.16
Mg	0.91	-0.37	0.99	0.16
Mn	0.43	0.67	-0.02	0.85
Mo	-0.05	-0.15	-0.11	0.15
Ni	0.24	0.59	-0.21	0.95
P	0.94	0.01	0.98	0.17
Si	0.37	0.75	0.98	0.17
Ti	0.92	-0.35	0.99	0.16
Zn	-0.20	-0.06	-0.01	0.10

Table 4.3
Principle component axes for filterable (<0.2 μm) elemental data from cores CAA FYI and CAA MYI at CAA, and cores PB FS and PB NS from Point Barrow, AK.

Filterable	**Canadian Arctic**		**Point Barrow, AK**	
Variability explained	**Axis 1 44.1**	**Axis 2 19.2**	**Axis 1 56.7**	**Axis 2 23.0**
Elemental coefficients				
Ca	0.99	0.04	0.94	-0.31
Cd	-0.24	0.65	0.39	0.68
Cr	0.34	-0.33	0.61	0.75
Cu	-0.21	0.75	0.39	0.71
Fe	-0.01	0.07	0.34	0.57
K	0.99	0.05	0.94	-0.31
Mg	0.99	0.03	0.94	-0.31
Mn	-0.11	0.73	0.58	0.47
Mo	0.98	0.07	0.97	-0.21
Na	0.99	0.03	0.94	-0.30
P	0.77	0.29	0.91	-0.21
Si	-0.08	0.40	0.96	-0.03
Zn	0.13	0.78	0.16	0.68

References

Aguilar-Islas, A. M., R. D. Rember, C. W. Mordy, and J. Wu (2008), Sea ice-derived dissolved iron and its potential influence on the spring algal bloom in the Bering Sea, *Geophysical Research Letters*, *35*(24), L24601.

Aguilar-Islas, A. M., R. Rember, S. Nishino, T. Kikuchi, and T. Ito (2013), Partitioning and lateral transport of iron to the Canada Basin, *Polar Science*, *7*(2), 82-99.

Albani, S., Delmonte, B., Maggi, V., Baroni, C., Petit, J.-R., Stenni, B., Mazzola, C., Frezzotti, M. (2012), Interpreting last glacial to Holocene dust changes at Talos Dome (East Antarctica): implications for atmospheric variations from regional to hemispheric scales. *Climate of the Past, 8,* 741–750.

Arrigo, K. R., et al. (2012), Massive Phytoplankton Blooms Under Arctic Sea Ice, *Science*, *336*(6087), 1408-1408.

Berger, C. J. M., S. M. Lippiatt, M. G. Lawrence, and K. W. Bruland (2008), Application of a chemical leach technique for estimating labile particulate aluminum, iron, and manganese in the Columbia River plume and coastal waters off Oregon and Washington, *Journal of Geophysical Research*, *113*, C00B01.

Bhatia, M. P., E. B. Kujawinski, S. B. Das, C. F. Breier, P. B. Henderson, and M. A. Charette (2013), Greenland meltwater as a significant and potentially bioavailable source of iron to the ocean, *Nature Geoscience*, *6*(4), 274-278.

Borer, P., B. Sulzberger, S. J. Hug, S. M. Kraemer, and R. Kretzschmar (2009), Photoreductive dissolution of iron(III) (hydr)oxides in the absence and presence of organic ligands: Experimental studies and kinetic modeling, *Environmental Science & Technology*, *43*(6), 1864-1870.

Cullen, J. T., B. A. Bergquist, and J. W. Moffett (2006), Thermodynamic characterization of the partitioning of iron between soluble and colloidal species in the Atlantic Ocean, *Marine Chemistry*, *98*(2-4), 295-303.

Darby, D. A., W. B. Myers, M. Jakobsson, and I. Rigor (2011), Modern dirty sea ice characteristics and sources: The role of anchor ice, *Journal of Geophysical Research*, *116*(C9), C09008–18.

Deal, C., M. Jin, S. Elliott, E. Hunke, M. Maltrud, and N. Jeffery (2011), Large-scale modeling of primary production and ice algal biomass within arctic sea ice in 1992, *Journal of Geophysical Research*, *116*(C7), C07004.

Delmonte, B., P. S. Andersson, M. Hansson, H. Schöberg, J. R. Petit, I. Basile-Doelsch, and V. Maggi (2008), Aeolian dust in East Antarctica (EPICA-Dome C and Vostok):

Provenance during glacial ages over the last 800 kyr, *Geophysical Research Letters*, *35*(7), L07703.

Ellwood, M. J., D. A. Hutchins, M. C. Lohan, A. Milne, P. Nasemann, S. D. Nodder, S. G. Sander, R. Strzepek, S. W. Wilhelm, and P. W. Boyd (2015), Iron stable isotopes track pelagic iron cycling during a subtropical phytoplankton bloom, *Proceedings of the National Academy of Sciences*, *112*(1), E15-E20.

Frew, R. D., D. A. Hutchins, S. Nodder, S. Sanudo-Wilhelmy, A. Tovar-Sanchez, K. Leblanc, C. E. Hare, and B. P. W (2006), Particulate iron dynamics during FeCycle in subantarctic waters southeast of New Zealand, *Global Biogeochemical Cycles*, *20*(1), GB1S93.

Hawkings, J. R., M. Tranter, R. Raiswell, L. G. Benning, P. J. Statham, A. Tedstone, P. Nienow, K. Lee, J. Telling, and J. L. Wadham (2014), Ice sheets as a significant source of highly reactive nanoparticulate iron to the oceans, *Nature Communications*, *5*, 1-8.

Hölemann, J. A., M. Schirmacher, and A. Prange (1999), Dissolved and particulate major and trace elements in newly formed ice from the Laptev Sea (Transdrift III, October 1995), in Land-Ocean Systems in the Siberian Arctic: Dynamics and History, edited by H. Kassens et al., pp. 101-111, Springer, Berlin.

Hopwood, M. J., P. J. Statham, M. Tranter, and J. L. Wadham (2014), Glacial flours as a potential source of Fe(II) and Fe(III) to polar waters, *Biogeochemistry*, *118*(1-3), 443-452.

Hurst, M. P., A. M. Aguilar-Islas, and K. W. Bruland (2010), Iron in the southeastern Bering Sea Elevated leachable particulate Fe in shelf bottom waters as an important source for surface waters, *Continental Shelf Research*, *30*(5), 467-480.

Klunder, M. B., D. Bauch, P. Laan, H. J. W. de Baar, S. van Heuven, and S. Ober (2012), Dissolved iron in the Arctic shelf seas and surface waters of the central Arctic Ocean: Impact of Arctic river water and ice-melt, *Journal of Geophysical Research*, *117*(C1), C01027–18.

Lannuzel, D., E. B. Roark, A. R. Bowie, K. G. Cannriato, P. C. van der Merwe, B. L. Ingram, A. T. Townsend, R. Tada, V. Schoemann (2011), Distribution of dissolved and particulate metals in Antarctic sea ice, *Marine Chemistry 124*, 134–146.

Lannuzel, D., P. C. van der Merwe, A. T. Townsend, and A. R. Bowie (2014), Size fractionation of iron, manganese and aluminium in Antarctic fast ice reveals a lithogenic origin and low iron solubility, *Marine Chemistry*, *161*(C), 47-56.

Lippiatt, S. M., M. C. Lohan, and K. W. Bruland (2010), The distribution of reactive iron in northern Gulf of Alaska coastal waters, *Marine Chemistry*, *121*(1-4), 187-199.

Mahowald, N., D. S. Ward, S. Kloster, M. G. Flanner, C. L. Heald, N. G. Heavens, P. G. Hess,

J.-F. Lamarque, and P. Y. Chuang (2011), Aerosol Impacts on Climate and Biogeochemistry, *Annual Review of Environment and Resources*, *36*(1), 45-74.

Nakayama, Y., S. Fujita, K. Kuma, and K. Shimada (2011), Iron and humic-type fluorescent dissolved organic matter in the Chukchi Sea and Canada Basin of the western Arctic Ocean, *Journal of Geophysical Research*, *116*(C7), C07031–17.

Perovich, D. K., and J. A. Richter-Menge (2009), Loss of sea ice in the Arctic, *Annual Review of Marine Science*, *1*(1), 417–441.

Planquette, H., R. M. Sherrell, S. Stammerjohn, and M. P. Field (2013), Particulate iron delivery to the water column of the Amundsen Sea, Antarctica, *Marine Chemistry*, *153*(C), 15-30.

Poulton, S. W., and R. Raiswell (2005), Chemical and physical characteristics of iron oxides in riverine and glacial meltwater sediments, *Chemical Geology*, *218*(3-4), 203-221.

Raiswell, R., and D. E. Canfield (2012), The iron biogeochemical cycle past and present, *Geochemical Perspectives*, *1*(1), 1-232.

Reimnitz, E. (2002), lnteractions of river discharge with sea ice in proximity of Arctic deltas: A review, *Polarforschung*, *70*, 123–134.

Sugie, K., J. Nishioka, K. Kuma, Y. N. Volkov, and T. Nakatsuka (2013), Availability of particulate Fe to phytoplankton in the Sea of Okhotsk, *Marine Chemistry*, *152*(C), 20-31.

Sunda, W.G., (2001), Bioavailability and Bioaccumulation of Iron in Seawater. In: Turner, D.R., Hunter, K.A. (Eds.), The Biogeochemistry of Iron in Seawater. Wiley, New York, pp. 41–84.

Thiagarajan, N., and C.-T. Aeolus Lee (2004), Trace-element evidence for the origin of desert varnish by direct aqueous atmospheric deposition, *Earth and Planetary Science Letters*, *224*(1-2), 131-141.

Tovar-Sánchez, A., C. M. Duarte, J. C. Alonso, S. Lacorte, R. Tauler, and C. Galbán-Malagón (2010), Impacts of metals and nutrients released from melting multiyear Arctic sea ice, *Journal of Geophysical Research*, *115*(C7), C07003.

Tremblay, J. É., et al. (2011), Climate forcing multiplies biological productivity in the coastal Arctic Ocean, *Geophysical Research Letters*, *38*(18), L18604.

Uglietti, C., P., Gabrielli, A. Lutton, J. Olesik, L. Thompson (2014), Large variability of trace element mass fractions determined by ICP-SFMS in ice core samples from worldwide high altitude glaciers, *Applied Geochemistry*, *47*, 109-121.

van der Merwe, P., D. Lannuzel, A. R. Bowie, and K. M. Meiners (2011), High temporal resolution observations of spring fast ice melt and seawater iron enrichment in East

Antarctica, *Journal of Geophysical Research*, *116*(G3), G03017.

Wang, S., D. Bailey, K. Lindsay, J. K. Moore, and M. Holland (2014), Impact of sea ice on the marine iron cycle and phytoplankton productivity, *Biogeosciences*, *11*(17), 4713-4731.

Wehrmann, L. M., M. J. Formolo, J. D. Owens, R. Raiswell, T. G. Ferdelman, N. Riedinger, and T. W. Lyons (2014), Iron and manganese speciation and cycling in glacially influenced high-latitude fjord sediments (West Spitsbergen, Svalbard): Evidence for a benthic recycling-transport mechanism, *Geochimica et Cosmochimica Acta*, *141*(C), 628-655.

Chapter 5

Conclusions

The interaction between climate, and ocean and atmosphere circulation can be reconstructed from sediments. In ice forming regions, this interaction can amplify climate change responses or potentially fuel marine productivity. The sensitivity of the marine environment to these changes can be amplified or muted by the amount of ice present in the region. A better understanding of both past and present ice forming regions is needed to improve future predictions of environmental change in polar regions in response to anthropogenic climate forcing.

In **Chapter 2**, ocean sediments were used to reconstruct a high-resolution history of the retreat of the southern marine margin of the Cordilleran Ice Sheet (CIS). It appears that the marine margin of the CIS was grounded and relatively stable despite warm SSTs after 19.8 ka, which is also supported by the lack of IRD during this interval. The combination of a grounded ice margin and a relatively high accumulation rate supplying ice from the Coast Mountains may have stabilized against retreat for almost 2 ka from 19.8 to 17.5 ka. Sedimentation at the end of modern tidewater glacial may build a morainal shoal that reduces iceberg calving (Meier and Post, 1987), and there is evidence from baythmetric features on the continental shelf that similar stabilizing processes were similarly important on the southern marine margin of the CIS (Mosher and Hewitt, 2004). Thus the retreat of the CIS was may have been forestalled despite the warm surface and subsurface ocean temperatures that exerted substantial thermal forcing along the tidewater ice terminus (Motyka, 2003; Rignot et al., 2010), similar to modern Alaskan and

Greenland tidewater glacial systems. However, the reconstructed deglacial history of the CIS is also consistent with modern studies implicating rapidly warming ocean temperatures in increasing ice discharge and the large-scale drawdown of land-based ice (Shepherd et al., 2004; Rignot et al., 2014; Jacobs et al., 2011).

A significant increase in iceberg calving from the CIS between ~17 to 15 ka has been observed around the margin of the eastern North Pacific. The CIS retreat from its marine margin began at 17.5 ka during significant pulse of IRD, which corresponded with ice rafting to the north where glaciomarine sediments in the Queen Charlotte Island region to the north in Hecate Strait where IRD appeared between 17.7–15.2 ka. New evidence from Alaskan Gulf sediment cores indicate large pulses of IRD along with brief surface water freshening occurred between 17.5 and 16.5 ka (Praetorius and Mix, 2014). Thus, from ~17.5 to 15.5 ka retreat via calving is indicated along the tidewater margin of the CIS in western Canada as ocean thermal forcing increased off shore of Vancouver Island. Such a coordinated discharge of IRD along several points of the CIS separated by hundreds of kilometers suggests that this phenomenon is not an accident of iceberg routing but instead that there is a major change in CIS dynamics along the marine margin. This interval of peak IRD discharge from the CIS occurs during Heinrich Event 1, when IRD from the Laurentide Ice Sheet (LIS) is also abundant in the North Atlantic (Hemming et al., 2004; Hendy and Cosma, 2008; Praetorius and Mix, 2014; Taylor et al., 2014). However, how the CIS ice margin may be responding uniformly to distal forcings is unclear. Work on the Alaskan margin cores is ongoing by another team of researchers, and should yield more information about the large-scale deglacial history of the CIS beyond the relatively warm southern margin of the ice sheet.

In the North Pacific Ocean there remain outstanding questions about the presence of fresh water from melting of the CIS. The occurrence of Lake Missoula outburst flooding which entered the ocean via the Columbia River, OR (Atwater, 1986; Brunner et al., 1999) and the presence of IRD in the North Pacific (Blaise et al., 1990; Hendy and Cosma, 2008; Praetorius and Mix, 2014) provides evidence of processes delivering freshwater to the North Pacific. However, there is little isotopic evidence of a significant meltwater such as has been recorded in $\delta^{18}O_{seawater}$ records from the Gulf of Mexico (Flower et al., 2004; Williams et al., 2012). Reconstructed $\delta^{18}O_{seawater}$ record at MD02-2496 shows no indication of isotopically depleted meltwater in the surface waters off Vancouver Island, BC. The absence of a meltwater signal in the $\delta^{18}O_{seawater}$ record despite clear evidence for meltwater input might be due to mixing of meltwater with warmer seawater near the glacial terminus. It is also likely that the isotopic composition of the CIS is less distinct from seawater than the LIS given its temperate latitude and proximity to moisture source.

The source of warm surface waters to the NE Pacific during the LGM off Vancouver Island became the focus of the next research question. In **Chapter 3**, reconstructed surface water characteristics indicate increased advection of waters from the Eastern Tropical North Pacific (ETNP) by relative strengthening of the California Undercurrent (CUC) that brought relatively warm, salty tropical waters poleward during Dangaard Oeschger Interstadial (DOI) events. Surface water reconstructions along the eastern and western Pacific margins are dominated by a warm, salty and cold, fresh dichotomy (Chen et al., 2010; Pak et al., 2012; Taylor et al., in revision) that have been interpreted to reflect changes in the relative proportion of southern versus northern sourced waters. Surface circulation is driven by changes in wind forcing, and atmospheric circulation, therefore proxy data showing changes in southern versus northern

sourced waters between DOI and Dangaard Oeschger stadials supports a reorganization of ocean/atmospheric circulation in the North Pacific. North Pacific ocean/atmosphere circulation reorganizations are teleconnected to climate change in Greenland (Timmerman et al., 2005; Zhang and Delworth, 2005; Menviel et al., 2014) and therefore could be forced by changes in North Atlantic meridional overturning circulation (MOC) and/or possibly changes in ice sheet topography (Li et al., 2010; Petersen et al., 2013; Zhang et al., 2014). In the modern ocean, the strength of the CUC responds to changes in sea surface heights in the tropical Pacific. I posit that the linkage between the strength of the CUC on the NE Pacific margin and DOIs may be related sea surface heights off Central America that increase when the Intertropical Convergence Zone (ITCZ) shifted northward. Northward movement of the ITCZ has been attributed to northern hemisphere atmospheric warming (Zhang and Delworth, 2005; Leduc et al., 2009).

The Mg/Ca records along the eastern North Pacific margin are noisy relative to their corresponding $\delta^{18}O_{calcite}$ records (Leduc et al., 2007; Pak et al., 2012, Taylor et al., in revision). A further complication for Pacific SST reconstructions involves the lack of SST calibrations for *N. pachyderma* Mg/Ca values. Additionally at MD02-2496 specimen scarcity prevented multiple analyses of outlier values to reduce data variability. In the future, increasing use of secondary ion mass spectrometry (SIMS) and laser ablation mass spectrometry will be enable the refining of Mg/Ca calibrations and analysis in foraminifera (Vetter et al., 2013). However, despite these issues the overall coherence between two species at MD02-2496, *N. pachyderma* and *G. bulloides*, indicated that temperature trends were robust in the record and demonstrated the utility of the use of multiple species in SST reconstructions.

In 2013, the Integrated Ocean Drilling Program (IODP) collected 3420 meters of core material from the margin of the Gulf of Alaska to establish the timing of advance and retreat

phases of the northern marine margin of CIS. These cores were drilled in a depth transect from the continental shelf to deeper sediments beneath the subartic gyre (IODP report, 2014). This new collection of cores will provide a northern perspective on changes in surface water circulation, bottom water oxygenation, productivity, ice-ocean interactions, and intermediate water masses during MIS 3 and the deglacial.

Annual and multiyear sea-ice creates another significant body of ice that plays a major role in the regional climate and biogeochemistry of the polar surface ocean. **Chapter 4** contains the results of a novel study characterizing sediment composition within Arctic sea ice in shallow continental shelf settings offshore from Barrow, AK and in the Canadian Arctic Archipelago. Here I investigated whether these sediments deposited onto and within sea ice constitute a reservoir of bioessential metals for surface dwelling primary producers. Continental shelves are projected to be regions of increased NO_3^- availability in a future warmer planet due to increased upwelling in shallow regions (Tremblay et al., 2011), especially in spring during the early phytoplankton bloom. It has been hypothesized that there is a greater likelihood of Fe limitations to primary producers in oceanic areas where more intense upwelling bring NO_3^- to surface waters (Taylor et al., 2013). In order to estimate the proportion bioavailable Fe in sea-ice sediments, we used a sediment leach protocol designed to extract "labile", or easily accessible crystalline and amorphous Fe-oxyhydroxides and biogenic Fe (Berger et al., 2008). Average sea ice sediment concentrations were ~150 to 750 ppb in the CAA cores, and were likely higher in the Barrow, AK cores. The ratio of labile to total Fe at these sites was high relative to the few measurements that have been made in the Arctic. Here I established an important baseline geochemistry for an environment that is rapidly changing due to anthropogenic climate change (Post et al., 2013). More work needs to be done to better constrain both community structure of primary producers

and to better establish the cellular demand for nutrients of these organisms before the importance of the high labile Fe concentrations found in sea ice sediments can be assessed. However, given the spatial and temporal variability of surface nutrients and uptake by phytoplankton as well as export from the surface mixed layer over the course of the growing season constraining Arctic primary production requirements may be difficult (Popova et al., 2012). Iron isotopes have been utilized during algal blooms to map these processes in situ, and also in shipboard mesocosm experiments in the subtropical Pacific Ocean through programs like GEOTRACES (Ellwood et al., 2014). Similar experiments conducted in the Arctic would likewise be informative.

More work also needs to be undertaken to constrain sediments sources, in addition to sediment transport and delivery mechanisms in order to understand the dominant processes enriching sediments in sea ice. Processes concentrating sediments in sea ice are likely dependent the age and thickness of sea ice which will dictate the length of time over which these processes operate. Additionally the location will play a role. Sea ice closer to shore and in shallower seas likely have greater influx of terrigenous sediments from runoff, ice caps or glaciers, or upwelled shelf sediments. Sea ice further from shore may have a great component of dust relative to these other inputs. Finally, Fe speciation would be useful to determine biogenic versus inorganic sediments as well as bioavailability.

References

Berger, C. J. M., S. M. Lippiatt, M. G. Lawrence, and K. W. Bruland (2008), Application of a chemical leach technique for estimating labile particulate aluminum, iron, and manganese in the Columbia River plume and coastal waters off Oregon and Washington, *Journal of Geophysical Research*, *113*, C00B01.

Blaise, B., J. J. Clague, and R. W. Mathewes (1990), Time of maximum late Wisconsin glaciation, west coast of Canada, *Quaternary Research*, *34*, 282-295.

Brunner, C. A., W. R. Normark, S. F, and G. G. Zuffa (1999), Deep-sea sedimentary record of the late Wisconsin cataclysmic floods from the Columbia River, *Geology*, *27*(5), 463-466.

Chen, M. T., X. P. Lin, Y. P. Chang, Y. C. Chen, L. Lo, C. C. Shen, Y. Yokoyama, D. W. Oppo, W. G. Thompson, and R. Zhang (2010), Dynamic millennial-scale climate changes in the northwestern Pacific over the past 40,000 years, *Geophysical Research Letters*, *37*(23), L23603.

Ellwood, M. J., D. A. Hutchins, M. C. Lohan, A. Milne, P. Nasemann, S. D. Nodder, S. G. Sander, R. Strzepek, S. W. Wilhelm, and P. W. Boyd (2015), Iron stable isotopes track pelagic iron cycling during a subtropical phytoplankton bloom, *Proceedings of the National Academy of Sciences*, *112*(1), E15-E20.

Expedition 341 Scientists (2013), Integrated Ocean Drilling Program Expedition 341 Preliminary Report Southern Alaska Margin: Interactions of tectonics, climate, and sedimentation, Published by Integrated Ocean Drilling Program.

Flower, B. P., D. W. Hastings, H. W. Hill, and T. M. Quinn (2004), Phasing of deglacial warming and Laurentide Ice Sheet meltwater in the Gulf of Mexico, *Geology*, *32*(7), 597.

Hemming, S. R. (2004), Heinrich events: Massive late Pleistocene detritus layers of the North Atlantic and their global climate imprint, *Reviews of Geophysics*, *42*(1), RG1005.

Hendy, I. L., and T. Cosma (2008), Vulnerability of the Cordilleran Ice Sheet to iceberg calving during late Quaternary rapid climate change events, *Paleoceanography*, *23*.

Jacobs, S. S., A. Jenkins, C. F. Giulivi, and P. Dutrieux (2011), Stronger ocean circulation and increased melting under Pine Island Glacier ice shelf, *Nature Geoscience*, *4*(8), 519-523.

Leduc, G., L. Vidal, K. Tachikawa, and E. Bard (2009), ITCZ rather than ENSO signature for abrupt climate changes across the tropical Pacific?, *Quaternary Research*, *72*(1), 123-131.

Leduc, G., L. Vidal, K. Tachikawa, F. Rostek, C. Sonzogni, L. Beaufort, and E. Bard (2007), Moisture transport across Central America as a positive feedback on abrupt climatic

changes, *Nature*, *445*(7130), 908-911.

Li, C., D. S. Battisti, and C. M. Bitz (2010), Can North Atlantic sea ice anomalies account for Dansgaard–Oeschger climate signals?*, *Journal of Climate*, *23*(20), 5457-5475.

Meier, M. F., and A. Post (1987), Fast tidewater tlaciers, *Journal of Geophysical Research*, *92*(B9), 9051-9058.

Menviel, L., A. Timmermann, T. Friedrich, and M. H. England (2014), Hindcasting the continuum of Dansgaard-Oeschger variability: mechanisms, patterns and timing, *Climate of the Past*, *10*(1), 63-77.

Mosher, D. C., and A. T. Hewitt (2004), Late Quaternary deglaciation and sea-level history of eastern Juan de Fuca Strait, Cascadia, *Quaternary International*, *121*, 23-39.

Motyka, R. J., L. Hunter, K. A. Echelmeyer, and C. Connor (2003), Submarine melting at the terminus of a temperate tidewater glacier, LeConte Glacier, Alaska, U.S.A., *Annals of Glaciology*, *36*, 57-65.

Pak, D. K., D. W. Lea, and J. P. Kennett (2012), Millennial scale changes in sea surface temperature and ocean circulation in the northeast Pacific, 10–60 kyr BP, *Paleoceanography*, *27*(1), PA1212.

Petersen, S. V., D. P. Schrag, and P. U. Clark (2013), A new mechanism for Dansgaard-Oeschger cycles, *Paleoceanography*, *28*, 1-7.

Popova, E. E., A. Yool, A. C. Coward, F. Dupont, C. Deal, S. Elliott, E. Hunke, M. Jin, M. Steele, and J. Zhang (2012), What controls primary production in the Arctic Ocean? Results from an intercomparison of five general circulation models with biogeochemistry, *Journal of Geophysical Research*, *117*, C00D12.

Post, E., U. S. Bhatt, C. M. Bitz, J. F. Brodie, T. L. Fulton, M. Hebblewhite, J. Kerby, I. Stirling, and D. A. Walker (2013), Ecological consequences of sea-ice decline, *Science*, *341*(6145), 519-524.

Praetorius, S. K., and A. C. Mix (2014), Synchronization of North Pacific and Greenland climates preceded abrupt deglacial warming, *Science*, *345*(6195), 444-448.

Rignot, E., M. Koppes, and I. Velicogna (2010), Rapid submarine melting of the calving faces of West Greenland glaciers, *Nature Geoscience*, *3*, 187-191.

Rignot, E., J. Mouginot, M. Morlighem, H. Seroussi, and B. Scheuchl (2014), Widespread, rapid grounding line retreat of Pine Island, Thwaites, Smith, and Kohler glaciers, West Antarctica, from 1992 to 2011, *Geophysical Research Letters*, *41*, 3502-3509.

Shepherd, A. (2004), Warm ocean is eroding West Antarctic Ice Sheet, *Geophysical Research Letters*, *31*(23), L23402.

Taylor, M. A., I. L. Hendy, and D. K. Pak (2014), Deglacial ocean warming and marine margin retreat of the Cordilleran Ice Sheet in the North Pacific Ocean, *Earth and Planetary Science Letters*, *403*(C), 89-98.

Taylor, M. A., I. L. Hendy, and D. K. Pak (in revision), The California Current System as a transmitter of millennial scale climate change on the northeastern Pacific margin from 10-50 ka, *Paleoceanography*.

Taylor, R. L., D. M. Semeniuk, C. D. Payne, J. Zhou, J.-É. Tremblay, J. T. Cullen, and M. T. Maldonado (2013), Colimitation by light, nitrate, and iron in the Beaufort Sea in late summer, *Journal of Geophysical Research: Oceans*, *118*(7), 3260-3277.

Timmermann, A., U. Krebs, F. Justino, H. Goosse, and T. Ivanochko (2005), Mechanisms for millennial-scale global synchronization during the last glacial period, *Paleoceanography*, *20*(4), PA4008.

Tremblay, J. É., et al. (2011), Climate forcing multiplies biological productivity in the coastal Arctic Ocean, *Geophysical Research Letters*, *38*(18), L18604.

Vetter, L., H. J. Spero, A. D. Russell, and J. S. Fehrenbacher (2013), LA-ICP-MS depth profiling perspective on cleaning protocols for elemental analyses in planktic foraminifers, *Geochemistry Geophysics Geosystems*, *14*(8), 2916-2931.

Williams, C., B. P. Flower, and D. W. Hastings (2012), Seasonal Laurentide Ice Sheet melting during the "Mystery Interval" (17.5-14.5 ka), *Geology*, *40*(10), 955-958.

Zhang, R., and T. L. Delworth (2005), Simulated Tropical Response to a Substantial Weakening of the Atlantic Thermohaline Circulation, *Journal of Climate*, *18*, 1853-1860.

Zhang, X., G. Lohmann, G. Knorr, and C. Purcell (2015), Abrupt glacial climate shifts controlled by ice sheet changes, *Nature*, *512*(7514), 290-294.

Appendix A

Supplementary Figures and Tables for Chapters 2 and 3

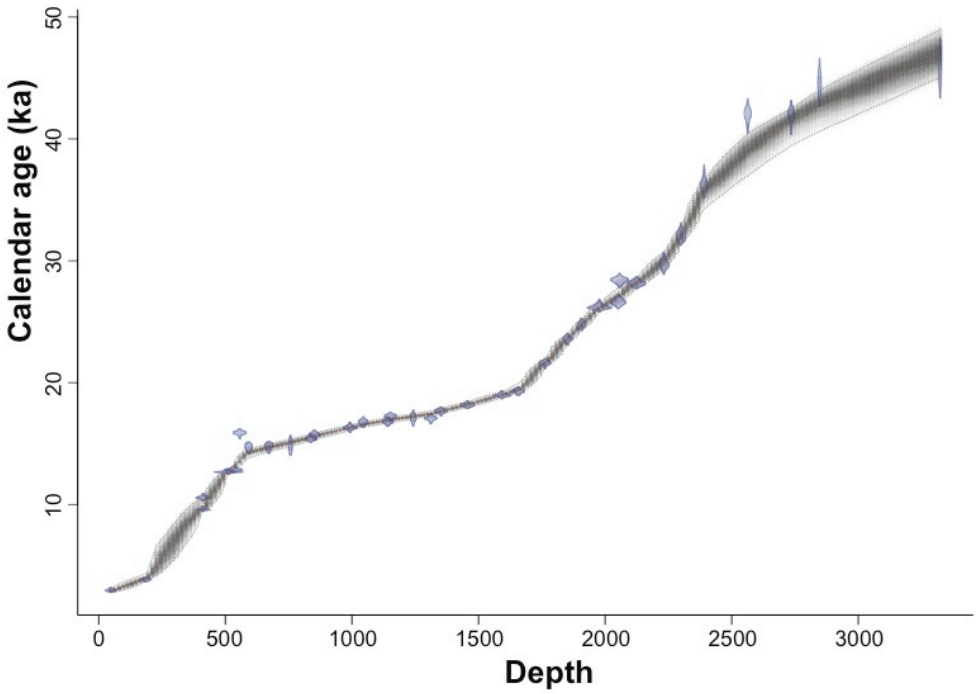

Figure A.1
Age in calendar years B.P. versus core depth (corrected cm below core top). Age model was generated using calibrated mixed planktonic species and bulk organic carbon (purple marks) radiocarbon dates (Cosma et al., 2008). The previously published radiocarbon dates were recalibrated using the MARINE13 calibration (Reimer et al., 2013). The age model (red dotted line) is a Bayesian interpolation between dates generated with Monte Carlo simulated age model errors (width of black line) using Bacon 2.2 (Blaau and Christen, 2011).

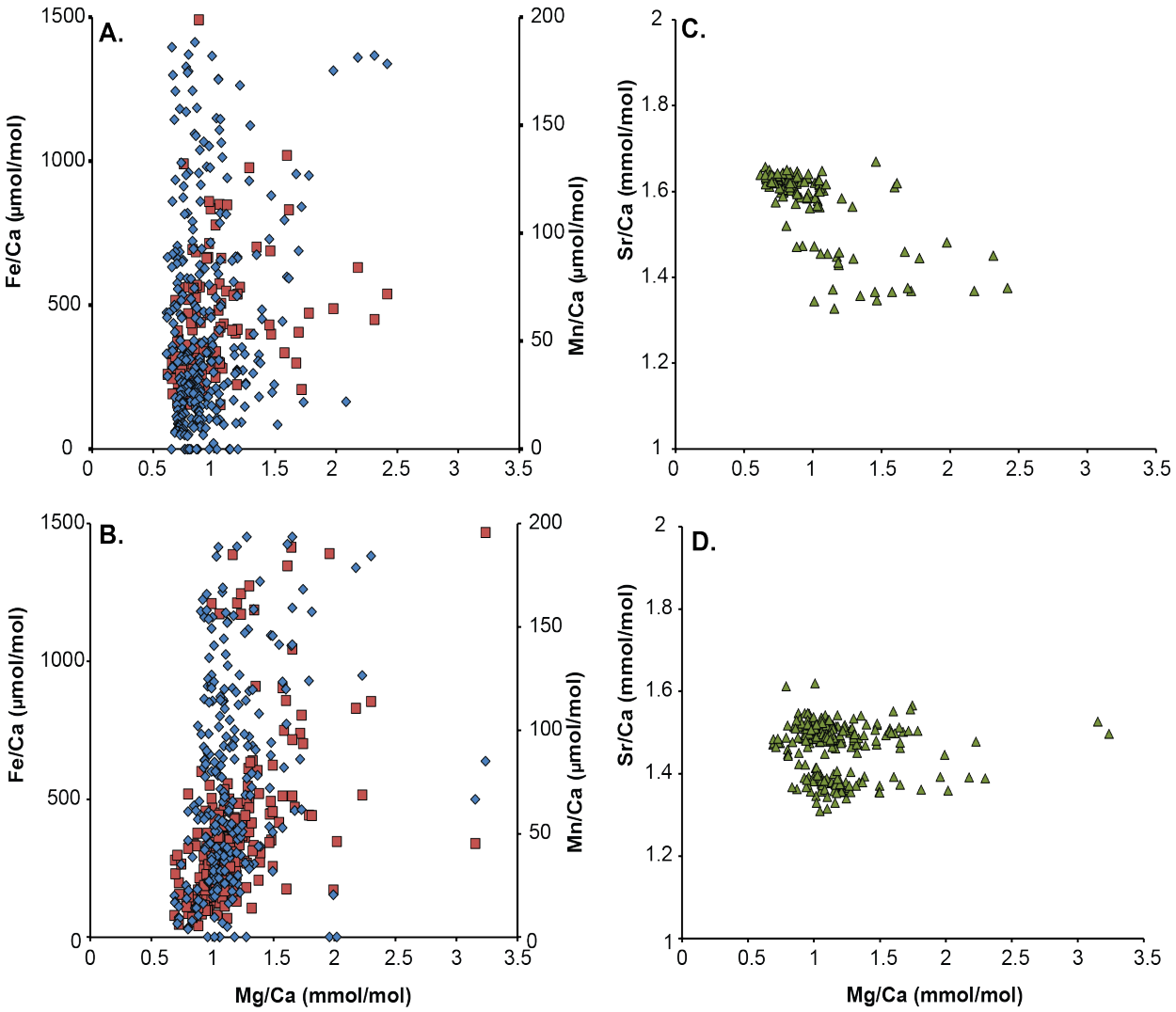

Figure A.2
Fe/Ca (µmol/mol) (blue diamonds) and Mn/Ca (µmol/mol) (red squares) ratios versus Mg/Ca (mmol/mol) ratios for (A) *N. pachyderma* and (B) *G. bulloides*. Sr/Ca (mmol/mol) ratios (green triangles) versus Mg/Ca (mmol/mol) ratios for (C) *N. pachyderma* and (D) *G. bulloides*.

Table A.1
Radiocarbon dates, calibrated calendar ages datum in core MD02-2496

ID	Sample Interval	Depth[ß] (cm)	^{14}C age[¥]	Lab error (years)	Calendar Age (years)[ƒ]	1 Sigma range (years)	2 Sigma range (years)	Depth (cm)	Datum (years)
UCIAMS 31569	60-61.5	48	3080[Ï]	±15	2374.5	67.5	126		
UCIAMS 31570	75-76.5	63	3295[Ï]	±15	2690.5	52.5	201	70.5*	2836*
UCIAMS 31571	85-86.5	73	3525[Ï]	±15	2898.5	73.5	135		
UCIAMS 31572	110-111.5	98	3890[Ï]	±15	3382	62	150		
UCIAMS 31573	205-206.5	185	4175[Ï]	±15				-	-
UCIAMS 31574	574-576.5	-	7210[Ï]	±20				-	-
UCIAMS 31569	700-701.5	412	9215[Ï]	±25	10354.5	60.5	88	412	10524*
CAMS 107298	700-701.5	412	10065	±45	10693	92	145		
CAMS 120938	740-741.5	452	11850	±150				-	-
CAMS 118214	800-801.5	512	11565	±40	12660	55	102	522*	12750*
CAMS 107299	820-821.5	532	11790	±45	12840.5	88.5	160		
CAMS 120937	840-841.5	552	14025	±50				-	-
CAMS 118215	880-881.5	592	13305	±40	14736	228	449	592	14736
CAMS 107300	960-961.5	672	13340	±50				-	-
CAMS 118216	1045-1047	757	13390	±180				-	-
CAMS 118217	1125-1127	837	13695	±45	15385	132.5	222.5	845*	15563*
CAMS 107302	1140-1141.5	852	13920	±60	15741	146	340		
CAMS 118218	1280-1281.5	992	14340	±45	16290	118	224	1018.5*	16536*
CAMS 118219	1333-1335	1045	14660	±70	16781	164	339		
CAMS 118220	1430-1432	1142	14695	±45	16830.5	141.5	295.5	1147*	17036*
CAMS 118222	1440-1441.5	1152	14970	±50	17242	127	238		
CAMS 118221	1530-1532	1242	14900	±150				-	-
CAMS 107303	1600-1601.5	1312	14855	±45				-	-
CAMS 107304	1640-1641.5	1352	15310	±60	17678.5	120.5	219.5	1352	17679
CAMS 118223	1745-1747	1457	15765	±50	18183	111	225	1457	18183
CAMS 107305	1880-1881.5	1592	16510	±60	18938	91	161	1592	18938
CAMS 118224	1945-1947	1657	16800	±60	19308	128	259	1657	19308
CAMS 118225	2050-2052	1762	18650	±60	21632.5	133.5	270.5	1762	21633
CAMS 107306	2140-2141.5	1852	20420	±90	23636	154	319	1852	23636
CAMS 118226	2195-2197	1907	21370	±90	24747.5	200.5	338.5	1907	24748
CAMS 118227	2265-2267	1977	22780	±100	26165	137	227	1977	26165
CAMS 107307	2340-2341.5	2052	23150	±120	26614.5	231.5	399.5	2052	26615
CAMS 118229	2345-2347	2057	25190	±140				-	-
CAMS 118228	2412-2413.5	2124	24930	±120	28144.5	178.5	311.5	2124	28145
CAMS 107308	2520-2521.5	2232	26380	±200	29718	315	562	2232	29718
CAMS 118230	2588-2590	2300	29010	±200	32016.5	360.5	548.5	2300	32017
CAMS 118231	2688-2690	2391	33150	±320	36220	372	765	2391	36220
CAMS 118233	2860-2861.5	2563	38590	±640				-	-
CAMS 118232	3032-3034	2735	38430	±600	41980.5	424.5	972.5	2735	41981
CAMS 118234	3144-3146	2847	41900	±930	44544.5	812.5	1561.5	2847	44545
CAMS 120936	3325-3327	3028	>44900					-	-
CAMS 120935	3390-3392	3093	>51300					-	-
CAMS 120934	3480-3481.5	3183	>50500					-	-
CAMS 120933	3560-3561.5	3263	>48900					-	-
CAMS 118235	3620-3621.5	3323	43100	±1060	45596	982	1960	3323	45596
CAMS 118236	574-576		14720[Ω]	±280				-	-

[ß] Depth was corrected for voids and disturbed sediments (see Table 1).

[¥] ^{14}C ages were not corrected for reservoir effect by 807 years (Robinson and Thompson, 1981).

[ƒ] Calendar ages between 22 ^{14}C Kyr and present were determined by CALIB04 (Stuiver et al., 2004).
Calendar ages beyond 22 ^{14}C Kyr were calibrated using the radiocarbon data of Hughen et al., (2004).
Calibrations were generated using interpolation between data points.

* Ages and depths were averaged.

[Ω] ^{14}C age was generated from mixed benthic foraminiferal species.

[Ï] ^{14}C age was generated from bulk organic carbon.

Table A.2
Neogloboquadrina pachyderma data for MD02-2496

Corrected Depth (cm)	Age kyr	Mg/Ca (mmol/mol)	SST (°C)	$\delta^{18}O_{calcite}$ (VPDB)	Ice volume corrected $\delta^{18}O_{calcite}$ (VPDB)	$\delta^{18}O_{seawater}$ (VSMOW)
407	9.826	0.84	4.8	1.38	1.00	
467	11.395	0.91	5.6	2.17	1.60	-0.88
482	11.821	1.36	9.6	2.39	1.82	0.37
487	11.964	0.88	5.2	2.36	1.79	-0.79
497	12.264	0.73	3.4	2.82	2.15	-0.92
517	12.702	1.23	8.6	1.74	1.07	-0.65
532	12.936	0.97	6.2	1.69	1.02	-1.30
537	13.082	1.03	6.9	1.80	1.02	-1.13
547	13.373	0.97	6.3	1.62	0.84	-1.47
562	13.746	1.38	9.8	2.03	1.25	-0.17
567	13.868	1.29	9.1	2.19	1.41	-0.18
577	14.032	1.05	7.0	1.71	0.84	-1.28
587	14.186	1.36	9.6	1.87	1.00	-0.47
599	14.275	1.60	11.2	2.01	1.14	0.07
622	14.412	1.61	11.3	3.01	2.14	1.09
627	14.439	0.98	6.3	3.13	2.26	-0.04
667	14.649	1.11	7.6	2.88	2.01	0.03
677	14.700	0.99	6.4			
697	14.799	1.32	9.3	2.54	1.67	0.13
707	14.847	1.24	8.7	2.52	1.65	-0.06
722	14.918	0.88	5.3	2.44	1.57	-1.00
797	15.297	0.97	6.2	2.83	1.87	-0.45
802	15.323	1.05	7.0	2.85	1.89	-0.22
807	15.349	1.03	6.9	2.80	1.84	-0.31
812	15.374	1.02	6.7	2.81	1.85	-0.34
817	15.400	0.96	6.1	2.94	1.98	-0.37
847	15.564	0.89	5.3	2.72	1.76	-0.79
852	15.591	0.98	6.4	2.95	1.99	-0.30
882	15.746	0.87	5.2	2.59	1.63	-0.96
902	15.847	1.04	7.0	2.69	1.73	-0.40
942	16.053	0.91	5.6	2.98	1.95	-0.53
967	16.181	0.91	5.6	2.95	1.92	-0.55
972	16.207	1.08	7.3	3.22	2.19	0.14
992	16.309	0.83	4.6	2.97	1.94	-0.80
997	16.334	1.10	7.5	3.20	2.17	0.17
1012	16.407	1.04	7.0	3.04	2.01	-0.12
1017	16.432	0.86	5.0	3.05	2.02	-0.62
1022	16.456	0.84	4.8	3.01	1.98	-0.70
1027	16.481	0.66	2.5	2.94	1.91	-1.41
1037	16.526	0.89	5.3	3.00	1.97	-0.58
1042	16.549	0.68	2.7	3.37	2.34	-0.90
1067	16.643	1.04	7.0	3.04	2.01	-0.12
1127	16.861	0.75	3.7	3.00	1.97	-1.02
1137	16.898	0.92	5.7	3.12	2.09	-0.37
1147	16.937	0.78	4.1	2.94	1.91	-0.97
1152	16.954	0.71	3.1	3.02	1.99	-1.14
1182	17.049	0.72	3.2	3.07	1.99	-1.13
1207	17.124	0.84	4.7	3.13	2.05	-0.65
1212	17.139	0.79	4.2	2.89	1.81	-1.05
1252	17.261	0.74	3.6	3.21	2.13	-0.88
1257	17.276	0.83	4.7	3.02	1.94	-0.78
1267	17.308	0.69	2.8	2.92	1.84	-1.38
1277	17.339	0.72	3.3	3.19	2.11	-0.98
1282	17.355	0.68	2.7	3.13	2.05	-1.19
1287	17.371	0.74	3.5	3.14	2.06	-0.98
1302	17.419	0.70	3.0	2.99	1.91	-1.26
1307	17.435	0.66	2.4	3.18	2.10	-1.25
1312	17.456	0.67	2.6	3.29	2.21	-1.08
1317	17.479	0.64	2.1	3.26	2.18	-1.23
1322	17.502	0.68	2.7	3.23	2.15	-1.11
1327	17.526	0.85	4.9	3.18	2.10	-0.55
1332	17.552	0.61	1.6	3.01	1.93	-1.61
1337	17.580	0.66	2.4	3.18	2.10	-1.23
1342	17.608	0.85	4.9	3.13	2.05	-0.60
1382	17.822	0.79	4.2	3.18	2.10	-0.75
1402	17.926	0.62	1.7	2.94	1.86	-1.67
1417	18.004	0.71	3.1	3.08	1.98	-1.17
1427	18.057	0.61	1.5	3.08	1.98	-1.59
1432	18.083	0.79	4.1	3.21	2.11	-0.75
1437	18.109	0.65	2.3	3.05	1.95	-1.42
1447	18.161	0.82	4.6	2.97	1.87	-0.89
1452	18.187	0.97	6.2	2.65	1.55	-0.77
1457	18.214	0.82	4.6	2.74	1.64	-1.11
1467	18.267	0.77	3.9	2.93	1.83	-1.09
1472	18.296	0.82	4.6	2.44	1.34	-1.41
1478	18.331	1.03	6.9	2.60	1.50	-0.65
1482	18.355	0.99	6.5	2.60	1.50	-0.75
1487	18.384	0.89	5.4	2.64	1.54	-1.00
1492	18.413	0.91	5.6	2.49	1.39	-1.10
1507	18.500	0.85	4.9	2.90	1.80	-0.88
1512	18.530	0.81	4.5	2.99	1.89	-0.89
1517	18.560	0.67	2.6	2.63	1.53	-1.75
1522	18.590	0.74	3.6	2.78	1.68	-1.34
1527	18.620	0.90	5.4	2.97	1.87	-0.65
1537	18.678	0.62	1.7	3.05	1.95	-1.57
1542	18.707	0.70	3.0	2.90	1.80	-1.37
1547	18.736	0.66	2.3	3.26	2.16	-1.20
1552	18.766	0.68	2.7	2.65	1.55	-1.71
1557	18.795	0.66	2.4	3.01	1.91	-1.44
1562	18.826	1.11	7.6	2.93	1.83	-0.15
1567	18.855	0.70	2.9	2.57	1.47	-1.72
1577	18.912	0.72	3.2	2.93	1.83	-1.28
1597	19.038	0.72	3.3	2.85	1.75	-1.34
1607	19.107	0.76	3.8	3.00	1.90	-1.07
1612	19.142	0.87	5.1	2.76	1.66	-0.95
1617	19.177	0.66	2.4	2.52	1.42	-1.93
1627	19.247	0.76	3.8	2.95	1.85	-1.12
1637	19.319	0.81	4.4	2.73	1.63	-1.16
1652	19.437	1.05	7.0	2.79	1.69	-0.43
1657	19.488	1.08	7.3	2.60	1.50	-0.55
1662	19.538	0.86	5.0	2.88	1.78	-0.86
1672	19.680	0.77	4.0	2.45	1.35	-1.56
1682	19.887	1.14	7.9	2.82	1.72	-0.17
1692	20.094	0.93	5.8	2.84	1.75	-0.68
1702	20.305	1.19	8.3	2.86	1.77	-0.03
1707	20.410	0.88	5.3	2.94	1.85	-0.72
1717	20.624	0.84	4.8	2.86	1.77	-0.93
1727	20.839	0.87	5.1	2.94	1.85	-0.77
1737	21.047	0.73	3.4	2.77	1.69	-1.38
1747	21.255	0.83	4.7	2.96	1.88	-0.83
1757	21.475	0.74	3.5	2.90	1.82	-1.22
1767	21.700	1.01	6.7	2.64	1.56	-0.64
1777	21.927	0.72	3.2	2.85	1.77	-1.33
1782	22.039	0.82	4.5	2.89	1.84	-0.93
1782	22.039	0.85	4.9	2.89	1.84	-0.84
1787	22.150	0.75	3.7	2.84	1.79	-1.21
1792	22.257	0.82	4.5	2.85	1.80	-0.96
1797	22.364	0.76	3.7	2.74	1.69	-1.29
1807	22.581	0.79	4.2	3.12	2.07	-0.78
1817	22.805	0.83	4.6	2.84	1.79	-0.95
1822	22.917	0.75	3.7	2.88	1.83	-1.16
1827	23.030	0.89	5.4	2.95	1.93	-0.60
1837	23.252	0.80	4.3	2.63	1.61	-1.22
1847	23.474	0.95	6.0	2.90	1.88	-0.49
1867	23.928	0.82	4.6	2.62	1.60	-1.15
1872	24.032	1.08	7.3	3.19	2.21	0.17
1877	24.134	1.25	8.8	3.06	2.08	0.41
1887	24.336	1.32	9.3	3.21	2.23	0.70
1897	24.535	0.83	4.6	2.55	1.57	-1.17
1907	24.733	0.87	5.2	2.96	1.98	-0.61
1917	24.938	0.69	2.8	3.10	2.12	-1.11
1922	25.039	0.79	4.1	2.84	1.90	-0.98
1927	25.139	0.70	3.0	3.10	2.16	-1.01
1932	25.238	0.95	6.0			
1937	25.336	0.70	3.0	3.28	2.34	-0.84
1942	25.434	0.60	1.5	3.30	2.36	-1.24
1947	25.532	1.02	6.8	3.18	2.24	0.05
1952	25.632	1.02	6.7	2.88	1.94	-0.26
1962	25.832	1.25	8.8	2.91	1.97	0.29
1967	25.931	0.87	5.1	2.78	1.84	-0.78
1972	26.021	0.74	3.5	3.09	2.18	-0.85
1977	26.109	0.68	2.7	3.00	2.09	-1.17
1987	26.287	0.71	3.1	2.77	1.86	-1.30
1992	26.356	0.81	4.4	3.04	2.13	-0.66
2002	26.483	1.12	7.7	2.98	2.07	0.12
2007	26.545	1.04	6.9	2.73	1.82	-0.33
2017	26.673	0.89	5.4	2.78	1.87	-0.68
2022	26.737	0.71	3.1	2.80	1.89	-1.26
2027	26.801	0.73	3.4	2.74	1.83	-1.25
2047	27.053	0.88	5.2	2.39	1.50	-1.08
2067	27.408	0.79	4.2	2.16	1.27	-1.58
2077	27.550	1.13	7.8	2.49	1.60	-0.33
2087	27.689	0.86	5.0	2.56	1.67	-0.96
2092	27.759	0.65	2.2	3.05	2.16	-1.22
2092	27.759	0.68	2.6	3.05	2.16	-1.11
2120	28.148	0.70	2.9	3.10	2.22	-0.98
2132	28.327	0.75	3.7	2.34	1.46	-1.52
2152	28.661	0.73	3.4	3.09	2.21	-0.86
2156	28.729	0.80	4.3	3.10	2.22	-0.60
2168	28.933	1.46	10.3	3.25	2.37	1.08
2172	29.001	0.72	3.3	2.89	2.02	-1.08
2176	29.069	0.94	5.9	3.28	2.41	0.00
2180	29.137	0.74	3.5	3.30	2.43	-0.61
2188	29.272	0.74	3.5	3.14	2.27	-0.77
2200	29.477	0.75	3.6	3.02	2.15	-0.85
2204	29.545	1.03	6.8	3.21	2.34	0.18
2208	29.612	0.73	3.4	3.15	2.28	-0.79
2212	29.680	0.89	5.3	3.35	2.48	-0.07
2216	29.748	0.74	3.5	3.27	2.40	-0.64
2220	29.816	0.81	4.4	3.20	2.33	-0.46
2224	29.883	0.79	4.1	3.15	2.28	-0.59
2224	29.949	0.79	4.2	3.15	2.28	-0.58
2232	30.045	0.65	2.2			
2236	30.145	0.70	2.9	3.01	2.15	-1.05
2240	30.242	0.88	5.3	2.79	1.93	-0.64
2240	30.242	1.17	8.1	2.79	1.93	0.09
2252	30.558	0.72	3.3	2.89	2.03	-1.06
2256	30.682	0.78	4.1	3.15	2.29	-0.60
2260	30.807	0.74	3.6	2.99	2.13	-0.90
2264	30.931	0.88	5.2	3.06	2.20	-0.38
2268	31.055	1.27	8.9	2.81	1.95	0.31
2272	31.180	1.08	7.4	2.99	2.13	0.10
2280	31.431	1.06	7.1	2.72	1.86	-0.23
2284	31.553	1.52	10.7	2.96	2.10	0.90
2288	31.676	0.65	2.3	3.19	2.33	-1.04
2292	31.809	0.75	3.6	3.02	2.16	-0.85
2296	31.943	0.59	1.3	3.06	2.20	-1.43
2300	32.078	0.80	4.4	2.98	2.12	-0.69
2304	32.214	0.62	1.8	3.02	2.16	-1.33
2312	32.508	1.15	7.9			
2316	32.668	1.11	7.6	3.04	2.18	0.21
2320	32.825	0.69	2.9	2.77	1.91	-1.29
2324	32.981	1.18	8.2	3.04	2.18	0.36
2328	33.135	1.65	11.6	3.05	2.19	1.21
2332	33.295	1.59	11.2	2.82	1.96	0.89
2332.5	33.295	0.88	5.3			
2333	33.335	0.74	3.5			
2337	33.494	1.45	10.3	2.63	1.77	0.47
2341	33.653	0.76	3.8	2.63	1.77	-1.18
2343	33.734	0.81	4.5	3.02	2.16	-0.62
2343	33.734	0.87	5.1	3.02	2.16	-0.44
2343	33.734	1.41	10.0	3.02	2.16	0.79
2347	33.894	0.77	3.9	2.86	2.00	-0.93
2351	34.052	0.72	3.2	2.89	2.03	-1.09
2355	34.212	1.05	7.0	2.96	2.10	-0.01
2363	34.532	0.88	5.2	2.97	2.11	-0.46
2367	34.690	0.72	3.3	2.88	2.02	-1.08
2371	34.849	1.39	9.9	2.43	1.57	0.17
2375	35.006	0.84	4.8	2.49	1.63	-1.06
2379	35.164	0.82	4.6	2.50	1.64	-1.11
2383	35.320	0.91	5.6	2.73	1.87	-0.62
2387	35.475	0.88	5.3	2.83	1.97	-0.60
2391	35.585	0.94	5.9	2.64	1.78	-0.61
2397	35.723	0.78	4.1	3.01	2.15	-0.74
2403	35.860	0.71	3.1	2.71	1.85	-1.31
2411	36.030	0.73	3.4	2.88	2.02	-1.05
2419	36.180	0.74	3.5	2.97	2.11	-0.92
2427	36.333	0.86	5.0	2.96	2.10	-0.53

Table A.2 continued

Corrected Depth (cm)	Age kyr	Mg/Ca (mmol/mol)	SST (˚C)	$\delta^{18}O_{calcite}$ (VPDB)	Ice volume corrected $\delta^{18}O_{calcite}$ (VPDB)	$\delta^{18}O_{seawater}$ (VSMOW)
2435	36.485	0.70	2.9	3.09	2.23	-0.97
2451	36.788	0.79	4.2	2.88	2.02	-0.85
2459	36.940	1.06	7.2	2.88	2.02	-0.06
2467	37.092	0.73	3.4	3.00	2.14	-0.92
2479	37.325	1.33	9.4	2.50	1.64	0.11
2483	37.402	0.71	3.2			
2491	37.557	0.68	2.6	2.94	2.08	-1.20
2499	37.708	0.87	5.1	3.03	2.17	-0.45
2508	37.875	0.83	4.7	2.83	1.97	-0.75
2516	38.027	0.78	4.1	2.36	1.51	-1.38
2523	38.162	0.87	5.2	2.64	1.79	-0.81
2527	38.239	0.80	4.3	2.78	1.93	-0.89
2539	38.467	0.88	5.3	2.96	2.11	-0.46
2551	38.697	0.88	5.3	2.40	1.55	-1.01
2555	38.773	1.26	8.8	2.25	1.40	-0.26
2563	38.926	0.75	3.7	2.21	1.36	-1.63
2575	39.119	0.71	3.1	2.49	1.65	-1.49
2583	39.228	0.86	5.0	2.81	1.97	-0.68
2591	39.339	0.78	4.1	2.91	2.07	-0.82
2599	39.451	0.79	4.1			
2607	39.563	0.94	5.9	3.07	2.23	-0.18
2615	39.677	0.76	3.8	2.81	1.97	-1.00
2623	39.790	0.81	4.5	2.94	2.10	-0.69
2631	39.903	0.88	5.3	2.76	1.92	-0.65
2639	40.017	0.80	4.3	2.43	1.60	-1.22
2639	40.017	0.83	4.6	2.43	1.60	-1.14
2647	40.130	0.82	4.5	2.75	1.92	-0.85
2655	40.242	0.99	6.5	2.89	2.06	-0.19
2675	40.517	0.89	5.3	2.33	1.50	-1.05
2683	40.629	1.08	7.3	2.40	1.57	-0.47
2691	40.739	0.96	6.1	2.15	1.32	-1.03
2699	40.849	0.72	3.3	2.19	1.36	-1.74
2703	40.904	1.18	8.2	2.49	1.66	-0.17
2707	40.959	1.59	11.2	2.64	1.81	0.73
2711	41.014	0.68	2.7	2.52	1.70	-1.54
2719	41.125	0.82	4.6	2.58	1.76	-0.99
2723	41.181	0.73	3.4	2.76	1.94	-1.13
2727	41.235	0.85	4.9	2.64	1.82	-0.84
2727	41.235	0.90	5.5	2.64	1.82	-0.69
2727	41.235	1.74	12.1	2.64	1.82	0.96
2731	41.288	0.73	3.4	2.44	1.62	-1.45
2739	41.393	0.76	3.8	2.51	1.69	-1.26
2763	41.686	1.12	7.7	2.36	1.54	-0.41
2767	41.732	0.80	4.4	2.49	1.67	-1.14
2771	41.779	0.88	5.3	2.67	1.85	-0.71
2775	41.824	0.81	4.5	2.75	1.93	-0.85
2779	41.869	0.71	3.1	2.69	1.87	-1.27
2783	41.916	0.73	3.4	2.76	1.94	-1.13
2787	41.961	0.91	5.6	2.62	1.80	-0.69
2795	42.055	0.71	3.1	2.87	2.06	-1.09
2799	42.100	0.75	3.7	2.90	2.09	-0.90
2803	42.146	0.77	3.9	2.90	2.09	-0.83
2811	42.239	0.79	4.2	2.98	2.17	-0.68
2819	42.331	0.74	3.5	2.71	1.90	-1.13
2827	42.425	0.69	2.9	3.23	2.42	-0.79
2835	42.516	0.73	3.3	2.87	2.06	-1.02
2839	42.562	0.69	2.8	2.93	2.12	-1.11
2839	42.562	0.69	2.9	2.93	2.12	-1.08
2851	42.693	0.67	2.5	2.97	2.16	-1.15
2851	42.693	0.72	3.3	2.97	2.16	-0.93
2859	42.771	0.76	3.8	2.99	2.18	-0.77
2867	42.847	0.65	2.2	3.23	2.42	-0.97
2875	42.921	0.80	4.4	2.87	2.06	-0.74
2883	42.994	0.78	4.1	3.10	2.29	-0.59
2891	43.069	0.72	3.3	3.11	2.32	-0.78
2903	43.178	1.20	8.3	3.20	2.41	0.62
2913	43.272	0.74	3.6	3.13	2.34	-0.69
2923	43.366	0.68	2.7	3.08	2.29	-0.96
2933	43.459	0.97	6.3	3.00	2.21	-0.10
2958	43.686	0.90	5.5	3.03	2.24	-0.28
2963	43.733	0.94	5.9	2.96	2.17	-0.24
2993	44.010	1.18	8.2	2.94	2.16	0.35
3003	44.105	0.82	4.5	2.73	1.95	-0.82
3008	44.153	0.96	6.1	2.47	1.69	-0.65
3023	44.287	0.92	5.8	2.36	1.58	-0.86
3033	44.377	0.80	4.4	2.75	1.97	-0.84
3043	44.469	0.82	4.6	2.80	2.02	-0.74
3048	44.516	0.84	4.8	2.86	2.08	-0.62
3063	44.653	0.74	3.6	2.92	2.14	-0.88
3083	44.838	0.85	4.9	2.99	2.21	-0.46
3088	44.885	0.89	5.4	3.13	2.35	-0.19
3093	44.931	0.74	3.5	3.05	2.27	-0.77
3103	45.023	0.73	3.3	2.99	2.22	-0.86
3113	45.117	0.79	4.2	2.95	2.18	-0.67
3138	45.348	0.74	3.5	3.30	2.53	-0.50
3188	45.806	1.06	7.1	2.81	2.04	-0.06
3203	45.948	0.88	5.3	2.92	2.15	-0.42
3223	46.134	0.69	2.8	2.83	2.07	-1.17
3233	46.227	1.05	7.0	2.87	2.11	-0.01
3243	46.320	0.82	4.6	2.92	2.16	-0.59
3258	46.463	1.31	9.3	2.83	2.07	0.52
3283	46.697	0.89	5.3	2.84	2.08	-0.47
3293	46.790	0.92	5.7	2.78	2.02	-0.44
3303	46.881	0.93	5.9	2.62	1.86	-0.56
3323	47.065	0.89	5.3	2.51	1.76	-0.80
3333	47.155	1.33	9.4	2.91	2.16	0.63
3338	47.200	1.26	8.9	2.82	2.07	0.42
3348	47.290	0.98	6.3	2.77	2.02	-0.28
3357	47.380	1.30	9.1	2.73	1.98	0.40
3363	47.425	1.11	7.5	2.77	2.02	0.04
3423	47.965	1.18	8.2	2.92	2.17	0.34
3498	48.640	1.19	8.3	2.92	2.17	0.37
3498	48.640	1.19	8.3	2.92	2.17	0.38
3523	48.865	0.91	5.6	2.64	1.89	-0.58
3533	48.955	1.10	7.5	3.09	2.34	0.35

Table A.3
Globigerina bulloides data for MD02-2496

Corrected Depth (cm)	Age kyr	Mg/Ca (mmol/mol)	SST (°C)	$\delta^{18}O_{calcite}$ (VPDB)	Ice volume corrected $\delta^{18}O_{calcite}$ (VPDB)	$\delta^{18}O_{seawater}$ (VSMOW)
407	9.826	1.49	10.5	1.32	0.94	-0.30
497	12.264	1.18	8.2	3.03	2.36	0.54
517	12.702	1.17	8.1	1.96	1.29	-0.56
537	13.082	1.48	10.4	2.08	1.30	0.05
542	13.228	1.57	11.1	2.42	1.64	0.54
547	13.373	1.21	8.5	2.31	1.53	-0.21
562	13.746	1.66	11.6	3.02	2.24	1.27
567	13.868	1.65	11.6	2.82	2.04	1.06
599	14.275	1.37	9.7	2.89	2.02	0.57
602	14.295	1.16	8.0	2.87	2.00	0.14
622	14.412	1.22	8.5	2.96	2.09	0.36
627	14.439	1.27	8.9	3.25	2.38	0.74
662	14.622	1.29	9.1	3.1	2.23	0.63
667	14.649	1.21	8.4	2.8	1.93	0.16
677	14.700	1.24	8.7	3.02	2.15	0.45
682	14.726	0.97	6.2			
697	14.799	1.16	8.1	2.75	1.88	0.02
707	14.847	1.14	7.8	2.79	1.92	0.01
722	14.918	1.39	9.8	2.75	1.88	0.47
747	15.039	1.04	7.0	2.86	1.90	-0.23
797	15.297	1.08	7.3	3.19	2.23	0.18
802	15.323	1.09	7.4	3.11	2.15	0.13
807	15.349	1.28	9.0	2.89	1.93	0.32
812	15.374	1.34	9.4	3	2.04	0.54
817	15.400	1.14	7.9	2.98	2.02	0.12
847	15.564	1.09	7.4	3.22	2.26	0.25
882	15.746	1.20	8.4	3.01	2.05	0.28
897	15.821	1.10	7.4	2.88	1.92	-0.09
902	15.847	0.99	6.5	3.03	2.07	-0.18
927	15.975	1.05	7.0	2.89	1.93	-0.19
942	16.053	1.08	7.3	3.07	2.04	0.00
982	16.258	1.03	6.9	3.43	2.40	0.24
997	16.334	1.00	6.5	3.25	2.22	-0.02
1007	16.383	1.29	9.1	2.93	1.90	0.31
1022	16.456	1.48	10.5	3.1	2.07	0.81
1027	16.481	0.96	6.1	3.22	2.19	-0.16
1037	16.526	1.07	7.2	2.99	1.96	-0.11
1042	16.549	0.92	5.7	3.01	1.98	-0.47
1067	16.643	1.10	7.5	3.21	2.18	0.20
1127	16.861	0.99	6.5	3.26	2.23	-0.03
1137	16.898	0.93	5.8	3.08	2.05	-0.39
1147	16.937	0.90	5.5	2.96	1.93	-0.57
1152	16.954	0.93	5.8	2.92	1.89	-0.53
1157	16.970	0.93	5.9	3.15	2.12	-0.30
1182	17.049	0.96	6.2	2.97	1.89	-0.44
1202	17.109	1.04	6.9	3.41	2.33	0.20
1207	17.124	0.99	6.5	3.4	2.32	0.06
1237	17.214	0.91	5.6			
1247	17.245	1.04	7.0	3.12	2.04	-0.08
1252	17.261	0.97	6.2	3.12	2.04	-0.28
1257	17.276	0.97	6.3	3.19	2.11	-0.19
1262	17.292	0.96	6.1	3.29	2.21	-0.13
1267	17.308	0.93	5.8	2.88	1.80	-0.63
1272	17.323	0.94	5.9	3.39	2.31	-0.09
1277	17.339	1.36	9.6	3.2	2.12	0.66
1282	17.355	1.14	7.9	3.41	2.33	0.44
1302	17.419	0.93	5.8	3.27	2.19	-0.24
1307	17.435	1.09	7.4	3.35	2.27	0.25
1312	17.456	0.88	5.3	3.5	2.42	-0.15
1317	17.479	0.89	5.4	3.12	2.04	-0.49
1322	17.502	0.94	5.9	2.89	1.81	-0.60
1327	17.526	1.06	7.2	3.22	2.14	0.07
1332	17.552	1.05	7.0	3.15	2.07	-0.04
1337	17.580	1.06	7.1	3.18	2.10	0.01
1382	17.822	0.90	5.5	3.31	2.23	-0.29
1387	17.848	1.18	8.2	3.04	1.96	0.14
1427	18.057	1.38	9.8	3.17	2.07	0.65
1432	18.083	1.27	8.9	3.27	2.17	0.54
1437	18.109	0.95	6.1	3	1.90	-0.46
1447	18.161	1.10	7.5	3.13	2.03	0.04
1452	18.187	1.12	7.7	3	1.90	-0.04
1462	18.241	1.29	9.1	3.21	2.11	0.52
1467	18.267	1.02	6.7	2.99	1.89	-0.31
1472	18.296	1.59	11.2	2.79	1.69	0.61
1478	18.331	1.13	7.7	2.97	1.87	-0.06
1487	18.384	1.74	12.1	2.95	1.85	1.00
1492	18.413	1.10	7.5	2.84	1.74	-0.25
1507	18.500	1.20	8.3	2.92	1.82	0.04
1512	18.530	0.91	5.6	2.78	1.68	-0.80
1527	18.620	1.12	7.7	3.13	2.03	0.09
1542	18.707	1.00	6.5	3.21	2.11	-0.14
1552	18.766	0.98	6.3	3.1	2.00	-0.30
1557	18.795	1.02	6.7	2.94	1.84	-0.35
1562	18.826	1.14	7.8	2.95	1.85	-0.05
1567	18.855	1.14	7.9	2.76	1.66	-0.23
1577	18.912	0.97	6.2	3.03	1.93	-0.39
1582	18.941	1.09	7.4	2.7	1.60	-0.40
1607	19.107	0.95	6.0	3.14	2.04	-0.34
1612	19.142	1.08	7.3	2.87	1.77	-0.27
1617	19.177	1.06	7.2	2.91	1.81	-0.27
1632	19.283	0.79	4.1	2.74	1.64	-1.23
1637	19.319	0.99	6.5	2.76	1.66	-0.59
1652	19.437	0.95	6.1	2.94	1.84	-0.52
1662	19.538	1.22	8.5	2.95	1.85	0.12
1677	19.784	1.73	12.0	2.74	1.64	0.77
1682	19.887	1.07	7.3	2.81	1.71	-0.35
1692	20.094	1.07	7.2	3.07	1.98	-0.09
1697	20.200	1.30	9.2	2.77	1.68	0.11
1702	20.305	1.12	7.6	2.81	1.72	-0.24
1707	20.410	1.13	7.8	3.01	1.92	0.00
1717	20.624	1.30	9.2	2.53	1.44	-0.14
1727	20.839	1.50	10.6	2.95	1.86	0.63
1737	21.047	1.10	7.5	2.84	1.76	-0.24
1747	21.255	1.24	8.7	2.71	1.63	-0.06
1757	21.475	1.37	9.7	2.97	1.89	0.45
1767	21.700	1.06	7.1	2.87	1.79	-0.31
1777	21.927	1.02	6.7	2.97	1.89	-0.30
1787	22.150	1.01	6.6	3.16	2.11	-0.10
1797	22.364	1.01	6.6	2.74	1.69	-0.53
1807	22.581	1.13	7.7	2.82	1.77	-0.17
1817	22.805	1.21	8.4	2.99	1.94	0.18
1827	23.030	0.93	5.8	3.13	2.11	-0.32
1837	23.252	0.97	6.2	2.76	1.74	-0.57
1847	23.474	1.20	8.3	2.78	1.76	-0.02
1857	23.700	1.25	8.7	2.68	1.66	-0.02
1867	23.928	1.09	7.4	2.83	1.81	-0.21
1877	24.134	1.18	8.2	2.85	1.87	0.06
1887	24.336	1.16	8.0	3.35	2.37	0.51
1897	24.535	1.31	9.3	2.82	1.84	0.29
1907	24.733	1.09	7.4	2.93	1.95	-0.06
1917	24.938	1.15	7.9	2.69	1.71	-0.18
1927	25.139	1.12	7.7	2.8	1.86	-0.10
1937	25.336	1.40	9.9	3.02	2.08	0.68
1947	25.532	1.01	6.6	2.89	1.95	-0.28
1992	26.356	1.09	7.4	3.23	2.32	0.30
2027	26.801	0.97	6.2	2.82	1.91	-0.41
2037	26.926	1.02	6.7	2.99	2.08	-0.12
2047	27.053	1.07	7.2	2.63	1.74	-0.34
2057	27.227	0.86	5.0	3.15	2.26	-0.38
2062	27.318	0.98	6.3	2.18	1.29	-1.00
2067	27.408	1.05	7.0	2.43	1.54	-0.58
2082	27.619	1.31	9.2	2.91	2.02	0.46
2087	27.689	1.13	7.8	3.14	2.25	0.33
2097	27.830	1.38	9.8	2.9	2.01	0.58
2112	28.040	0.99	6.5	2.99	2.11	-0.15
2120	28.148	0.89	5.4	2.74	1.86	-0.68
2124	28.204	1.02	6.7	2.55	1.67	-0.53
2140	28.461	1.17	8.1	3.05	2.17	0.32
2152	28.661	0.95	6.0	2.92	2.04	-0.33
2172	29.001	1.04	6.9	3.24	2.37	0.22
2180	29.137	1.21	8.4	3.03	2.16	0.40
2272	31.180	0.85	4.9	3.08	2.22	-0.45
2284	31.553	1.06	7.1	2.87	2.01	-0.09
2341	33.653	0.96	6.1	2.68	1.82	-0.52
2363	34.532	1.15	8.0	2.92	2.06	0.19
2371	34.849	1.02	6.7	2.6	1.74	-0.45
2383	35.320	1.17	8.1	2.3	1.44	-0.40
2523	38.162	1.02	6.8	2.19	1.34	-0.85
2563	38.926	1.18	8.2	1.86	1.01	-0.81
2583	39.228	1.28	9.0	2.7	1.86	0.24
2615	39.677	1.02	6.7	3.04	2.20	0.01
2623	39.790	0.87	5.1	3.1	2.26	-0.35
2655	40.242	1.09	7.4	3.02	2.19	0.18
2703	40.904	1.16	8.0	2.8	1.97	0.11
2723	41.181	1.17	8.1	2.7	1.88	0.05
2763	41.686	0.83	4.7	2.56	1.74	-0.97
2787	41.961	1.27	8.9	2.96	2.14	0.51
2803	42.146	1.07	7.2	3.07	2.26	0.20
2883	42.994	1.06	7.2	3.3	2.49	0.41
2891	43.069	0.96	6.1	3.18	2.39	0.04
2903	43.178	1.01	6.7	3.24	2.45	0.24
2913	43.272	1.03	6.9	3.21	2.42	0.26
2933	43.459	1.27	8.9	3.25	2.46	0.82
2973	43.826	1.15	7.9	2.87	2.08	0.19
2983	43.917	1.05	7.1	3.04	2.25	0.14
2993	44.010	1.17	8.1			
3003	44.105	1.04	6.9	3.08	2.30	0.16
3023	44.287	1.10	7.5	2.05	1.27	-0.73
3033	44.377	1.20	8.3	2.99	2.21	0.43
3093	44.931	0.97	6.3	3.17	2.39	0.08
3103	45.023	0.99	6.5	3.02	2.25	0.00
3143	45.395	0.99	6.5	3	2.23	-0.03
3223	46.134	0.95	6.1	2.87	2.11	-0.25
3233	46.227	1.03	6.8	2.93	2.17	0.00
3243	46.320	1.08	7.3	3.01	2.25	0.20
3253	46.415	1.32	9.3	3.03	2.27	0.74
3258	46.463	0.95	6.0	2.97	2.21	-0.17
3273	46.604	1.14	7.9	2.78	2.02	0.13
3283	46.697	1.25	8.8	2.96	2.20	0.53
3333	47.155	1.01	6.6	2.99	2.24	0.02
3338	47.200	1.16	8.0	2.89	2.14	0.27
3348	47.290	1.04	7.0	2.92	2.17	0.04
3357	47.380	1.72	11.9	2.63	1.88	0.99
3363	47.425	1.47	10.4	2.94	2.19	0.91
3378	47.560	1.50	10.6	2.94	2.19	0.97
3498	47.740	1.69	11.8	2.92	2.17	1.24
3508	48.730	1.45	10.3	2.86	2.11	0.81
3518	48.820	1.57	11.1	2.94	2.19	1.09
3523	48.865	1.28	9.0	3.08	2.33	0.72
3533	48.955	0.94	6.0	2.73	1.98	-0.41
3538	49.000	1.39	9.8	2.92	2.18	0.77

Appendix B

Supplementary Table for Chapter 4

Table B.1
Concentrations of grain size diameters from core S4, CAA

Core depth (cm)	1-2 μm (ppb)	1-5 μm (ppb)	1-10 μm (ppb)	1-20 μm (ppb)	1-30 μm (ppb)
0	37.4	120.1	185.9	232.6	252.3
9	23.4	68.8	113.6	176.4	201.5
18	26.4	120.2	217.5	328.8	356.2
27	33.6	100.1	154.5	272.0	305.7
36	16.0	51.8	87.3	126.4	137.0
45	11.8	35.1	53.4	63.3	84.5
54	11.2	35.0	58.7	82.5	82.5
63	9.4	31.8	66.9	115.4	136.8
72	20.2	62.6	110.1	160.6	176.1
81	6.1	15.0	26.7	41.2	41.2
90	17.2	56.8	114.0	173.4	191.8
99	9.1	26.2	44.0	68.7	68.7
108	9.4	25.6	46.0	68.2	68.2
117	12.8	28.8	45.9	77.3	77.3
126	21.4	69.4	114.0	166.2	173.0
135	19.9	48.3	69.3	102.3	102.3
144	26.9	81.1	131.4	224.3	230.6
153	23.4	64.2	95.4	137.1	137.1
162	27.1	66.8	97.9	133.8	133.8
171	12.5	46.1	85.5	160.7	175.8
180	18.2	49.1	80.0	150.8	170.5
189	27.8	78.3	118.6	153.3	168.2
198	24.8	100.0	197.7	314.7	345.0
207	8.9	24.4	32.3	36.4	36.4
216	12.3	47.5	84.1	107.0	107.0
225	11.5	31.5	48.6	58.2	58.2
234	8.5	28.0	47.5	60.7	69.1

Table B.2
Concentrations of grain size diameters from core S3, CAA

Core depth (cm)	1-2 µm (ppb)	1-5 µm (ppb)	1-10 µm (ppb)	1-20 µm (ppb)	1-30 µm (ppb)
0	51.7	235.1	496.4	721.1	781.8
9	123.5	372.7	687.6	868.0	888.8
18	162.6	601.8	1316.8	1963.8	2050.0
36	24.9	123.1	256.8	400.6	412.1
45	64.8	239.0	449.0	726.5	829.5
54	142.4	494.8	809.0	1160.2	1247.8
63	52.1	201.7	461.2	843.3	911.8
72	52.0	177.5	302.4	419.1	432.2
81	84.0	352.5	723.2	1203.1	1405.1
90	24.6	108.4	243.3	409.6	440.2
99	128.6	355.4	529.8	689.7	698.4
108	161.8	461.5	754.9	1039.0	1061.3
117	85.0	244.3	392.2	552.4	572.8
126	113.7	303.3	424.4	544.0	552.9
135	101.5	320.6	453.6	557.7	593.1
144	102.9	280.6	413.3	580.8	594.6
153	44.2	156.4	260.2	358.8	387.1
162	23.6	82.5	146.6	198.3	198.3
171	29.0	118.4	228.1	371.7	437.3
190	43.6	126.4	198.9	275.9	299.4
189	201.9	622.3	889.7	1027.6	1034.0

Table B.3
Labile elemental data for core S2, Point Barrow, AK

Core depth (cm)	Grain size (μm)	Si (nM)	Ti (nM)	Al (nM)	Fe (nM)	Mn (nM)	Mg (nM)	Ca (nM)	K (nM)	P (nM)	Cd (nM)	Co (nM)	Cr (nM)	Cu (nM)	Mo (nM)	Ni (nM)	Zn (nM)
5	0.2 - 5	2224.8	16.7	211.7	357.6	19.4	20103.9	0.0	0.0	515.6	0.1	0.2	1.7	7.5	0.0	0.1	4.0
20	0.2 - 5	0.0	10.1	0.0	84.4	1.1	11272.6	0.0	0.0	0.0	0.0	0.0	9.5	3.5	0.0	0.0	0.0
63.5	0.2 - 5	1200.0	12.0	26.1	51.1	1.2	16928.6	6455.9	7013.5	77.9	0.0	0.2	0.5	6.5	0.0	0.0	7.3
90	0.2 - 5	98282.5	10.1	110.9	153.0	3.2	15679.6	226210.2	62607.6	35860.9	0.0	0.0	0.0	3.7	0.0	0.0	0.0
113	0.2 - 5	2202.7	10.8	256.8	484.7	21.0	14019.6	8651.5	8697.9	131.2	0.1	0.7	2.6	11.7	0.0	0.1	3.3
127	0.2 - 5	1165.9	3.8	0.0	115.8	8.6	5303.7	12021.7	13124.3	105.3	0.0	0.0	0.2	0.7	0.0	0.0	0.0
Seawater	0.2 - 5	1434.9	0.0	0.0	0.0	0.0	0.0	7752.3	7782.7	106.1	0.0	0.0	0.0	0.0	0.0	0.0	0.0
5	5 - 10	1100.3	12.8	0.0	39.7	2.1	20046.9	0.0	0.0	282.5	0.0	0.0	0.0	13.2	0.0	3.7	4.2
20	5 - 10	18686.9	13.6	17.9	68.7	1.9	10174.5	31141.3	22147.4	2697.2	0.0	0.0	0.3	2.0	0.0	0.0	0.2
63.5	5 - 10	1684.1	6.8	0.0	0.0	0.0	10866.2	8920.3	8476.7	243.1	0.0	0.3	0.0	0.0	0.0	0.0	0.0
90	5 - 10	32860.4	13.6	0.0	12.8	1.0	19757.6	46161.3	23782.9	2715.4	0.0	0.0	0.0	0.6	0.0	0.0	0.0
113	5 - 10	2580.0	3.0	0.0	54.5	6.7	5086.3	35543.8	36635.4	311.8	0.0	0.0	0.0	0.0	0.0	0.0	0.0
127	5 - 10	1097.5	6.7	0.0	115.9	8.8	9339.6	0.0	0.0	131.9	0.0	0.0	1.2	1.1	0.0	0.0	0.0
Seawater	5 - 10	1583.6	0.0	0.0	0.0	0.0	0.0	10100.7	9504.0	280.2	0.0	0.0	0.0	0.0	0.0	0.0	0.0
5	10 - 30	1724.4	84.8	2930.2	4739.1	204.9	53465.7	9587.6	9495.3	223.8	0.3	3.4	27.6	18.1	0.2	3.8	36.3
20	10 - 30	0.0	446.3	10882.5	15342.7	524.8	53115.4	0.0	0.0	0.0	0.5	7.5	50.1	56.3	0.9	9.8	85.2
63.5	10 - 30	1135.0	65.5	2482.8	4625.6	357.8	55196.7	9364.3	9172.9	80.9	0.3	4.4	10.5	38.9	0.3	2.8	57.9
90	10 - 30	1187.6	218.2	23033.0	76297.3	7439.1	83999.8	8395.0	8816.4	148.4	1.4	41.9	19.7	114.1	0.7	26.6	206.7
113	10 - 30	0.0	1010.4	64547.9	218342.7	21480.2	209643.5	0.0	0.0	0.0	38.3	133.3	110.3	253.8	1.5	125.3	776.2
127	10 - 30	12955.6	39.5	1211.7	1530.7	62.1	32984.1	58224.9	34852.3	1835.2	0.4	1.2	9.1	11.9	0.2	1.7	13.4
Seawater	10 - 30	15168.3	0.0	0.0	0.0	0.0	0.0	37834.7	33221.5	1036.7	0.0	0.0	0.0	0.0	0.0	0.0	0.0
5	> 30	842.0	9.7	0.0	0.0	0.2	14609.3	0.0	0.0	25.9	0.0	0.0	0.0	0.3	0.0	0.9	0.0
20	> 30	0.0	19.2	232.8	292.7	5.2	18029.6	0.0	0.0	0.0	0.0	0.1	0.0	1.4	0.0	0.0	14.0
63.5	> 30	1088.1	21.8	3.2	0.0	0.7	24095.1	11200.8	11378.2	144.8	0.0	0.0	0.0	0.1	0.0	0.0	1.1
90	> 30	1214.7	36.7	2614.9	6276.7	530.2	25231.4	3097.8	3299.7	146.7	0.1	8.3	3.4	16.6	0.1	2.3	27.0
113	> 30	79240.0	62.7	3665.5	95782.1	3053.3	23597.6	1244830.7	132739.4	80055.2	0.8	106.7	27938.1	942.0	74.9	15140.3	693.4
127	> 30	1312.5	24.6	0.0	1455.1	34.4	32663.6	1930.2	1609.8	209.2	0.1	1.2	383.7	11.8	1.3	173.9	8.5
Seawater	> 30	1932.7	0.0	0.0	0.0	0.0	0.0	7796.2	7079.1	393.7	0.0	0.0	0.0	0.0	0.0	0.0	0.0

Table B.4
Total elemental data for core S2, Point Barrow, AK

Core depth (cm)	Grain size (μm)	Si (nM)	Ti (nM)	Al (nM)	Fe (nM)	Mn (nM)	Mg (nM)	Ca (nM)	K (nM)	P (nM)	Cd (nM)	Co (nM)	Cr (nM)	Cu (nM)	Mo (nM)	Ni (nM)	Zn (nM)
5	0.2 - 5	3383.6	17.2	346.3	357.6	19.4	20121.7	8920.3	8476.7	54.5	0.1	0.2	1.7	7.8	0.0	0.1	4.0
20	0.2 - 5	1811.6	10.1	0.0	84.4	1.1	11272.6	4879.5	4920.1	127.2	0.0	0.0	9.5	4.9	0.0	0.0	0.0
63.5	0.2 - 5	2457.1	12.4	26.1	51.1	1.2	16945.8	7752.3	7782.7	173.1	0.0	0.2	0.5	6.5	0.0	0.0	7.3
90	0.2 - 5	2486.1	16.8	257.9	156.6	3.2	15692.1	9587.6	9495.3	343.4	0.0	0.0	0.0	4.1	0.0	0.0	0.0
113	0.2 - 5	2997.4	15.9	354.1	484.7	21.0	14034.5	7796.2	7079.1	597.4	0.1	0.7	2.6	11.7	0.0	0.1	3.9
127	0.2 - 5	2829.9	8.2	91.5	115.8	8.6	5317.0	5874.1	5374.7	348.1	0.0	0.0	0.2	0.7	0.0	0.0	0.9
Seawater	0.2 - 5	2112.9	0.0	0.0	0.0	0.0	0.0	0.0	0.0	445.7	0.0	0.0	0.0	0.0	0.0	0.0	0.0
5	5 - 10	4485.1	22.8	136.4	72.9	2.2	20088.8	8395.0	8816.4	221.8	0.0	0.0	0.0	13.2	0.0	3.7	17.1
20	5 - 10	2395.0	13.6	17.9	68.7	1.9	10181.6	7999.2	4735.8	161.1	0.0	0.0	0.3	2.6	0.0	0.0	0.2
63.5	5 - 10	1983.9	6.8	18.5	22.9	0.0	10919.4	5460.6	6528.5	105.7	0.0	0.3	0.0	2.1	0.0	0.0	21.4
90	5 - 10	2024.5	13.6	0.0	12.8	1.0	19757.6	9364.3	9172.9	165.1	0.0	0.0	0.0	0.6	0.0	0.0	0.0
113	5 - 10	2096.9	3.0	0.0	54.5	6.7	5086.7	3097.8	3299.7	265.8	0.0	0.0	0.0	0.1	0.0	0.0	0.0
127	5 - 10	2493.4	7.1	15.2	115.9	8.8	9343.2	10100.7	9504.0	339.6	0.0	0.0	1.2	1.1	0.0	0.0	0.0
Seawater	5 - 10	1939.7	0.0	0.0	0.0	0.0	0.0	0.0	0.0	182.5	0.0	0.0	0.0	0.0	0.0	0.0	0.0
5	10 - 30	13921.3	86.4	2930.2	33029.0	1148.6	53492.6	58224.9	36579.4	1905.5	0.4	38.0	8955.0	276.0	23.3	5159.9	285.5
20	10 - 30	37038.1	532.8	13224.1	16085.2	530.9	53311.5	49365.2	29314.2	4179.8	0.5	7.7	50.1	57.1	0.9	9.8	98.6
63.5	10 - 30	10162.6	224.8	5292.1	5511.6	364.2	55604.2	35496.7	29378.5	1661.1	0.3	4.7	10.5	39.9	0.4	2.8	59.5
90	10 - 30	99703.2	3603.4	64394.5	100535.5	7599.3	86027.8	227673.4	122321.9	37498.9	1.4	49.7	84.8	126.8	1.1	47.8	246.8
113	10 - 30	80655.0	16942.4	515442.9	351250.1	22558.8	271873.4	1299239.6	605357.9	98468.2	38.9	173.8	486.6	310.5	4.1	246.0	980.0
127	10 - 30	16161.4	52.7	1301.5	1597.1	62.1	32993.9	37834.7	33221.5	1125.4	0.4	1.2	9.1	12.1	0.2	1.7	13.5
Seawater	10 - 30	3217.7	0.0	0.0	0.0	0.0	0.0	0.0	0.0	586.5	0.0	0.0	0.0	0.0	0.0	0.0	0.0
5	> 30	2173.4	11.4	0.0	1849.7	67.8	14668.4	6455.9	7013.5	111.3	0.0	2.6	562.7	22.8	5.4	391.1	18.6
20	> 30	3685.5	19.2	232.8	292.7	5.2	18029.9	8651.5	8697.9	197.5	0.0	0.1	0.0	1.6	0.0	0.0	73.9
63.5	> 30	2045.4	21.8	3.2	0.0	0.7	24095.1	12021.7	13124.3	147.6	0.0	0.0	0.0	0.2	0.0	0.0	1.1
90	> 30	19823.1	96.7	3442.6	6802.3	532.1	25319.0	31141.3	24513.5	2809.6	0.1	8.4	3.4	17.1	0.1	2.3	27.1
113	> 30	34122.6	96.1	5589.2	96224.3	3055.5	23904.0	46161.3	27211.4	3026.0	0.8	106.8	27938.1	942.2	74.9	15140.3	693.4
127	> 30	3509.5	24.8	0.0	1455.1	34.4	32667.7	35543.8	36635.4	365.7	0.1	1.2	383.7	13.3	1.3	173.9	8.5
Seawater	> 30	2059.8	0.0	0.0	0.0	0.0	0.0	0.0	0.0	221.8	0.0	0.0	0.0	0.0	0.0	0.0	0.0

Table B.5
Labile elemental data for core S1, Point Barrow, AK

Core depth (cm)	Grain size (μm)	Si (nM)	Ti (nM)	Al (nM)	Fe (nM)	Mn (nM)	Mg (nM)	Ca (nM)	K (nM)	P (nM)	Cd (nM)	Co (nM)	Cr (nM)	Cu (nM)	Mo (nM)	Ni (nM)	Zn (nM)
Snow	0.2 - 5	36054.8	3.5	222.2	311.1	1.3	4662.4	49365.2	27421.9	4087.4	0.0	0.1	1.2	8.1	0.0	0.3	1.4
5	0.2 - 5	9171.3	15.2	0.0	9807.4	246.9	8489.3	35496.7	27475.5	1539.9	0.0	9.5	2770.9	85.0	14.4	1387.2	72.4
34.5	0.2 - 5	3982.7	4.8	0.0	0.0	0.0	7847.5	19079.7	10214.2	650.0	0.0	0.0	0.0	0.0	0.0	0.0	0.0
59	0.2 - 5	24455.6	3.4	0.0	371.0	8.6	4073.7	23712.6	9630.3	90.6	0.0	0.3	109.2	2.7	0.7	46.2	1.2
106	0.2 - 5	915.2	5.1	0.0	0.0	0.0	8541.8	6706.8	5919.3	251.0	0.0	0.0	0.0	3.3	0.0	0.0	0.0
Snow	5 - 10	1853.3	4.7	0.0	0.0	0.0	7295.5	6628.0	5617.1	239.6	0.0	0.0	0.0	1.1	0.0	0.0	4.5
5	5 - 10	1432.1	36.3	1486.8	3354.3	130.7	27747.0	7999.2	4735.8	105.9	0.1	1.1	0.3	4.5	0.1	0.0	13.2
34.5	5 - 10	1007.8	11.0	47.6	210.4	18.8	13911.2	7732.1	6665.4	343.4	0.0	0.2	0.6	0.0	0.0	0.0	0.2
59	5 - 10	1098.9	11.5	0.0	3297.8	120.9	15251.7	5252.9	3685.5	217.1	0.0	5.0	946.0	43.6	4.8	713.3	36.1
106	5 - 10	1199.5	5.8	0.0	31.8	0.0	9516.4	10458.6	11168.7	285.9	0.0	0.0	0.0	0.0	0.0	0.0	0.0
Snow	10 - 30	1076.2	38.2	5941.5	2278.6	36.7	24591.0	5460.6	6528.5	50.1	1.5	4.2	18.2	30.1	0.3	4.6	26.4
5	10 - 30	0.0	3.5	0.0	0.0	0.0	5781.0	0.0	0.0	0.0	0.0	0.0	0.0	0.0	0.1	1.7	0.0
34.5	10 - 30	4214.5	5.4	0.0	0.0	0.5	7168.7	11649.7	7457.0	127.8	0.0	0.0	0.0	0.0	0.0	0.9	0.0
59	10 - 30	0.0	4.7	0.0	142.8	11.5	4891.8	0.0	0.0	0.0	0.0	0.0	0.0	0.0	0.0	0.0	0.0
106	10 - 30	11631.0	6.0	0.0	0.0	1420.7	0.0	40093.4	37422.7	364.8	204.5	1.8	87.9	17.6	0.4	104.7	0.0
Snow	> 30	1416.2	27.2	1025.7	313.3	4.0	15939.1	5874.1	5374.7	198.9	0.1	0.7	2.8	3.0	0.1	2.4	3.6
5	> 30	2595.6	26.9	777.2	522.7	9.8	26983.4	3221.9	2907.6	66.7	0.0	0.0	0.0	0.0	0.0	0.0	0.3
34.5	> 30	962.1	19.5	278.6	54.8	3.2	23821.1	0.0	0.0	143.8	0.0	0.3	1.1	0.0	0.0	0.0	0.0
59	> 30	2418.4	12.1	0.0	0.0	0.1	16933.4	16501.3	16184.9	150.3	0.0	0.0	0.0	0.0	0.0	0.0	0.0
106	> 30	3776.6	2.2	0.0	0.0	1488.2	0.0	45997.1	44864.8	277.4	54.6	0.5	20.5	0.0	0.0	18.7	0.0

Table B.6
Total elemental data for core S1, Point Barrow, AK

Core depth (cm)	Grain size (μm)	Si (nM)	Ti (nM)	Al (nM)	Fe (nM)	Mn (nM)	Mg (nM)	Ca (nM)	K (nM)	P (nM)	Cd (nM)	Co (nM)	Cr (nM)	Cu (nM)	Mo (nM)	Ni (nM)	Zn (nM)
Snow	0.2 - 5	2414.2	4.8	302.2	322.2	1.6	4681.7	1930.2	1609.8	300.1	0.0	0.1	1.2	9.8	0.0	0.3	1.5
5	0.2 - 5	25509.7	15.2	0.0	10054.3	261.8	8514.1	23712.6	9630.3	133.6	0.0	10.0	2856.4	89.3	14.7	1476.3	75.9
34.5	0.2 - 5	2818.6	4.8	0.0	0.0	0.0	7847.5	7732.1	6665.4	425.7	0.0	0.0	0.0	0.0	0.0	0.0	0.0
59	0.2 - 5	2041.4	3.4	0.0	371.0	8.6	4073.7	5252.9	3685.5	295.5	0.0	0.3	109.2	2.7	0.7	46.2	1.2
106	0.2 - 5	2351.5	5.1	0.0	0.0	0.0	8549.5	10458.6	11168.7	368.5	0.0	0.0	0.0	3.3	0.0	0.0	0.0
Snow	5 - 10	3609.1	4.7	0.0	0.0	0.0	7306.0	3221.9	2907.6	171.5	0.0	0.0	0.0	1.4	0.0	0.0	4.5
5	5 - 10	22100.8	156.0	1742.4	4298.4	133.5	27762.3	65146.3	38061.4	3993.9	0.1	1.1	-20.4	4.5	0.1	0.0	13.2
34.5	5 - 10	3920.6	11.0	47.6	210.4	18.8	13911.2	19801.9	18662.9	382.8	0.0	0.2	0.6	0.0	0.0	0.0	0.2
59	5 - 10	21232.8	11.5	0.0	3297.8	120.9	15251.7	17592.6	17718.5	293.3	0.0	5.0	946.0	43.6	4.8	713.3	36.1
106	5 - 10	2398.7	5.8	0.0	31.8	0.0	9577.6	11200.8	11378.2	174.5	0.0	0.0	0.0	0.0	0.0	0.0	0.0
Snow	10 - 30	5268.7	103.9	6218.0	2918.7	39.0	24635.8	19079.7	10214.2	726.5	1.6	4.4	18.2	31.3	0.4	4.6	27.3
5	10 - 30	1849.6	3.5	0.0	0.0	0.0	5781.0	6706.8	6258.9	312.6	0.0	0.0	0.0	0.0	0.1	1.7	0.0
34.5	10 - 30	2009.9	5.4	0.0	0.0	0.5	7168.7	7783.1	7577.0	157.3	0.0	0.0	0.0	0.0	0.0	0.9	0.0
59	10 - 30	2871.2	4.9	0.0	142.8	12.7	4891.8	6628.0	5617.1	310.6	0.0	0.0	7.0	0.0	0.0	4.4	0.0
106	10 - 30	6373.0	6.0	0.0	0.0	1420.7	0.0	34008.7	29610.4	1043.4	204.5	1.8	87.9	17.6	0.4	104.7	0.0
Snow	> 30	5394.1	118.8	1768.9	1130.0	7.1	16005.9	11649.7	7457.0	168.2	0.1	0.9	2.8	3.7	0.1	2.4	4.3
5	> 30	12648.9	26.9	777.2	522.7	9.8	26983.4	40093.4	37422.7	393.7	0.0	0.0	0.0	0.0	0.0	0.0	0.3
34.5	> 30	4823.9	20.1	278.6	57.9	3.2	23828.6	31785.6	29398.4	309.1	0.0	0.3	11.1	0.0	0.3	0.0	0.0
59	> 30	3614.1	12.1	0.0	0.0	0.1	16933.4	16501.3	16184.9	185.7	0.0	0.0	0.0	0.0	0.0	0.0	0.0
106	> 30	4741.3	4.4	0.0	0.0	1488.2	47.9	45997.1	44864.8	324.2	54.6	0.5	20.5	0.0	0.0	18.7	0.0

Table B.7
Labile elemental data for core S4, CAA

Core depth (cm)	Grain size (μm)	Si (nM)	Ti (nM)	Al (nM)	Fe (nM)	Mn (nM)	Mg (nM)	Ca (nM)	K (nM)	P (nM)	Cd (nM)	Co (nM)	Cr (nM)	Cu (nM)	Mo (nM)	Ni (nM)	Zn (nM)
Snow	0.2 - 5	11665.0	0.0	15.9	42.3	2.5	28.5	0.0	0.0	117.5	0.0	0.0	3.3	0.0	0.0	1.9	0.0
10	0.2 - 5	598.9	0.0	0.0	0.0	0.0	0.0	0.0	0.0	94.7	0.0	0.0	0.0	0.0	0.0	0.0	0.0
20	0.2 - 5	1920.6	1.1	0.0	0.0	0.0	1740.5	1846.0	1583.3	182.4	0.0	0.0	0.0	0.0	0.0	0.0	0.0
117	0.2 - 5	2545.7	0.0	0.0	0.0	0.0	1291.9	1682.9	1236.9	105.6	0.0	0.0	0.0	0.0	0.0	0.0	0.0
176	0.2 - 5	25889.6	0.0	0.0	0.0	0.0	1849.0	1938.6	1771.9	88.5	0.0	0.0	0.0	0.0	0.0	0.0	0.0
227	0.2 - 5	778.1	0.0	0.0	0.0	0.0	2292.0	2119.1	2071.6	157.7	0.0	0.0	0.0	0.4	0.0	0.0	0.0
Seawater	0.2 - 5	887.7	0.0	0.0	0.0	0.0	0.0	0.0	0.0	120.0	0.0	0.0	0.0	0.0	0.0	0.0	0.0
Snow	5 - 10	13561.8	0.0	0.0	24.7	2.3	8.8	0.0	0.0	217.2	0.0	0.0	3.2	0.0	0.0	1.5	0.0
10	5 - 10	9231.8	0.0	0.0	0.0	0.0	0.0	0.0	0.0	88.0	0.0	0.0	0.0	0.0	0.0	0.0	0.0
20	5 - 10	35661.0	0.1	0.0	0.0	0.0	1486.5	1665.0	1444.1	84.3	0.0	0.0	0.0	0.0	0.0	0.0	0.0
117	5 - 10	1021.8	3.6	0.0	7970.7	484.0	552.1	4047.2	9136.6	205.3	0.3	35.9	2334.0	52.7	126.2	2347.6	14627.7
176	5 - 10	30579.9	0.0	0.0	0.0	0.0	1670.7	1827.6	1580.1	103.2	0.0	0.0	0.0	0.0	0.0	0.0	0.0
227	5 - 10	14229.6	0.0	0.0	18.2	0.0	940.6	1032.7	849.8	146.7	0.0	0.0	7.2	0.0	0.0	2.7	0.0
Seawater	5 - 10	935.0	0.0	0.0	0.0	0.0	0.0	0.0	0.0	112.9	0.0	0.0	0.0	0.0	0.0	0.0	0.0
Snow	10 - 30	21029.1	66.2	6233.1	2330.6	18.1	1529.5	1494.1	2251.4	314.3	0.0	0.5	4.1	4.5	0.1	2.6	3.6
10	10 - 30	15609.9	8.6	1986.3	754.8	9.8	1164.0	3076.8	979.1	573.2	0.3	1.9	55.7	8.2	2.5	27.2	2178.8
20	10 - 30	27659.5	3.3	222.3	148.8	3.2	5069.2	7966.4	5458.7	179.1	0.0	0.0	1.4	4.9	0.0	1.7	0.0
117	10 - 30	28973.9	9.2	547.5	75.7	2.1	8785.2	18536.1	8906.9	368.9	0.0	0.0	1.3	2.3	0.0	1.9	0.0
176	10 - 30	31647.1	12.1	70.0	193.8	3.8	12540.2	16787.3	12869.6	257.1	0.0	0.0	3.5	1.8	0.0	2.4	0.0
227	10 - 30	1309.5	3.7	0.0	8.3	0.2	6368.1	7963.9	6782.4	373.6	0.1	0.0	0.2	1.0	0.0	0.0	0.0
Seawater	10 - 30	1742.3	0.0	0.0	0.0	0.0	0.0	0.0	0.0	218.3	0.0	0.0	0.0	0.0	0.0	0.0	0.0
Snow	> 30	14346.3	2.2	312.1	112.7	0.3	83.7	0.0	229.5	207.6	0.0	0.0	0.0	0.0	0.0	0.0	0.0
10	> 30	15945.7	24.6	2373.8	319.1	2.8	1785.1	12269.3	477.3	308.1	0.1	0.0	43.6	7.4	0.0	2.1	0.0
20	> 30	34156.7	7.5	365.8	87.9	3.4	11337.4	17135.4	12409.5	276.0	0.0	0.0	2.2	3.5	0.0	1.1	0.0
117	> 30	33316.3	12.0	928.4	54.5	2.1	9834.1	17133.6	8009.7	640.0	0.0	0.0	1.6	2.5	0.0	0.7	0.0
176	> 30	48167.7	11.1	131.7	92.3	3.0	13226.1	16561.3	11871.8	328.8	0.0	0.0	2.1	2.2	0.0	1.7	0.0
227	> 30	27005.7	6.2	0.0	0.0	0.3	10488.6	13244.7	10462.9	359.8	0.0	0.0	0.0	0.4	0.0	0.0	0.0
Seawater	> 30	1584.3	0.0	0.0	0.0	0.0	0.0	0.0	0.0	168.4	0.0	0.0	0.0	0.0	0.0	0.0	0.0

Table B.8
Total elemental data for core S4, CAA

Core depth (cm)	Grain size (μm)	Si (nM)	Ti (nM)	Al (nM)	Fe (nM)	Mn (nM)	Mg (nM)	Ca (nM)	K (nM)	P (nM)	Cd (nM)	Co (nM)	Cr (nM)	Cu (nM)	Mo (nM)	Ni (nM)	Zn (nM)
Snow	0.2 - 5	12459.3	0.7	111.7	42.3	2.5	53.8	0.0	0.0	296.8	0.0	0.0	3.3	0.1	0.0	1.9	0.0
10	0.2 - 5	1205.0	0.0	14.2	183.4	5.8	7.2	0.0	379.9	307.7	0.0	1.1	49.7	0.6	2.6	26.2	1006.9
20	0.2 - 5	2938.7	1.1	0.0	0.0	0.0	1758.6	1846.0	1583.3	282.1	0.0	0.0	0.0	0.0	0.0	0.0	0.0
117	0.2 - 5	3026.8	0.0	0.0	0.0	0.0	1302.4	1682.9	1236.9	228.7	0.0	0.0	0.0	0.0	0.0	0.0	0.0
176	0.2 - 5	26499.4	0.0	0.0	0.0	0.2	1858.1	1938.6	1771.9	240.7	0.0	0.0	13.8	0.0	0.2	0.0	0.0
227	0.2 - 5	1885.3	0.0	0.0	806.9	18.1	2292.0	2119.1	2071.6	261.4	0.0	0.6	284.0	4.5	1.4	105.7	0.0
Seawater	0.2 - 5	1795.0	0.0	0.0	0.0	0.0	0.0	0.0	0.0	190.1	0.0	0.0	0.0	0.0	0.0	0.0	0.0
Snow	5 - 10	14357.8	0.0	0.0	24.7	2.3	8.8	0.0	0.0	320.4	0.0	0.0	3.2	0.0	0.0	1.5	0.0
10	5 - 10	9919.3	0.0	0.0	0.0	0.0	29.1	0.0	0.0	217.0	0.0	0.0	0.0	0.0	0.0	0.0	0.0
20	5 - 10	36786.8	0.1	0.0	1763.6	37.0	1492.0	1665.0	1444.1	195.0	0.0	1.4	524.7	12.0	2.4	225.5	0.0
117	5 - 10	1827.8	3.6	0.0	7970.7	484.0	570.6	4047.2	9136.6	305.2	0.3	35.9	2334.0	52.7	126.2	2347.6	14627.7
176	5 - 10	31340.1	1.3	0.0	3694.4	78.3	1689.4	1827.6	1580.1	266.3	0.0	3.0	1029.2	27.4	5.7	472.1	21.0
227	5 - 10	15216.1	0.0	0.0	18.2	0.0	952.3	1032.7	849.8	254.4	0.0	0.0	7.2	0.0	0.0	2.7	0.0
Seawater	5 - 10	2012.3	0.0	0.0	0.0	0.0	0.0	0.0	0.0	228.2	0.0	0.0	0.0	0.0	0.0	0.0	0.0
Snow	10 - 30	22090.4	72.0	6287.9	3618.4	45.9	1535.5	1494.1	2251.4	434.2	0.0	1.5	376.0	14.3	1.5	152.6	3.6
10	10 - 30	16372.3	12.8	2133.0	754.8	9.8	1190.1	3548.6	1061.8	702.9	0.3	1.9	55.7	8.2	2.5	27.2	2178.8
20	10 - 30	28499.2	3.6	222.9	2435.9	52.5	5089.3	7966.4	5458.7	345.2	0.0	1.9	692.3	21.6	2.9	292.1	0.0
117	10 - 30	29681.1	11.6	598.0	1001.1	22.5	8815.5	18536.1	8996.8	522.9	0.0	0.7	289.9	7.4	1.4	118.5	0.0
176	10 - 30	32331.0	13.6	70.0	193.8	3.8	12589.2	16787.3	12869.6	393.4	0.0	0.0	3.5	1.8	0.0	2.4	0.0
227	10 - 30	1999.3	2.5	0.0	11256.5	231.1	6368.1	7963.9	6782.4	478.5	0.1	9.1	3398.3	86.1	14.8	1369.3	16.0
Seawater	10 - 30	2646.5	0.0	0.0	0.0	0.0	0.0	0.0	0.0	438.7	0.0	0.0	0.0	0.0	0.0	0.0	0.0
Snow	> 30	15220.2	5.8	402.7	987.5	18.9	93.8	0.0	229.5	297.3	0.0	0.7	192.7	6.4	0.9	102.9	0.0
10	> 30	16642.8	28.9	2473.7	319.1	2.8	1808.5	12269.3	477.3	401.7	0.1	0.0	43.6	7.4	0.0	2.1	0.0
20	> 30	34843.3	9.3	376.4	87.9	3.4	11350.3	17135.4	12409.5	396.7	0.0	0.0	2.2	3.5	0.0	1.1	0.0
117	> 30	34012.6	12.0	928.4	54.5	2.1	9839.7	17133.6	8009.7	750.6	0.0	0.0	1.6	2.5	0.0	0.7	0.0
176	> 30	48901.8	12.8	131.7	395.3	9.5	13235.4	16561.3	11871.8	434.8	0.0	0.2	68.1	1.4	0.8	35.1	0.0
227	> 30	27830.1	6.2	0.0	147.5	3.5	10490.4	13244.7	10462.9	405.4	0.0	0.0	73.5	0.4	1.0	15.4	0.0
Seawater	> 30	2730.2	0.0	0.0	0.0	0.0	0.0	0.0	0.0	231.4	0.0	0.0	0.0	0.0	0.0	0.0	0.0

Table B.9
Labile elemental data for core S3, CAA

Core depth (cm)	Grain size (μm)	Si (nM)	Ti (nM)	Al (nM)	Fe (nM)	Mn (nM)	Mg (nM)	Ca (nM)	K (nM)	P (nM)	Cd (nM)	Co (nM)	Cr (nM)	Cu (nM)	Mo (nM)	Ni (nM)	Zn (nM)
5	0.2 - 5	1099.2	63.6	2254.1	1637.5	62.9	92329.8	9245.3	7838.0	144.0	0.7	1.3	22.2	42.9	0.3	9.8	33.1
15	0.2 - 5	1082.5	9.7	0.0	22.9	0.0	7041.2	2337.3	2014.3	77.5	0.0	0.0	0.0	4.8	0.0	0.0	0.0
30	0.2 - 5	39568.8	2.1	0.0	0.0	0.0	7345.2	2439.2	2286.4	124.2	0.0	0.0	0.0	0.0	0.0	0.0	0.0
103	0.2 - 5	1795.3	6.5	0.0	0.0	0.0	10594.0	3379.1	3084.2	130.4	0.0	0.0	0.6	0.7	0.0	0.0	0.0
175	0.2 - 5	782.9	13.2	0.0	7.3	0.0	27000.9	9342.5	7817.3	507.9	0.0	0.0	1.8	16.3	0.0	0.0	0.0
5	5 - 10	1042.4	18.0	0.0	83.4	0.0	33863.3	11457.7	9301.1	206.1	0.0	0.0	3.7	17.7	0.1	0.0	0.0
15	5 - 10	735.6	3.1	0.0	23.9	0.0	6962.2	2337.6	1971.2	150.2	0.0	0.0	0.5	0.0	0.2	3.9	0.0
30	5 - 10	31408.4	3.9	0.0	0.0	0.0	11108.7	3656.4	3289.0	119.5	0.0	0.0	0.0	0.0	0.0	0.0	0.0
103	5 - 10	719.6	3.3	0.0	0.0	0.0	4744.5	1579.1	1440.8	108.4	0.0	0.0	0.0	0.4	0.0	0.0	0.0
175	5 - 10	843.8	3.1	0.0	0.0	0.0	9637.5	3141.3	2687.1	253.5	0.0	0.0	0.1	7.6	0.0	0.0	0.0
5	10 - 30	1252.4	73.8	426.5	600.3	6.2	103085.9	41254.3	31376.3	332.6	0.2	0.0	30.5	28.0	0.2	12.7	34.4
15	10 - 30	1785.2	55.4	485.5	936.0	5.1	84462.1	32839.6	24932.0	394.4	0.1	0.0	13.3	11.0	0.1	111.2	42.5
30	10 - 30	41071.9	43.3	2673.0	364.0	7.0	64090.4	25034.2	19278.1	207.8	0.1	0.0	20.5	15.0	0.1	9.1	23.4
103	10 - 30	1673.3	26.3	252.5	507.2	12.0	37577.9	16712.4	12640.3	354.5	0.4	0.0	23.1	14.6	0.1	14.4	7.9
175	10 - 30	8579.2	32.6	113.5	153.4	6.1	54919.3	19688.4	16300.3	283.4	0.1	0.0	7.3	24.0	0.1	3.3	0.0
5	> 30	1610.1	108.3	1423.9	315.7	4.1	150083.2	74366.1	53053.6	297.6	0.2	0.0	29.7	16.9	0.2	7.3	11.8
15	> 30	81120.5	32.3	940.5	337.3	11.3	43388.3	17299.3	12708.9	371.9	0.1	0.0	14.0	10.0	0.1	15.8	11.5
30	> 30	2313.2	66.8	4381.5	908.9	8.0	83620.6	39203.8	23818.4	386.5	0.1	0.0	30.5	12.8	0.2	126.0	83.5
103	> 30	1763.2	30.9	626.6	239.5	6.5	44057.4	18906.6	14236.3	190.6	0.1	0.0	19.0	10.0	0.1	7.2	0.0
175	> 30	2862.4	32.3	37.9	21.4	1.9	56824.7	22342.6	20218.3	570.2	0.1	0.0	0.7	11.3	0.0	0.6	0.0

Table B.10
Total elemental data for core S3, CAA

Core depth (cm)	Grain size (μm)	Si (nM)	Ti (nM)	Al (nM)	Fe (nM)	Mn (nM)	Mg (nM)	Ca (nM)	K (nM)	P (nM)	Cd (nM)	Co (nM)	Cr (nM)	Cu (nM)	Mo (nM)	Ni (nM)	Zn (nM)
5	0.2 - 5	1817.9	63.6	2254.1	1637.5	62.9	92335.1	9245.3	7838.0	243.2	0.7	1.3	22.2	42.9	0.3	9.8	33.1
15	0.2 - 5	1725.2	9.7	0.0	22.9	0.0	7063.0	2337.3	2014.3	163.1	0.0	0.0	0.0	4.8	0.0	0.0	0.0
30	0.2 - 5	40251.1	21.6	0.0	5011.7	99.9	7373.0	2439.2	2655.7	207.8	0.0	4.1	1517.4	41.0	10.8	639.0	0.0
103	0.2 - 5	2370.1	6.5	0.0	0.0	0.0	10598.9	3379.1	3185.8	306.2	0.0	0.0	0.6	0.7	0.0	0.0	0.0
175	0.2 - 5	1881.3	13.2	0.0	7.3	0.0	27000.9	9342.5	7936.0	632.4	0.0	0.0	1.8	16.3	0.0	0.0	0.0
5	5 - 10	2405.1	18.0	0.0	83.4	0.0	33863.3	11457.7	9301.1	357.0	0.0	0.0	3.7	17.7	0.1	0.0	0.0
15	5 - 10	1994.5	3.1	0.0	23.9	0.0	6989.8	2337.6	2053.4	257.1	0.0	0.0	0.5	0.0	0.2	3.9	0.0
30	5 - 10	32175.6	3.9	0.0	19119.8	387.9	11131.5	3656.4	3445.3	233.5	0.1	15.3	5798.8	133.8	24.8	2350.0	77.7
103	5 - 10	1441.3	3.3	0.0	0.0	0.0	4744.5	1579.1	1440.8	238.1	0.0	0.0	0.0	0.4	0.0	0.0	0.0
175	5 - 10	1557.2	3.1	0.0	0.0	0.0	9637.5	3141.3	2687.1	350.9	0.0	0.0	0.1	7.6	0.0	0.0	0.0
5	10 - 30	1911.7	73.8	426.5	600.3	6.2	103097.4	41254.3	31376.3	417.1	0.2	0.0	30.5	28.0	0.2	12.7	34.4
15	10 - 30	2521.5	55.4	485.5	936.0	5.1	84493.2	32839.6	24932.0	461.3	0.1	0.0	13.3	11.0	0.1	111.2	42.5
30	10 - 30	41800.5	43.3	2673.0	757.2	16.6	64138.8	25034.2	19278.1	321.7	0.1	0.3	165.4	15.0	0.9	61.8	23.4
103	10 - 30	2345.7	26.3	252.5	7920.0	420.7	37590.0	17524.0	14418.6	523.4	0.6	25.8	2038.1	63.7	96.5	2117.2	9020.2
175	10 - 30	9244.6	32.6	113.5	153.4	6.1	54922.4	19688.4	16300.3	418.4	0.1	0.0	7.3	24.0	0.1	3.3	0.0
5	> 30	2265.3	108.3	1423.9	315.7	4.1	150090.6	74366.1	53053.6	386.1	0.2	0.0	29.7	16.9	0.2	7.3	11.8
15	> 30	81828.0	32.9	940.5	337.3	11.3	43400.6	17299.3	12708.9	460.7	0.1	0.0	14.0	10.0	0.1	15.8	11.5
30	> 30	2983.9	66.8	4381.5	4274.6	78.5	83620.6	39203.8	23818.4	487.6	0.1	2.7	1070.9	40.6	4.9	547.1	83.5
103	> 30	2479.8	30.9	626.6	239.5	6.5	44064.4	18906.6	14236.3	315.0	0.1	0.0	19.0	10.0	0.1	7.2	0.0
175	> 30	3580.2	32.3	37.9	21.4	1.9	56824.7	22342.6	20218.3	682.8	0.1	0.0	0.7	11.3	0.0	0.6	0.0

Table B.11
Filterable (<0.2 μm) elemental data for cores S4 (top) and S3 (bottom), CAA

Core depth (cm)	Si (nM)	Al (nM)	Fe (nM)	Mn (nM)	Mg (nM)	Ca (nM)	Na (nM)	K (nM)	P (nM)	Cd (nM)	Cr (nM)	Cu (nM)	Mo (nM)	Zn (nM)
5	6.1	206.6	14.9	12.5	9546.5	1844.8	83195.2	1677.3	0.4	4.7	1.3	3.7	62.2	28.2
20	4.8	71.5	19.3	17.3	6646.9	1287.4	57034.9	1171.3	0.4	9.1	1.3	8.0	46.1	68.7
63.5	3.5	78.3	8.5	35.8	6203.9	1200.2	54834.8	1106.3	0.3	2.8	0.7	4.4	43.1	67.5
90	91.6	290.1	317.6	81.6	6065.4	1166.1	52103.5	1066.5	0.3	2.2	1.0	35.4	29.5	95.4
113	4.2	118.5	15.3	120.9	6107.9	1177.1	52466.6	1029.5	0.5	24.8	1.7	5.8	44.8	58.3
127	2.1	139.6	20.9	8.8	6349.3	1195.1	55038.3	1069.9	0.3	5.1	5.9	2.7	46.8	28.1
Seawater	14.3	441.3	31.3	16.4	43616.6	8301.2	390299.4	7647.1	1.8	18.0	12.4	26.9	303.1	108.2

Core depth (cm)	Si (nM)	Al (nM)	Fe (nM)	Mn (nM)	Mg (nM)	Ca (nM)	Na (nM)	K (nM)	P (nM)	Cd (nM)	Cr (nM)	Cu (nM)	Mo (nM)	Zn (nM)
Snow	2.4	173.5	33.9	16.6	2740.1	514.8	22901.9	464.9	0.3	13.9	0.8	6.8	19.0	73.3
5	5.8	52.2	10.8	11.7	7903.3	1563.9	68534.5	1426.5	0.3	0.7	0.6	1.2	41.8	19.1
34.5	3.5	42.5	3.5	7.5	6764.8	1289.9	58180.3	1109.3	0.3	0.5	0.7	1.1	41.6	12.6
59	2.8	66.8	114.4	6.2	7601.2	1497.6	64572.0	1307.2	0.3	0.9	0.7	1.6	47.4	25.7
106	2.0	329.0	20.3	9.9	7913.1	1482.1	67740.1	1349.2	0.4	6.7	1.9	6.6	48.6	99.2

Table B.12
Filterable (<0.2 μm) elemental data for cores S2 (top) and S1 (bottom), Point Barrow, AK

Core depth (cm)	Si (nM)	Al (nM)	Fe (nM)	Mn (nM)	Mg (nM)	Ca (nM)	Na (nM)	K (nM)	P (nM)	Cd (nM)	Cr (nM)	Cu (nM)	Mo (nM)	Zn (nM)
Snow	0.4	36.0	9.1	3.4	6.5	2.1	35.7	1.0	0.0	0.2	0.6	0.8	4.3	5.8
10	0.4	111.9	9.6	4.2	52.5	12.4	489.5	10.3	0.0	2.3	4.9	11.4	4.3	39.5
20	0.6	250.9	2.0	2.6	2957.0	568.3	25849.3	514.1	0.1	0.7	1.2	6.5	19.6	38.0
117	0.8	345.9	2.0	2.6	2221.3	430.7	19747.6	400.4	0.3	0.6	1.2	6.2	15.4	109.9
176	0.9	197.2	4.4	2.3	4671.1	895.7	41546.1	800.5	0.2	1.3	1.2	3.8	28.8	51.0
227	1.3	124.4	3.5	1.9	4829.5	904.6	43986.0	833.1	0.3	3.3	2.3	5.1	36.8	29.7
Seawater	13.9	426.0	46.4	30.9	51079.7	9886.3	441767.0	8722.2	3.3	4.6	12.4	22.6	327.9	75.3

Core depth (cm)	Si (nM)	Al (nM)	Fe (nM)	Mn (nM)	Mg (nM)	Ca (nM)	Na (nM)	K (nM)	P (nM)	Cd (nM)	Cr (nM)	Cu (nM)	Mo (nM)	Zn (nM)
5	1.3	951.3	9.4	5.9	10254.1	1966.7	93083.7	1750.8	0.4	3.5	4.0	7.4	74.4	58.5
15	1.1	422.0	4.9	3.3	7233.6	1403.8	61607.0	1252.9	0.2	1.0	1.4	3.0	54.5	22.4
30	1.1	493.9	1.8	3.1	7663.8	1471.7	67164.9	1321.3	0.2	1.1	1.6	3.4	50.6	22.8
103	1.1	216.5	2.8	3.7	5579.2	1074.5	49431.9	947.3	0.2	2.3	2.4	9.2	40.3	40.8
175	0.8	130.7	2.1	2.4	6248.8	1225.3	57113.9	1109.6	0.3	1.4	1.5	6.5	47.6	34.6